UNIVERSITY OF CALIFORNIA, SAN DIEGO

Spatial and Temporal Scales of Precipitating Tropical Cloud Systems

A dissertation submitted in partial satisfaction of the

requirements for the degree Doctor of Philosophy

in

Oceanography

By

Eric Martin Wilcox

Committee in charge:

V. Ramanathan, Chair
Daniel Cayan
Carl Gibson
Richard C. J. Somerville
Bradley T. Werner

2002

The dissertation of Eric Wilcox is approved, and it
is acceptable in quality and form for publication on
microfilm:

_____

_____

_____

_____

_____

Chair

University of California, San Diego

2002

for Erin

TABLE OF CONTENTS

B_λ	blackbody emission (W m^{-2} str^{-1} m^{-1})
C	speed of light (2.998×10^8 m s^{-1})
C_l	longwave cloud radiative forcing (W m^{-2})
C_s	shortwave cloud radiative forcing (W m^{-2})
$\dot{E}$	evaporation rate (kg kg^{-1} s^{-1})
$\dot{E}$	evaporation rate (kg m^{-2} s^{-1})
F	longwave flux at top-of-atmosphere (W m^{-2})
F_{clr}	clear-sky longwave flux at top-of-atmosphere (W m^{-2})
F_c	grid cell fraction containing cloud
F_p	grid cell fraction containing precipitation
F_{cp}	grid cell fraction containing cloud and precipitation
f_{240K}	fraction of cloud area with IR brightness temperature less than 240K
G	coefficient for infrared rain estimate (mm hr^{-1})
h	Planck constant (6.626×10^{-34} J s)
I	radiant intensity (W m^{-2} str^{-1} m^{-1})
k	Boltzmann constant (1.381×10^{-23} J K^{-1})
k_E	coefficient of rain evaporation
L	condensed water amount in grid cell (kg m^{-2})
L_c	condensed water amount from convection (kg m^{-2})
L_c	condensed water amount from stable condensation (kg m^{-2})
L_v	latent heat of vaporization (J kg^{-1})
LH	latent heating and latent heat flux (W m^{-2})
n	aerosol mixing ratio (kg kg^{-1})
$\dot{P}$	production rate of precipitating water in grid cell (kg m^{-2} s^{-1})
$\dot{Q}$	net production rate of precipitating water in grid cell ($\dot{P}$ - $\dot{E}$; kg m^{-2} s^{-1})
$\dot{Q}_c$	net production rate of precipitating water from convection (kg m^{-2} s^{-1})
$\dot{Q}_{sc}$	net production rate of precipitating water from stable condensation (kg m^{-2} s^{-1})
RH	relative humidity
R	rate of production of precipitation (kg kg^{-1} s^{-1})
R_s	surface rain rate (mm hr^{-1})
S	solar flux (W m^{-2}), also radiant source term (W m^{-2} str^{-1} m^{-1})
SH	sensible heat flux (W m^{-2})
T	temperature (K)
T_{IR}	METEOSAT-5 infrared window channel brightness temperature (K)
T_{WV}	METEOSAT-5 water vapor channel brightness temperature (K)
α	albedo, also extinction coefficient (m^{-1})
α_{clr}	clear-sky albedo

λ	wavelength
ρ_w	density of water (kg m^{-3})
CCM3	Community Climate Model version 3
CEPEX	Central Equatorial Pacific Experiment
CERES	Clouds and the Earth's Radiant Energy System
CRF	cloud radiative forcing
ERBE	Earth Radiation Budget Experiment
GATE	Global Atmospheric Research Program Tropical Experiment
GCM	general circulation model
INDOEX	Indian Ocean Experiment
IR	infrared
ITCZ	Inter-tropical Convergence Zone
MATCH	Model for Atmospheric Transport and Chemistry
MCS	mesoscale convective system
MPF	mesoscale precipitating feature
NCAR	National Center for Atmospheric Research
SSM/I	Special Sensor Microwave Imager
TOA	top-of-atmosphere
TRMM	Tropical Rainfall Measuring Mission
TMI	TRMM Microwave Imager
WV	water vapor

LIST OF FIGURES

LIST OF TABLES

ACKNOWLEDGEMENTS

I wish to thank Prof. Ramanathan for his patient guidance and for providing the opportunity to work with the extraordinary group of scientists at the Center for Clouds, Chemistry and Climate. The students, staff and scientists of C^4 have been a tremendous support and I have benefited from countless discussions with Bill Conant, Baijun Tian, Rémy Roca, Andy Vogelmann, Chul Eddy Chung, and Guang Zhang, among others. I am also grateful to Prof. A. C. Mota, Ray Fitzgerald, and Erin Wilcox for proofreading and comments on an early draft.

I also thank the rest of my committee, all of whom have contributed to improving this project. In particular I thank Brad Werner for introducing me to my first real research problem and getting me started in the Earth sciences.

With support from NASA and The Universities Space Research Association I had the good fortune to spend a summer at the NASA Goddard Space Flight Center. While there, I received the guidance of Jim Weinman, who gave me my first lesson in satellite remote sensing. I also thank Mitchell Moncrieff for supporting me during a month-long visit to NCAR. The aerosol scavenging work presented in chapter 5 was hatched during conversations with Mark Lawrence (MPI-Mainz). Assistance from George Huffman (NASA/GSFC), Bill Collins (NCAR), and Phil Rasch (NCAR) with data and simulation models is greatly appreciated.

I am tremendously grateful to my family for their unconditional support of my pursuits. My mother has been continuously enthusiastic about my studies beginning long before I started graduate school. From my father I learned to always pursue the work that is most gratifying. I am also grateful to the Fitzgerald Family from whom I received daily encouragement, not to mention innumerable free meals. My greatest appreciation goes to Erin. We met while I was in the midst of applying to graduate schools, and she unwittingly committed herself to six long years with a struggling and occasionally starving graduate

student. In spite of that, she has been terrifically supportive throughout.

The text of chapter three, in full, is a reprint of the material as it appears in the Journal of Climate. I was the primary researcher and author, and the co-author, V. Ramanathan, directed and supervised the research that forms the basis for this chapter. The text of chapter four, in full, is a reprint of material that has been accepted for publication to the Journal of Climate pending revision. I was the sole researcher and author of this publication.

VITA

November 20, 1972	Born Palo Alto, California
1995	B.S. Physics, University of California, San Diego
1993 - 1994	Research assistant, Department of Physics, University of California, San Diego
1994 - 1996	Programmer, Institute for Geophysics and Planetary Physics, Scripps Institution of Oceanography, University of California, San Diego
1996 - 2002	Graduate student researcher, Center for Atmospheric Sciences, Scripps Institution of Oceanography, University of California, San Diego
Spring, 2000	Teaching assistant, Climate and Climate Change, Scripps Institution of Oceanography, University of California, San Diego
2002	Ph.D. Oceanography, Scripps Institution of Oceanography, University of California, San Diego

PUBLICATIONS

Wilcox, E. M., "Spatial and Temporal Scales of Precipitating Monsoonal Cloud Systems in Satellite Imagery and the NCAR CCM3", Journal of Climate, accepted pending revision, 2002

Wilcox, E. M. and V. Ramanathan, "Scale Dependence of the Thermodynamic Forcing of Tropical Monsoon Clouds: Results from TRMM Observations", Journal of Climate, vol. 14, pp. 1511-1524, 2001

Hellman, F., M. Q. Tran, A. E. Gebala, E. M. Wilcox and R. C. Dynes, "Metal-Insulator Transition and Giant Negative Magnetoresistance in Amorphous Magnetic Rare Earth Silicon Alloys", Physical Review Letters, vol. 77, pp. 4652-4655, 1996

FIELDS OF STUDY

Studies in Atmospheric Physics and Climate:
    V. Ramanathan
    Richard Somerville

Studies in Physical and Dynamical Oceanography:
>   Myrl Hendershott
>   Pearn Niiler
>   Lynne Talley
>   William Young

Studies in Marine Chemistry:
>   Joris Gieskes
>   Ralph Keeling

Studies in Fluid Dynamics:
>   Clinton Winant

Studies in Radiative Transfer:
>   Piotr Flatau

Studies in Observational Oceanography and Data Analysis:
>   Russ Davis
>   Robert Guza
>   Walter Munk
>   Robert Pinkel
>   Dean Roemmich

Studies in Remote Sensing:
>   David Sandwell

Studies in Complex Systems Physics:
>   Bradley Werner

Studies in Biological Oceanography:
>   David Checkley
>   Lisa Levin

ABSTRACT OF THE DISSERTATION

Spatial and Temporal Scales of Precipitating Tropical Cloud Systems

By

Eric Martin Wilcox

Doctor of Philosophy in Oceanography

University of California, San Diego, 2002

Professor V. Ramanathan, Chair

Precipitation, radiative forcing, and aerosol scavenging in tropical cloud systems over the wintertime Indian Ocean are examined in satellite observations and global atmospheric simulations. Measurements of surface rain rate and top-of-atmosphere radiative fluxes from the TRMM satellite, as well as brightness temperature measurements from the METEOSAT-5 satellite, are used to identify the boundaries of cloud systems, track their evolution, and determine the spatial and temporal scales of cloud thermodynamic forcing. The resulting quantitative, statistical description of monsoonal cloud systems is compared with simulated cloud systems in the NCAR CCM3 model.

Monsoonal clouds span a spectrum of spatial scales from smaller than 25 km^2 to greater than 10^7 km^2. Atmospheric heating owing to precipitation and the cloud greenhouse effect, as well as surface cooling owing to cloud albedo, increases with the spatial scale of cloud systems. As a result, thermodynamic forcing of the monsoonal environment is dominated by the contribution from giant semi-permanent decks of overcast cloud that

persist for days to weeks. Embedded within such cloud decks are numerous rain cells reaching up to 1 million square-kilometers because deep convection organizes into clusters of narrow overturning cells attached to a broad stratiform region of precipitation. A relatively few such mesoscale convective systems are greater than 10^5 km^2, yet are responsible for up to 70% of monsoonal precipitation. In contrast, simulated cloud systems in the model gently precipitate throughout their duration and everywhere within their boundaries. The model lacks a process that acts to organize convection into mesoscale episodic structures.

Precipitation is the principal means by which particulate pollution is removed from the atmosphere. The effect of model biases in the distribution of precipitation is tested by integrating satellite precipitation measurements into the MATCH chemical transport model. Mesoscale convective systems in the equatorial Indian Ocean are a substantial barrier to the transport of aerosols from South Asia to the Southern Hemisphere. Using observations of the spatial coverage of precipitation in the model reduces the amount of South Asian aerosol transported to the remote Northern Hemisphere by more than a factor of 2 compared to a simulation using model derived precipitation.

Chapter 1

Introduction

This dissertation analyzes observations and simulations of precipitating tropical cloud systems associated with deep atmospheric convection over the tropical Indian Ocean during the winter monsoon season. Such cloud systems are representative of the most energetic disturbances in the tropical atmosphere. The intense vertical motions occurring in their convective cores form the upward branch of the overturning flow that characterizes the general circulation of the tropical atmosphere. Condensed water, in the form of cloud material and precipitation provides the link between the sunlight that is ultimately responsible for oceanic and atmospheric dynamics, and heating gradients in the lower atmosphere that cause observed weather patterns. Because of the pivotal role of cloud systems in present climate, their representation in global climate models is a central point of debate in the pursuit of accurate and precise predictions of climate change.

Projections of the increase in global-averaged surface temperature over the next 100 years due to increasing greenhouse gas emissions vary from +1.4 $^\circ$C to +5.8 $^\circ$C based on global climate model simulations (Houghton et al. 2001). Variations in projected warming result from, among other things, uncertainties in the amount of future greenhouse increases, as well as uncertainties in the thermodynamic impacts of aerosols. However, a 1989 study of 14 climate models indicated that the greatest source of model-to-model variation in sensitivity to climate change results from differences in the representations of cloud processes and the feedback between clouds and climate (Cess et al. 1989). With regard to the development of cloud-climate research since then, the 2001 assessment report of the Intergovernmental

Panel on Climate Change concluded: "Although there has been clear progress in the physical content of the models, clouds remain a dominant source of uncertainty…" (Houghton et al. 2001).

The release of condensational heating within clouds, together with cloud/radiation interactions, determine in large part the general circulation of the atmosphere. These processes are together referred to as the thermodynamic forcing of a cloud and are the principal means by which cloud systems impact the thermal structure of the atmosphere. Among the challenges facing the climate modeling community are appropriately representing the thermodynamic forcing of cloud systems and predicting any shifts in the distribution of cloud forcing resulting from changes such as increasing greenhouse gas loading.

Satellite date provide an enormous amount of useful data on the structure and dynamics of clouds. While satellite observations have been used in the development and validation of model simulations of cloud processes, these data are typically averaged in time and space over stationary grids. Such Eulerian averaging can mask the relationship between the structure of cloud systems and their effects on the environment. Recognizing this limitation, several studies (Williams and Houze 1987; Machado and Rossow 1993; Boer and Ramanathan 1997) have initiated the Lagrangian approach of tracking clouds as individual objects. The present work extends the Lagrangian approach to unravel the following issues:

- the scale dependence of precipitation and associated latent heating,

- the scale dependence of cloud radiative forcing, and

- the scale dependence of the removal of pollution in the atmosphere.

Observations of cloud scales and scale dependent forcing are compared directly to simulated clouds in a global climate model for the purpose of testing the representation of tropical cloud systems in the model. This is accomplished by applying the same Lagrangian analysis to model output.

The study presented in chapter 3 indicates that the thermodynamic forcing of cloud systems depends strongly upon the spatial scales of cloud systems. This study also explores the relationship between the spectrum of naturally occurring cloud scales and the artificial separation between small clouds and large clouds imposed on atmospheric simulations by model grids of various resolutions. Many important cloud processes occur at scales smaller than a model grid cell. However, in the tropics they conspire to generate overcast decks of cloud spanning 10s of millions of square kilometers. Such decks span numerous grid cells in even coarse grid atmospheric simulations and are therefore identifiable in model output. The dependence of cloud forcing upon the scale of cloud systems is not explicitly simulated and must emerge from the model representation of cloud processes. Observations of scale dependent properties may therefore be exploited as a means of testing simulations of clouds in climate models. Such a validation is carried out in chapter 4 resulting in the identification of several important biases in the representation of precipitating tropical cloud systems. A key finding of the study in chapter 4 is that both the spatial and temporal distribution of tropical precipitation differ substantially in the model simulation from the observed distribution. The potential impacts of such a bias are many; one being that the removal rate of aerosol particles from the atmosphere may be improperly simulated. This is the subject of chapter 5.

The principal tools of this dissertation are satellite measurements of cloud properties and precipitation. Observations from the Tropical Rainfall Measuring Mission (TRMM) satellite are used extensively. TRMM is noteworthy because it is the first satellite mission that provides simultaneous measurements of both precipitation and cloud radiative forcing, the two primary thermodynamic influences of cloud systems. Also used are cloud cover observations from the METEOSAT-5 geosynchronous satellite, which affords better temporal sampling than TRMM. Automated image processing tools have been developed as part of this dissertation project that identify the boundaries of cloud and precipitation structures,

evaluate their sizes, compute the magnitudes of thermodynamic forcing averaged over the area of each structure, and track cloud systems as they evolve through consecutive satellite images. The result is a novel analysis technique that is the basis of the studies presented in chapters 3 and 4. In these studies, ensembles comprising thousands of clouds are assembled from which a statistical description of the spectrum of cloud system scales is constructed and the scale dependence of cloud thermodynamic forcing is evaluated. The description of natural cloud systems that emerges from these analyses is then compared with simulations of tropical cloud systems in a modern atmospheric general circulation model (GCM), the National Center for Atmospheric Research Community Climate Model (NCAR CCM3), and a derivative of CCM3 used for aerosol and trace gas chemistry studies called the Model for Atmospheric Transport and Chemistry (MATCH).

The remainder of this chapter explains in more detail the context for the dissertation, beginning with the paramount role of clouds in the atmosphere-surface energy budget. This is followed by a description of the important structural elements of precipitating tropical cloud systems and a discussion of the representation of cloud systems in modern simulations of the global atmosphere.

1.1 Energy budgets of the atmosphere and surface

In the simplest terms, the dynamics of the ocean and atmosphere are motivated by the equator-to-pole gradient in solar heating. On average the Earth receives 235 W m^{-2} of solar (or shortwave) energy, with far more impinging on the tropics than poles. Assuming the planet is in approximate equilibrium, it must emit back to space a comparable amount of energy in the form of terrestrial infrared radiation (also called longwave or heat radiation). The latitudinal variation of infrared radiation, however is much smaller, resulting in an excess of heat in the tropics that must be transported poleward by oceanic and atmospheric dynamics.

Though the energy for atmospheric dynamics originates at the sun, the atmosphere
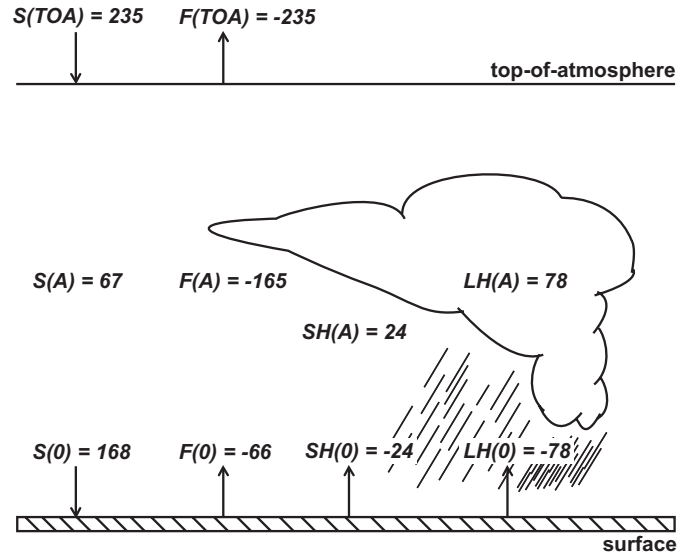
Fig 1.1. Top of the atmosphere (TOA), atmosphere (A), and surface (0) global annual averaged energy budget terms, including net shortwave flux (S), net longwave flux (F), sensible heat (SH) and latent heat (LH). Units are $W\ m^{-2}$ (values from Kiehl and Trenberth 1997).

is largely transparent to solar radiation, implying that additional processes are required to transfer solar radiation into atmospheric heating. Solar energy absorbed by the ocean is withdrawn from the surface by evaporation. An equivalent amount of energy (78 $W\ m^{-2}$ averaged over the globe) is then given to the atmosphere when this same water condenses into clouds and rain. This transfer process is called the latent heat flux. Global-, annual-average values of the surface and atmosphere energy budget terms are shown in Fig. 1.1 (values taken from Kiehl and Trenberth 1997). The atmosphere is principally warmed by latent heating (*LH(A)*) and cooled by infrared radiation (*F(A)*). Conversely, the ocean is principally heated by solar radiation (*S(0)*) and cooled by evaporation (*LH(0)*).

Global mean values, however, say nothing about the equator-pole gradients alluded to above. The northern hemisphere meridional gradients of the atmospheric heat budget components are shown in Fig. 1.2a (values from Hartmann 1994) and indicate that warming peaks in the tropics. Net heating occurs in the tropics because precipitation, hence latent heating, dominates infrared cooling there. The converse is true near the pole, where latent

Atmosphere Budget

Surface Budget

Top-of-Atmosphere CRF

latitude
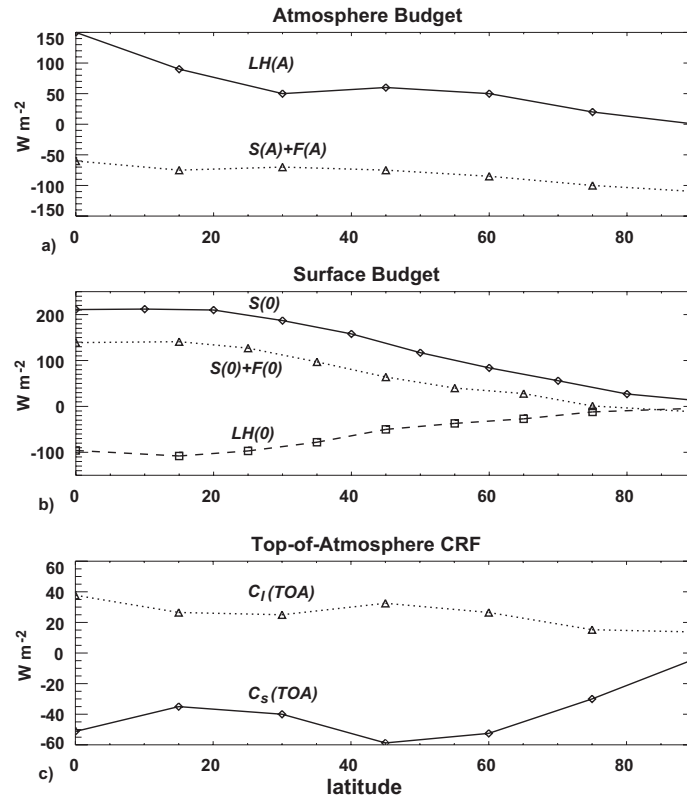
Fig 1.2. Northern hemisphere zonal-mean values of (a) atmospheric energy budget components (values from Hartmann 1994), (b) surface energy budget components (values from Sellers 1965), and (c) top-of-atmosphere cloud radiative forcing (CRF; values from Harrison et al. 1990). All values in W m-2.

heating from precipitation is insufficient to balance infrared cooling. The corresponding meridional gradients of the surface heat budget components are shown in Fig. 1.2b (values from Sellers 1965). Surface absorption of solar energy in the tropics exceeds 200 W m^{-2}, roughly twice the cooling owing to evaporation. Thus, the heating gradient at the surface arises largely from the peak in solar incidence at the tropics, while the heating gradient in the atmosphere arises largely from the peak in latent heating in the tropics.

Infrared and solar radiation interact with atmospheric trace gases such as water vapor, carbon dioxide, and methane. In addition, clouds have an important impact on the flux of radiation through the atmosphere. The weak meridional gradient in atmospheric radiative cooling shown in Fig. 1.2a includes the contributions from all of these interactions. Cloud

radiative forcing (CRF), a simple means of separating the effect of clouds on the radiative energy budget (Ramanathan 1987), is the difference between the clear sky radiative fluxes and the cloudy sky fluxes. Shortwave cloud forcing (C_s) is given by

$$C_s = S(\alpha_{clr} - \alpha), \tag{1.1}$$

where S is the solar constant, α_{clr} is the clear-sky albedo and α is the all-sky albedo. Longwave cloud forcing (C_l) is given by

$$C_l = F_{clr} - F, \tag{1.2}$$

where F_{clr} is the clear-sky longwave flux to space and F is the all-sky longwave flux. When the approach was applied to the ERBE satellite observations (Ramanathan et al. 1989), it revealed that clouds have a net radiative cooling effect of about -20 W m^{-2} (*i.e.*, the global average of the sum of C_l and C_s is -20 W m^{-2}). The meridional gradients of C_l and C_s at the top of the atmosphere are shown in Fig. 1.2c (data from Harrison et al. 1990). Local maxima in CRF occur in the tropics and the extra-tropical storm track. Ramanathan (1987) demonstrated that C_s in a GCM is expressed nearly entirely as a surface cooling, while C_l is expressed largely as a warming of the atmosphere. Thus the tropical peak in C_l suggests that longwave heating in tropical clouds enhances the equator to pole gradient in latent heating, while the peak in C_s suggests that the shortwave cooling effect reduces the solar heating gradient at the surface. Diagnostic and modeling studies (*e.g.*, Randall et al. 1989; Tian 2002) indicate that the gradient in C_l is instrumental in maintaining the observed thermal and moisture structure, as well as the circulation, of the tropical atmosphere.

The mean circulation over the Indian Ocean region during the winter monsoon is an example of the thermally-direct overturning circulation that results in the tropical atmosphere from heating gradients such as those discussed above (Fig. 1.3). Net heating in the convergence zone south of the equator gives rise to a narrow region of strong upward motion. The upward motion occurs through the process of atmospheric convection

8
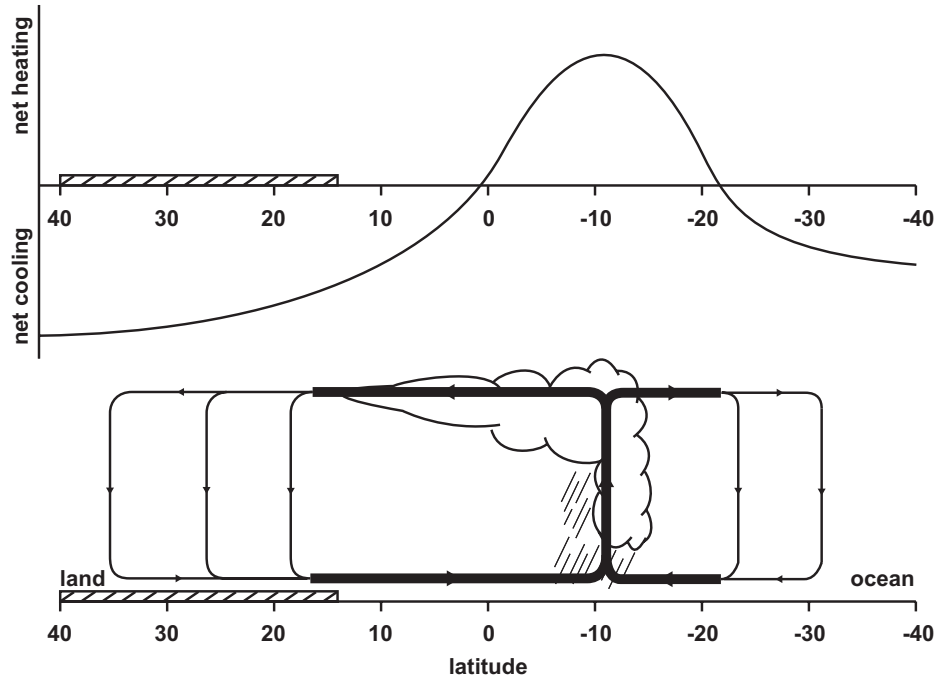
Fig 1.3. Schematic depiction of the net meridional heating structure, and the resulting circulation, over the Indian Ocean region during the winter monsoon (adapted from Webster 1987).

and is associated with precipitating cloud systems that contribute to the warming of the atmosphere through latent heating and longwave cloud radiative forcing. Net cooling away from the convergence zone is associated with broad, gentle subsidence. Such a circulation is characteristic of the time-mean dynamics of the tropical atmosphere in general. In the case of the monsoon, the strength of the heating gradient and the location of the convergence zone are further influenced by the properties of the south Asian landmass.

Evidence is now mounting that aerosol concentrations in the atmosphere are growing as a result of increasing pollution, and that the radiative impacts of the aerosols may be perturbing the energy balances described above (Ramanathan et al. 2001b). Solar radiation at the surface of the Indian Ocean was found to be reduced by -20 W m^{-2} during the 1999 winter monsoon as a result of pollution from South Asia (Ramanathan et al. 2001a). A high concentration of dark carbonaceous aerosols was also linked to an atmospheric heating of
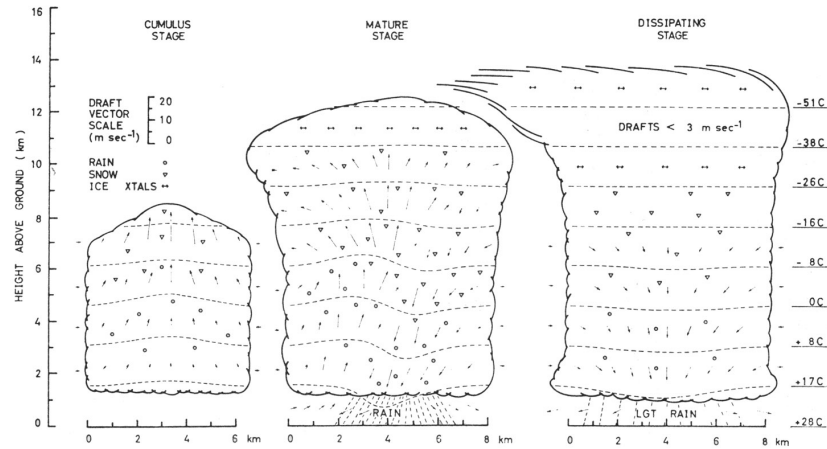
Fig 1.4. Three stages of development of a convective cell (from Chisholm 1973).

+18 W m^{-2}, owing to absorption of sunlight by the dark particles. The ability for regional sources of pollution to impact surface and atmospheric thermodynamics globally depends, in part, upon the efficiency of precipitating cloud systems to remove pollution and restrict long-range transport and mixing of aerosols.

1.2 The structure of precipitating tropical cloud systems

Although the general circulation of the tropical atmosphere is described above as being caused by the time- and space- averaged components of thermodynamic forcing, precipitation and cloud radiative forcing only occur in the presence of transient cloud systems. The quantities presented above are averages over contributions from numerous cloud systems. In regions of strong vertical motion, such as the wintertime tropical Indian Ocean, monthly-mean thermodynamic forcing is composed predominantly from contributions of a class of cloud system called a *mesoscale convective system* (MCS) (*e.g.*, Cotton and Anthes 1989; Houze and Betts 1981). As shown in chapter 3, roughly 20 such cloud systems are present over the Indian Ocean at a time in order to maintain the mean latent heating of the winter monsoon circulation. MCS structure is closely linked to the amount of latent heating and cloud radiative forcing produced by the system, as well as the scale of the system.
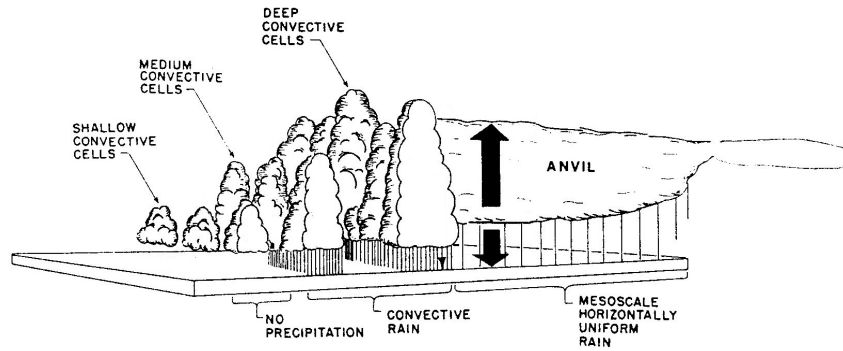
Fig 1.5. Schematic of a mesoscale convective system showing an ensemble of convective cells attached to stratiform anvil cloud and extended, non-precipitating cirrus cloud (from Houze et al. 1980).

A discussion of MCS structure is presented here.

The fundamental element of an MCS is the deep convective cell. Within a single cell, instability of warm moist air near the surface is released through the swift buoyant motion of air from the surface to the tropopause region (as high as 18 km in the tropics). Buoyancy is generated primarily through the rapid condensation of water into cloud drops (below the freezing level) and ice crystals (above the freezing level). Efficient coalescence of water and ice into rain, hail and graupel gives rise to strong rain rates at the surface. Evaporation of some of the precipitation as it falls within the cloud also gives rise to strong downdrafts adjacent to the convective updraft. Thus a single convective cell can be described as a narrow, vertically oriented overturning cell. A schematic of a convective cell is shown in Fig. 1.4. Aircraft studies indicate that convective cells have horizontal scales of 1 to 10 km (LeMone and Zipser 1980).

In MCSs, numerous convective cells group together within a single deck of cloud. As many as 10 may occur within a single MCS (Houze and Cheng 1977). At the tops of the convective cells large amounts of condensate detrain from the cells and spread horizontally. Therefore, adjacent to the region of deep convective cells, and within the same cloud deck, is a broad region of stratiform precipitation. The stratiform (sometimes called anvil) portion
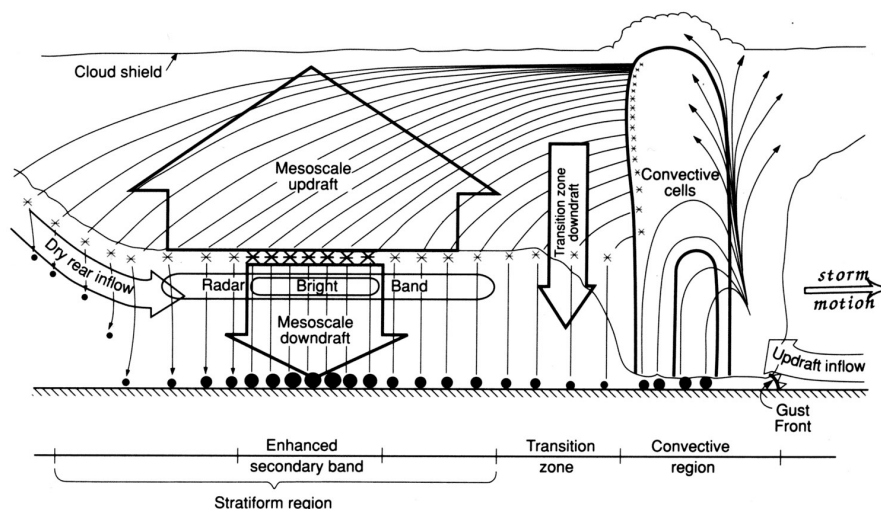
Fig 1.6. Schematic cross section through a mesoscale convective system indicating hydrometeor trajectories through a line of convective cells with a trailing stratiform anvil (from Biggerstaff and Houze 1991).

of the MCS is characterized by an upper-level region of precipitating cloud with horizontal scales of 100-1000 km and rain rates typically much lower than in the convective cells. Condensation within the stratiform portion gives rise to gentle, mesoscale uplift within the anvil cloud deck (Fig. 1.5). Generally, cloud-free air occurs below the stratiform portion, however some precipitation falling from above typically evaporates. Evaporative cooling results in a gentle, mesoscale downdraft below the anvil cloud deck. Though the mesoscale updraft implies some condensation in the anvil cloud, as much as 75% of the stratiform precipitation may result from hail and graupel detraining horizontally from the upper portions of the convective cells (Gamache and Houze 1983). Fig. 1.6 indicates typical trajectories of precipitating drops and hail.

In satellite images of the tropics, such as Fig. 1.7, structures larger than 1000 km are apparent. The colors in Fig. 1.7 correspond roughly with the temperature at the top of the clouds. Dark blue regions are cloud-free while red and yellow regions indicate where clouds associated with active convection are present. As shown in chapter 4, it is not uncommon for giant decks of cloud spanning 1000s of km to be maintained by numerous

18 Jan 1999 1100 GMT
METEOSAT5 IR brightness temperature (K)
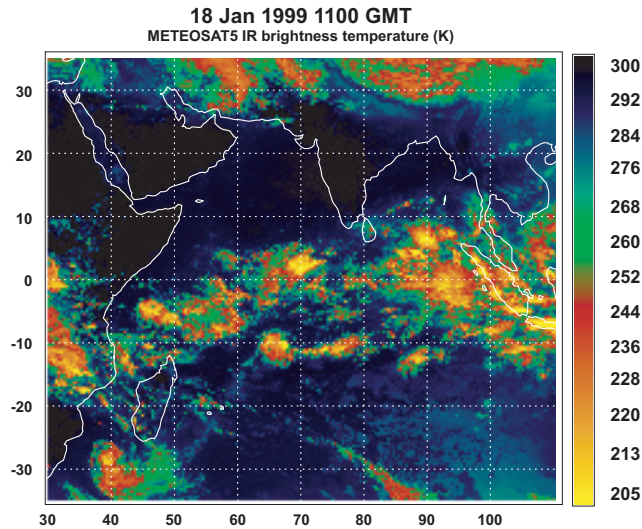
Fig 1.7. Infrared channel brightness temperature image (in K) from METEOSAT-5 from 18 Jan. 1999.

MCSs embedded within. Quantifying the spectrum of cloud systems that results from the hierarchy of convective structures described above is an important goal of this dissertation.

1.3 Cloud systems in atmospheric simulations

In order to perform simulations suitable for climate predictions, global climate models must account for the mass and momentum fluxes associated with the dynamics of tropical convection. Furthermore, the rate of condensation of rain drops must be predicted in order to calculate the magnitude of latent heating and the structure of the cloud decks must be predicted in order to calculate the cloud radiative forcing

Because of the fundamental role of latent heating and cloud radiative forcing in the planetary energy budget, global climate models must account for these processes, and anticipate changes in them resulting from greenhouse gas forcing, in order to perform simulations suitable for climate predictions. In the tropics, these processes are intimately related to atmospheric convection. Though the equations governing atmospheric dynamics in principle include the physics of convection, present day limitations in computing power prevent long-range, global climate predictions from being performed at sufficient resolution

to capture individual convective cells or even mesoscale anvil structures. All of the processes associated with a tropical cloud system residing within a grid cell are therefore computed using parameterizations that attempt to predict these quantities based on single, grid cell-averaged values of pressure, temperature, humidity and wind.

Much improvement remains to be made with respect to simulations of cloud systems in climate models. For example, an ensemble of convective cells occurring within a column of grid cells is typically predicted based on the column profile of instability (Arakawa and Schubert 1974). However cloud cover in a grid cell is often predicted based only on the grid cell value of relative humidity (Slingo 1987). The physical link between simulated convective dynamics and simulated cloud cover is weak in most models, in spite of the structure of tropical cloud systems being tightly coupled to convective dynamics. The assumption inherent in the present-day approach to cloud and convection parameterization is that all of the relevant processes occur at subgrid scales. As shown in chapter 3, however, the typical sizes of climate model grid cells are spanned by the spectrum of tropical cloud and precipitation structures, calling into question this assumption. Finally, the fluxes occurring in

References

Arakawa, A., and W. H. Schubert, 1974: Interaction of a cumulus cloud ensemble with the large-scale environment, part 1. *J. Atmos. Sci.*, **31**, 674-701.

Biggerstaff, M. I. and R. A. Houze, Jr., 1991: Kinematic and precipitation structure of the 10-11 June 1985 squall line. *Mon. Wea.. Rev.*, **119**, 3035-3065.

Boer, E. R. and V. Ramanathan, 1997: Lagrangian Approach for Deriving Cloud Characteristics from Satellite Observations and its Implications to Cloud Parameterization. *J. Geophys. Res.,* **102**, 21,383-21,399.

Cess, R. D. and co-authors, 1989: Interpretation of cloud-climate feedback as produced by 14 atmospheric general circulation models. *Science*, **245**, 513-516.

Chisholm, A. J., 1973: *Alberta Hailstorms. Part I: Radar Case Studies and Airflow Models.* Meteor. Monograph, **14**, No. 36. American Meteorological Society, Boston, 36 pp.

Cotton, W. R., and R. A. Anthes, 1989: *Storm and Cloud Dynamics*. Academic Press, San Diego,

CA, 883 pp.

Gamache, J. F. and R. A. Houze Jr., 1983: Water budget of a mesoscale convective system in the tropics. *J. Atmos. Sci.*, **40**, 1835-1850.

Harrison, E. F., P. Minnis, B. R. Barkstrom, V. Ramanathan, R. D. Cess, and G. G. Gibson, 1990: Seasonal variation of cloud radiative forcing derived from the Earth Radiation Budget Experiment. *J. of Geophys. Res.,* **95**, 18,687-18,703.

Hartmann, D. L., 1994: *Global Physical Climatology*, Academic Press, San Diego, CA, 411 pp.

Houghton, J. T., Y. Ding, D. J. Griggs, M. Noguer, P. J. van der Linden, and D. Xiaosu, Eds., 2001: *Climate Change 2001: The Scientific Basis: Contribution of Working Group 1 to the Third Assessment Report of the Intergovernmental Panel on Climate Change.* Cambridge University Press, 944 pp.

Houze, R. A., Jr., and C.-P. Cheng, 1977: Radar characteristics of tropical convection observed during GATE: Mean properties and trends over the summer season. *Mon. Wea. Rev.*, **105**, 964-980.

Houze, R. A., Jr., and C.-P. Cheng, C. A. Leary, and J. F. Gamache, 1980: Diagnosis of cloud mass and heat fluxes from radar and synoptic data. *J. Atmos. Sci.*, **37**, 754-773.

Houze, R. A., Jr., and A. K. Betts, 1981: Convection in GATE. *Rev. Geophys. Space Phys.,* **19**, 541-576.

Kiehl, J. T. and K. E. Trenberth, 1997: Earth's annual global mean energy budget. *Bull. Am. Meteorol. Soc.*, **78**, 197-208.

LeMone, M. A. and E. J. Zipser, 1980: Cumulonimbus vertical velocity events in GATE. Part I: Diameter, intensity and mass flux. *J. Atmos. Sci.*, **37**, 2444-2457.

Machado, L. A. T. and W. B. Rossow, 1993: Structural characteristics and radiative properties of tropical cloud clusters. *Mon. Wea. Rev.*, **121**, 3234-3260.

Ramanathan, V., 1987: The role of Earth radiation budget studies in climate and general circulation research. *J. of Geophys. Res.,* **92**, 4075-4095.

Ramanthan, V. R. D. Cess, E. F. Harrison, P. Minnis, B. R. Barkstrom, E. Ahmad, and D. Hartmann, 1989: Cloud-radiative forcing and climate: Results from the Earth Radiation Budget Experiment. *Science*, **243**, 57-63.

Ramanathan, V. and co-authors, 2001a: Indian Ocean Experiment: An integrated analysis of the climate forcing and effects of the great Indo-Asian haze. *J. Geophys. Res.*, **106**, 28,371-28-398.

Ramanthan, V., P. J. Crutzen, J. T. Kiehl, and D. Rosenfeld, 2001b: Aerosols, Climate and the Hydrological Cycle. *Science*, **294**, 2119-2124.

Randall, D. A., T. G. Corsetti, Harshvardhan, and D. A. Dazlich, 1989: Interactions among radiation, convection, and large-scale dynamics in a general circulation model. *J. Atmos. Sci.*, **46**, 1943-1970.

Sellers, W. D., 1965: *Physical Climatology,* University of Chicago Press, Chicago, IL, 272 pp.

Slingo, J. M. 1987: The development and verification of a cloud prediction scheme for the ECMWF model. *Quart. J. Roy. Meteor. Soc.,* **113**, 899-927.

Tian, B., 2002: *Cloud Radiative Forcing and the Tropical Hadley and Walker Circulations.* Ph.D. dissertation, Scripps Institution of Oceanography, University of California, San Diego.

Webster, 1987: The elementary monsoon, in *Monsoons* (J. Fein and P. Stephens, Eds.), John Wiley & Sons, New York, 632 pp.

Williams, M. and R. A.. Houze, Jr., 1987: Satellite-observed characteristics of winter monsoon cloud clusters. *Mon. Wea. Rev.*, **115**, 505-519.

Chapter 2

Passive Remote Sensing of Clouds and Precipitation

2.1 Introduction

In this dissertation, satellite measurements are used to observe the thermodynamic forcing of clouds, validate simulated cloud properties in a general circulation model (GCM), and evaluate aerosol scavenging rates. The satellite platform provides a useful vantage point for cloud studies. As will be shown in the following chapters, deep convective cloud systems span a wide spectrum of sizes, with overcast cloud decks and even precipitating structures exceeding millions of square kilometers. While ground-based and aircraft mounted observing systems provide more accurate measurements of some cloud parameters, they do not provide the necessary perspective to sample entire cloud systems on such spatial scales. Furthermore, the prohibitive cost of ship-based operations render satellites the most practical means of obtaining sufficient samples of clouds over ocean basins to perform statistical analyses of their properties.

Sampling clouds and precipitation from a satellite is by nature "remote", meaning cloud properties must be inferred from electromagnetic radiation that reaches the satellite from a cloud that may be hundreds or thousands of kilometers below. There are generally two classes of such remote sensing, active and passive. Active remote sensing involves broadcasting radiation from an antenna and measuring the quantity and quality of the backscatter signal. An example of active remote sensing is the ground-based weather radar, which has been the workhorse of operational meteorology for decades. However, research into active remote sensing of clouds and precipitation from satellites has only recently begun.

In contrast, passive remote sensing of clouds has been done from early in the satellite age. Passive sensing is performed by measuring the natural radiation that is emitted and/or scattered by water and ice hydrometeors.

This chapter will review the physical principles underlying the passive measurements that are used extensively in this dissertation. Some elements of radiative transfer theory pertinent to all of the measurements are presented in section 2.2. Section 2.3 addresses the use of the infrared channels of the METEOSAT-5 satellite to measure cloud cover. Section 2.4 discusses the use of microwave radiation for measuring surface rain rate. Broadband measurements of terrestrial infrared radiation and reflected solar radiation are discussed in section 2.5.

2.2 Elementary radiative transfer

The radiant energy emitted by a blackbody is determined by its temperature according to the Planck function:

$$B_\lambda = \frac{2hc^2}{\lambda^5} \frac{1}{e^{\frac{hc}{k\lambda T}} - 1} \tag{2.1}$$

in units of watts per unit area and unit solid angle. h is the Planck constant, k is the Boltzmann constant, c is the speed of light, λ is the wavelength and T is the temperature of the blackbody. The Earth emits approximately as a blackbody at with a temperature of about 300K. The radiation transmitted to space at the top of the atmosphere, however, is a complex spectrum determined by the profile of temperature and the emission and scattering properties of gases, particulates, cloud droplets and ice crystals within the atmosphere. This spectral response allows the retrieval of many atmospheric parameters, through measurements from space, of radiances at specific frequencies. Fig. 2.1 shows the Planck curve for a blackbody radiating at 300K. As shown, terrestrial radiation peaks in the infrared region of the spectrum. In this disseratation, measurements at two frequencies in the infrared will be used to detect the presence of clouds. As will be described in section 2.3, this approach
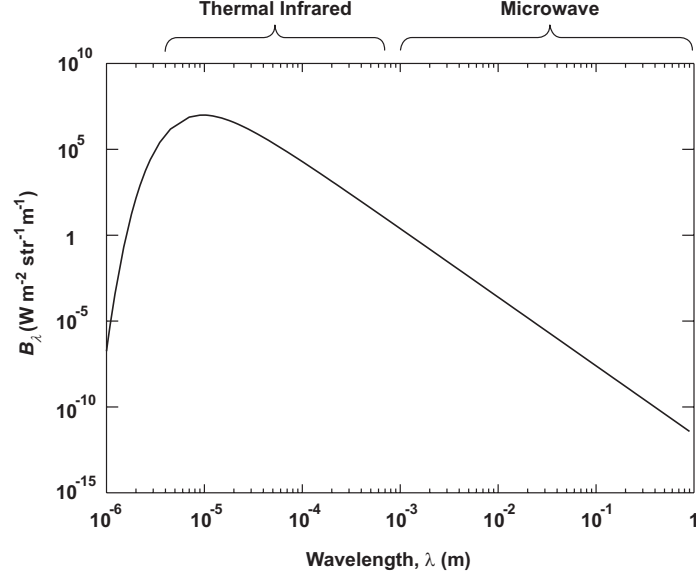
Fig 2.1. Energy emitted as a function of wavelength, given by the Planck Function, for a blackbody at 300 K.

will rely entirely on the absorption and emission by cloud drops and ice crystals, since these hydrometeors do not scatter infrared radiation. Fig. 2.1 also indicates that the long wavelength (low frequency) tail of the terrestrial emission extends into the microwave region of the spectrum. The transmission of microwaves through the atmosphere is strongly influenced by the presence of precipitation sized droplets and ice crystals. In this region of the spectrum, in addition to being subject to absorption and emission by precipitating hydrometeors, microwave radiation is also scatterd by precipitating ice. This is described in more detail in section 2.4.

The fundamental equation describing the flow of radiant energy is the starting point of any satellite remote sensing study. Following Janssen (1993), the radiant intensity per unit area, unit wavelength and unit solid angle (I) along path s is given by

$$\frac{dI}{ds} = -I\alpha + S \tag{2.2}$$

where α is the extinction coefficient and S is the source term. Thus the term with α represents the loss of intensity owing to absorption and scattering in the distance ds, and
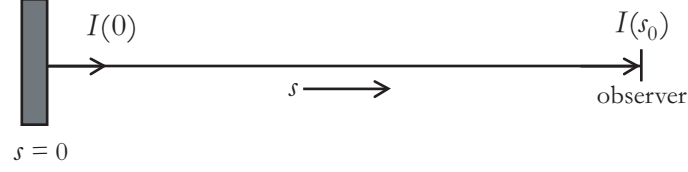
Fig 2.2. Geometry for remote sensing radiative transfer (from Janssen 1993).

the term with S represents the addition of intensity by either thermal emission or scattering of photons from other directions into the direction of ds (see diagram, Fig. 2.2). Radiant intensity is referred to interchangeably as intensity or radiance.

In the absence of scattering, losses are due only to absorption and the only source is thermal emission. In the atmosphere it is often the case that thermodynamic equilibrium prevails. This means that the energy absorbed in the section of path ds is equal to the energy emitted in ds. This is known as Kirchhoff's Law and requires that $S=\alpha B_\lambda$.

In the case without scattering, the solution to (2.1) for the intensity at location s_0 is:

$$I(s_0) = I(0)e^{-\alpha s_0} - \int_0^{s_0} B_\lambda(T(s)) e^{-\alpha(s_0-s)}\alpha ds \tag{2.3}$$

Thus the intensity at s_0 includes a contribution (first term, right side of Eqn. 2.3) from the emission at the boundary $s=0$, attenuated through the entire column (in the remote sensing case, $I(s=0)$ is the intensity of the surface emission). The second term includes a contribution from each segment ds along the column, attenuated through the remaining length of the column between s and s_0.

Equation 2.3 is sufficient to describe the cases of infrared transmission, as well as microwave transmission for wavelengths longer than about 2 cm, where contributions to α arise from absorption by cloud hydrometeors and precipitating hydrometeors respectively. However, Eqn. 2.3 is insufficient for the transmission of microwaves at wavelengths shorter than 2 cm because of contributions to α from scattering. This equation provides the intensity for a given distribution of T and α along the path s. Typically for remote sensing

applications, the problem is the inverse. Wavelengths are chosen for which the atmospheric constituent to be measured determines α. The measured value of intensity must be interpreted as an amount of the desired constituent. In many cases, there are contributions to α from several constituents so that measurements at several discrete wavelengths are required to constrain the problem.

In remote sensing studies, intensity is commonly converted to an equivalent brightness temperature, which is the temperature a blackbody would require in order to emit an intensity equal to the measured value. Thus, from Eqn. 2.1, brightness temperature can be expressed as:

$$T_B = \frac{hc}{k\lambda} \frac{1}{ln\left(\frac{2hc^2}{I\lambda^5} + 1\right)} \tag{2.4}$$

In the discussion that follows, intensity, which is the quantity directly measured by satellite imagers, will be converted to an equivalent brightness temperature.

2.3 Infrared cloud detection

In chapter 4 of this dissertation, measurements from the METEOSAT-5 spacecraft of infrared radiation in two narrow bands are used to identify regions of overcast cloudiness. METEOSAT-5 is a geosynchronous satellite located above the equator at 63° E longitude. The spacecraft orbits at a rate of exactly once per day, so that it remains stationary relative to the nadir point on the surface of the earth below it. A diagram of the orbit characteristics appears in Fig. 2.3. The imager mounted on the spacecraft produces an image of the entire Indian Ocean basin in three narrow frequency channels every half-hour (see Fig. 1.7, p. 12 for an example of an infrared channel image). In order to generate the image, the spacecraft is oriented with its axis parallel to the longitude line below it and rotates about the axis at a rate of 2500 rotations per image (image acquisition takes 25 minutes). As the spacecraft rotates, the imager instrument scans from high southern latitudes toward high northern latitudes, completing a scan of all latitudes in about 25 minutes.
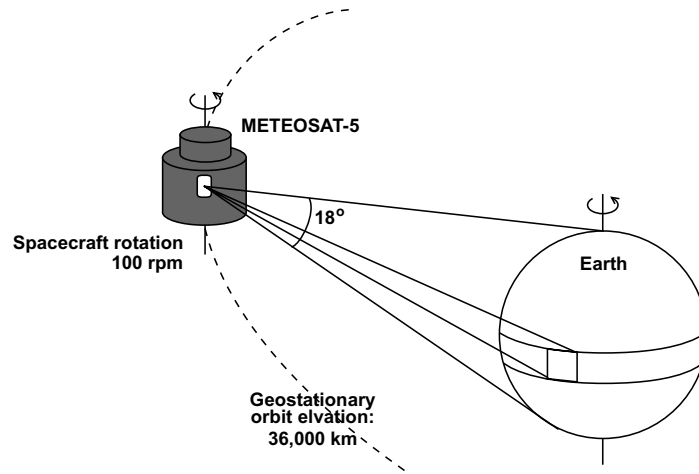
Fig 2.3. METEOSAT-5 orbit and image scanning characteristics (adapted from EUMETSAT 1999).

The cloud detection approach relies primarily on radiation at 11.5 μm (referred to below as the IR channel). This channel is sometimes referred to as the window channel because in the 8 - 12 μm region (also referred to as the window region) terrestrial radiation passes through the cloud-free atmosphere with almost no absorption (or top-of-atmosphere transmittance near 100% as shown in Fig. 2.4). Although the clear-sky atmosphere is nearly transparent within the window, clouds absorb strongly at these wavelengths. Even a moderately thick cloud will absorb virtually all of the upwelling terrestrial radiation passing up from below. Much of the radiance reaching the IR channel from such a cloudy column will then be the emission from the upper layer of the cloud deck. As a result, when the radiances are converted to brightness temperatures they provide an estimate of the cloud-top temperature.

Under clear-sky conditions, the IR channel measures a brightness temperature (T_{IR}) corresponding to the surface temperature (295 - 300 K for a tropical oceanic region). A brightness temperature colder than 280 K, for a 5 km METEOSAT-5 pixel, indicates that the pixel is overcast. Warmer pixels may be either clear-sky or partially filled with low, broken clouds.
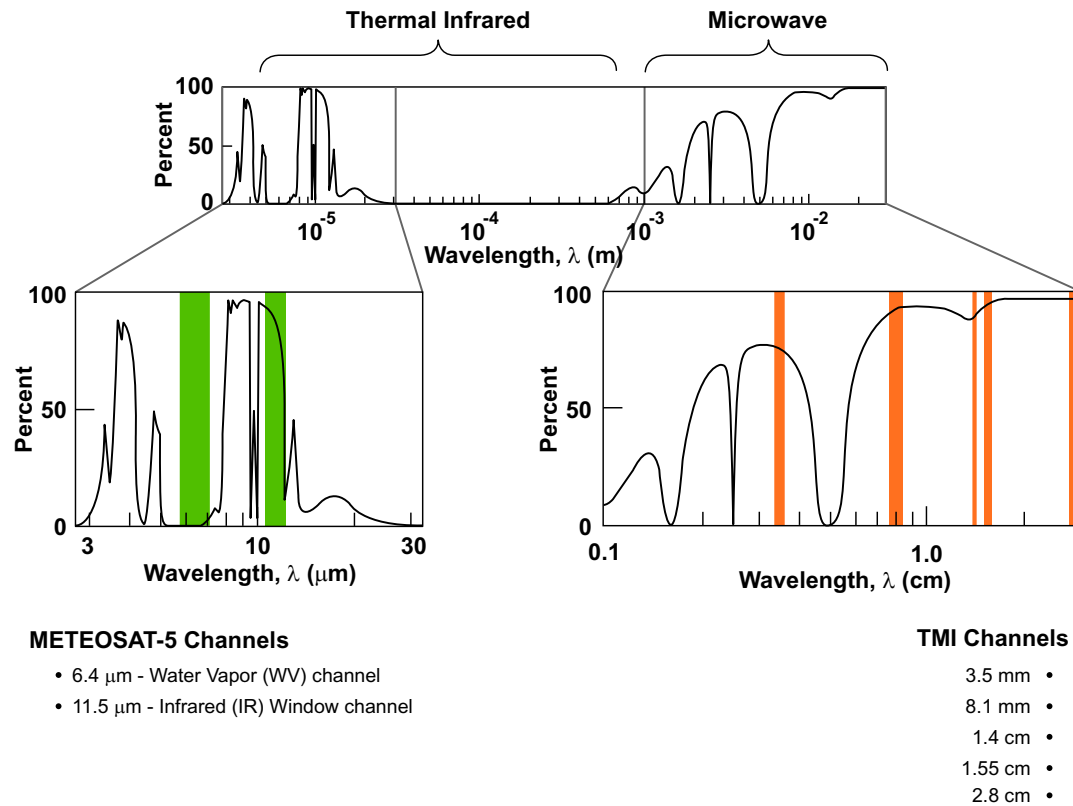
Fig 2.4. Clear-sky transmission at the top of the atmosphere for radiant energy emitted from the surface. Expanded are the spectral regions targeted by the METEOSAT-5 and TRMM Microwave Imager (TMI). Overlayed in color are the bandwidths of the imager channels. Green are METEOSAT-5 infrared channels and orange are TMI channels (adapted from Grody 1993).

There are some limitations to the use of the IR channel for cloud detection. Low clouds, such as marine stratocumulus decks, can be optically thick at the wavelength of the IR channel. However, because they are low clouds, their temperature is not very different from that of the surface. Such clouds can be difficult to distinguish from clear-sky scenes, particularly if the stratocumulus deck is broken with clear regions and cloudy regions mixed at sub-pixel spatial scales. Thin cirrus clouds can be difficult to distinguish from clear-sky scenes as well. Such clouds are often not thick enough to absorb an appreciable level of radiation in the window band.

For the case of low clouds, measurements during daylight hours of reflected solar
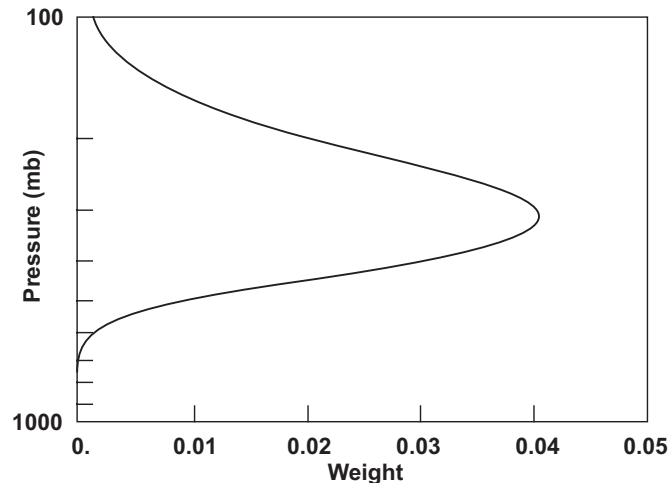
Fig 2.5. Normalized sensitivity of upwelling 6.7 μm intensity to clear-sky water vapor as a function of pressure level (from Soden and Bretherton 1993).

intensity can significantly improve their detection, as such clouds are often highly reflective.

For the purposes of this dissertation, detection of low clouds is not a priority, while tracking

cloud through nighttime hours is a priority, so visible channel radiances are not used.

Thin cirrus clouds, however, are a priority in the study presented in chapter 4. A second

infrared channel, centered at 6.4 μm is used for discriminating these clouds. As Fig. 2.4

indicates, virtually no surface emission within the 6.4 μm channel reaches space without

being absorbed, because this channel resides on a strong water vapor absorption feature.

This channel will be referred to as the water vapor (or WV) channel. Figure 2.5 shows the

relative sensitivity of the WV channel brightness temperature (T_{WV}) to changes in the water

vapor amount at different altitudes, according to the radiative transfer model of Soden and

Bretherton (1993). The sum of the weights over all pressure levels equals 1. T_{WV}, under

cloud-free conditions, is determined by the temperature and relative humidity in a broad layer

between 500 and 100 mb, corresponding to non-zero values of the sensitivity curve in Fig.

2.5. The WV channel brightness temperature decreases as relative humidity increases in the

layer. Saturated conditions in the layer correspond to a brightness temperature of about 240

K for the tropical atmosphere (Roca 2000). The 500 - 100 mb layer also corresponds to the

level of middle- and upper- tropospheric clouds, which also absorb upwelling WV channel radiation. WV brightness temperatures colder than 240 K typically indicate the presence of clouds in the layer. In many instances, pixels with T_{WV} less than 240 K will also have T_{IR} less than 240 K because cloud emission is similar in the IR and WV channels. For the thin cirrus case, however, T_{IR} may be warm, indicating clear-sky conditions, because IR channel emission from the warm surface may penetrate the cloud and contribute to the T_{IR} signal in addition to the cloud emission. In this case, only the WV channel will reveal the presence of cloud because T_{WV} is insensitive to the surface emission. The thresholds (T_{IR} < 280 K; T_{WV} < 240 K) are used in chapter 4 to detect clouds. They have been validated against other multi-spectral cloud retrievals and found to be suitable for discriminating clear-sky pixels from cloudy pixels, as well as classifying mid-level and upper-level cloud types (Roca et al. 2002). Furthermore, they served as the basis for operational cloud analyses during the Indian Ocean Experiment, which successfully aided in the planning of aircraft observations during the experiment (Roca et al. 2002).

2.4 Passive microwave rain measurements

The first scanning microwave imager was flown on an experimental satellite in 1978. Since 1987, similar instruments have been present on operational meteorological satellites. Beginning with the launch of the first microwave imager, there has been a steady effort to attain reliable measurements of surface precipitation by exploiting the microwave emission and scattering properties of precipitating water and ice. In 1997, the Tropical Rainfall Measuring Mission (TRMM) satellite was launched with the specific goal of measuring the amount of tropical rainfall.

The TRMM spacecraft orbits at a much lower altitude than METEOSAT-5 and at a much faster rate (once every 90 minutes). As a result, TRMM samples the surface in diagonal swaths, approximately 760 km across (see diagram in Fig. 2.6). The standard polar orbit for meteorological satellites passes directly over the poles. The orbit rate is coordinated with the
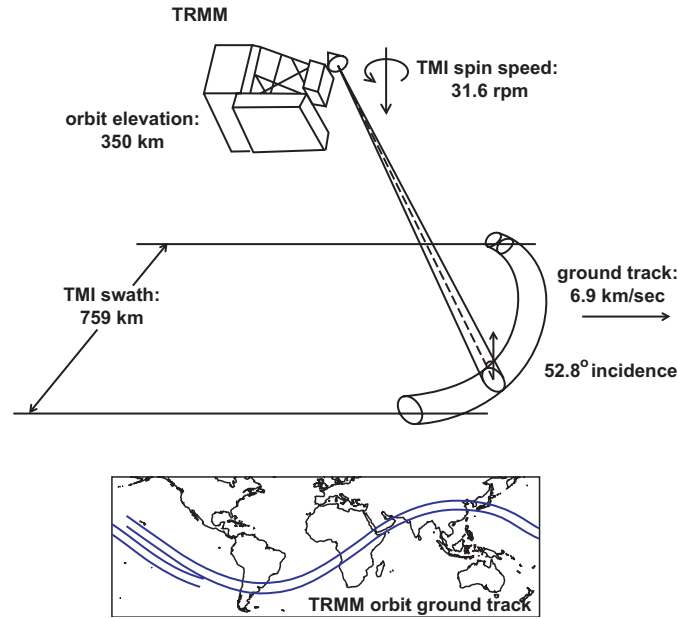
Fig 2.6. TRMM orbit and TMI scanning characteristics (adapted from Kummerow et al. 1998).

rotation of the Earth such that polar orbiting satellites cross the equator at exactly the same local time on each pass. In contrast to standard polar orbiters, the TRMM orbit is inclined at 35º latitude and is located at a lower altitude. As a result, the TRMM orbit precesses so that the local time of the equator crossing changes slightly with each orbit. This is designed to eliminate aliasing of diurnal variability in precipitation. The satellite samples all 24 local hours over the entire tropics every 45 days.

The instrument used in this dissertation is the TRMM Microwave Imager (TMI) which detects upwelling microwave radiances at 5 narrow channels within this spectral region. Additionally, 4 of these channels separately detect horizontally and vertically polarized radiation. The location of the 5 TMI wavelengths are indicated on the spectral top-of-atmosphere transmittance curve in Fig. 2.4. Within the spectral range of the TMI channels, transmittance depends on the vertically integrated tropospheric water vapor amount. Furthermore there are two distinct water vapor absorption features at approximately 5 mm and 1.35 cm. The 1.4 cm TMI channel is located on one of these features, specifically to
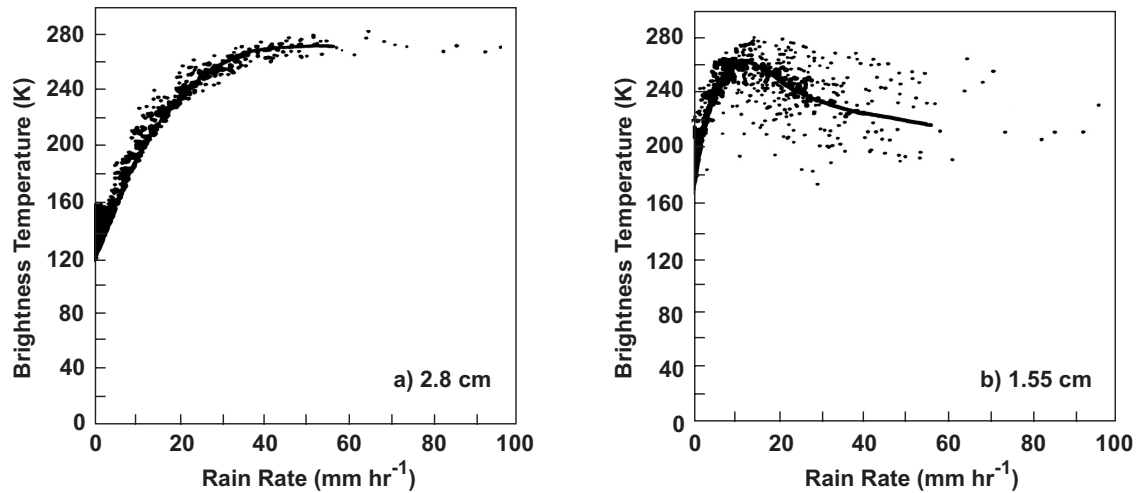
Fig 2.7. Simulated brightness temperatures as a function of rain rate for the (a) 2.8 cm and (b) 1.55 cm channels of the TMI (from Adler et al. 1991).

estimate the integrated water vapor amount and separate the water vapor effect from the precipitation effect on the brightness temperatures at the remaining channels.

Microwave precipitation detection works best over the ocean surface because emission from the ocean surface is low relative to emission from a precipitating cloud. Furthermore, the background ocean signal is spatially uniform. When viewing the ocean surface through a non-precipitating column the brightness temperature is low because the surface emissivity is low. When a precipitating cloud is present, precipitation sized water drops enhance the microwave emission of the atmosphere. As the amount of precipitating condensate increases, the microwave emission increases, and therefore the brightness temperature increases. Higher rain rates are generally correlated with thicker clouds and a greater amount of precipitating condensate, which leads to a relationship between microwave brightness temperature and surface rain rate. Fig. 2.7a shows the dependence of 2.8 cm brightness temperature on rain rate for a precipitating cloud over an ocean surface in the plane-parallel radiative transfer model of Adler et al. (1991). At the longest wavelength channels, radiation is insensitive to the presence of ice crystals in

tall clouds, therefore 2.8 cm brightness temperature increases with increasing rain rate until the signal saturates above about 40 mm hr^{-1}. At shorter wavelengths, however, significant scattering by precipitation sized ice (hail and graupel) is observed. This has the effect of reducing the measured brightness temperature, because a fraction of the upward emission from liquid raindrops will be scattered back downward by the ice above. Fig. 2.7b shows the 1.55 cm brightness temperature as a function of rain rate (Adler et al. 1991). In this simulated cloud, the rain rate is 10 mm hr^{-1} when the cloud rises to the freezing level, at which point precipitating ice begins to form. As shown in this figure, brightness temperatures at the top of the atmosphere begin to decrease as the rain rate increases above 10 mm hr^{-1}. Because the relative dependence upon emission and scattering is different for each TMI channel, each is primarily sensitive to precipitation in a different vertical level of the cloud.

For each precipitating cloud viewed by the TMI, a set of brightness temperatures is observed at 5 wavelengths. These brightness temperatures must then be inverted to a surface rain rate. This involves two steps: 1) retrieving a profile of precipitating hydrometeors from the measured brightness temperatures, and 2) relating the hydrometeor profile to a surface rain rate (usually by applying an assumed fall speed to the hydrometeor profile). The inversion problem, however, is often under-detemined, meaning that the same set of brightness temperatures may correspond to several different profiles of precipitating water and ice. To help constrain the problem, it helps to know what hydrometeor profiles are likely to occur in natural clouds. For this reason, many modern approaches to the inversion problem make use of high resolution, limited area numerical models of cloud dynamics. From such models it is possible to generate candidate profiles of precipitating hydrometeors, and corresponding simulated brightness temperatures, in order to compare with observed brightness temperatures. In the data product used in this dissertation, a Baysian approach is used to compute a linear combination of candidate profiles generated a priori from a

cloud model (Kummerow et al. 1996). Details of the inversion technique are included in section 3.2.1.

In addition to microwave rain detection, it has been demonstrated that rain rate estimates, averaged over large cloud systems, may be made using infrared brightness temperatures, such as those measured by METEOSAT-5 (Arkin and Meisner 1987). This approach relies on the correlation between the area covered by tall clouds in a region (which IR channels can measure) and the amount of rain falling in the region (which IR channels do not directly detect). IR estimates of rain rate have limited application because they rely on large spatial and/or long temporal averaging. However, for certain climate applications, they can be quite useful. This approach is used in a limited fashion in chapter 4 and a detailed discussion is presented in section 4.2.3.

2.5 Top-of-atmosphere radiative flux measurements

Top-of-atmosphere radiative flux measurements are used in chapter 3 to document the dependence of cloud radiative forcing (CRF) upon cloud and rain cell scale. These measurements are made with the Clouds and the Earth's Radiant Energy System (CERES) instrument (Wielicki et al. 1996) aboard the TRMM satellite. CERES measures upwelling radiation with three broadband radiometers. One channel measures total broadband radiance across the entire spectrum of infrared and visible wavelengths (0.2 - 100 μm). A second measures across the visible spectrum (0.2 - 5 μm), and a third one measures across the 8-12 μm infrared window. As discussed in chapter 1, CRF is calculated separately for terrestrial infrared (longwave) radiation and upwelling reflected solar (shortwave) radiation. The shortwave signal is measured directly with the CERES visible channel and the longwave signal is computed as the difference of the total channel and the visible channel.

The CERES radiometers measure radiances with an error of 1% or less. The surface footprint of each pixel is roughly 10 km and CERES scans across a swath of about 1000 km. Although the broadband fluxes reported for each pixel account for radiation

from all upwelling directions, the measurement from which the flux is derived is only a narrow radiance from a single direction. Therefore angular distribution models based on surface type and cloud cover are developed to estimate the anisotropy of the radiance. The difference between actual hemispheric fluxes and the retrieved fluxes assuming isotropy can be as large as a factor of 2. Thus the angular distribution models are the largest source of uncertainty in the retrieved fluxes. Reported errors in instantaneous top of the atmosphere fluxes for the pixel-scale data are typically 12% in the shortwave and 5% in the longwave (Suttles et al. 1992; Wielicki et al. 1995).

CRF is typically computed for time and space averages, such as monthly means over regions of hundreds of km. For this calculation, all of the CERES pixels in the region during the month are segmented into clear and cloudy. The clear pixels are then averaged to determine the mean clear-sky fluxes and all of the pixels are averaged to find the all-sky fluxes (Ramanathan et al. 1989). The difference between the clear and all-sky fluxes is the time-mean CRF (Eqns. 1.1 and 1.2). In contrast, chapter 3 will introduce measurements of instantaneous CRF for overcast pixels. This is the difference between the flux that would be observed if the cloud were not present and the flux that is actually observed. Because the clear-sky flux cannot be measured in this case, it is replaced with the monthly mean clear-sky flux. The instantaneous overcast flux is then subtracted. Variability of clear-sky fluxes over the ocean during the month adds an additional uncertainty of about 5 W m^{-2} to the measurements. For typical cloudy conditions, uncertainty in instantaneous longwave and shortwave CRF measured by CERES are about ±15 W m^{-2}.

References

Adler, R. F., H-Y. M. Yeh, N. Prasad, W-K. Tao, and J. Simpson, 1991: Microwave Simulations of a Tropical Rainfall System with a Three-dimensional Cloud Model. *J. Appl. Meteorol.*, **30**, 924-953.

Arkin, P. A., and B. N. Meisner, 1987: The relationship between large-scale convective rainfall and cold cloud over the Western Hemisphere during 1982-84. *Mon. Wea. Rev.*, **115**,

51-74.

EUMETSAT, 1999: *The METEOSAT System*. 66 pp.

Grody, N. C., 1993: Remote Sensing of the Atmosphere from Satellites Using Microwave
Radiometry, in *Atmospheric Remote Sensing by Mirowave Radiometry* (M. A. Janssen, Ed.)
John Wiley & Sons, New York, 572 pp.

Janssen, M. A., 1993: An Intoduction to the Passive Microwave Remote Sensing of
Atmospheres, in *Atmospheric Remote Sensing by Mirowave Radiometry*, (M. A. Janssen, Ed.)
John Wiley & Sons, New York, 572 pp.

Kummerow, C., W. S. Olson, and L. Giglio, 1996: A Simplified Scheme for Obtaining
Precipitation and Vertical Hydrometeor Profiles from Passive Microwave Sensors.
IEEE Trans. Geosci. Remote Sensing, **34**, 1213-1232.

Kummerow, C., W. Barnes, T. Kozu, J. Shiue, and J. Simpson, 1998: The Tropical Rainfall
Measuring Mission (TRMM) Sensor Package. *J. Atmos. Ocean Technol.,* **15**, 809-817.

Ramanathan, V., R. D. Cess, E. F. Harrison, P. Minnis, B. R. Barkstrom, E. Ahmad, and
D. Hartmann, 1989: Cloud-radiative forcing and climate: Results from the Earth
Radiation Budget Experiment. *Science*, **243**, 57-63.

Roca, R., 2000: *Contribution à l'étude de la vapeur d'eau, de la convection et de leurs interactions dans
les tropiques à l'aide d'observations de satellite et de modles*. Ph.D. dissertation, University of
Paris 7 Denis Diderot, pp. 208.

Roca, R., M. Viollier, L. Picon, and M. Desbois, 2002: A multi satellite analysis of deep
convection and its moist environment over the Indian Ocean during the winter
monsoon. *J. Geophys. Res.* special INDOEX issue, part 2, in press.

Soden, B. J., and F. P. Bretherton, 1993: Upper Tropospheric Relative Humidity from the
GOES 6.7 mm Channel: Method and Climatology for July 1987. *J. Geophys. Res.*,
98, 16,669-16,668.

Suttles, J. T., B. A. Wielicki, and S. Vemury, 1992: Top-of-Atmosphere Radiative Fluxes:
Validation of ERBE Scanner Inversion Algorithm Using *Nimbus-7* ERB Data. *Bull.
Amer. Meteor. Soc.,* **31**, 784-796.

Wielicki, B. A., R. D. Cess, M. D. King, D. A. Randall, and E. F. Harrison, 1995: Mission
to Planet Earth: Role of Clouds and Radiation in Climate. *Bull. Amer. Meteor. Soc.,*
76, 2125-2153.

Wielicki, B. A., B. R. Barkstrom, E. F. Harrison, R. B. Lee, G. L. Smith, and J. E. Cooper,
1996: Clouds and the Earth's Radiant Energy System (CERES): An Earth Observing
System Experiment. *Bull. Amer. Meteor. Soc.,* **77**, 853-868.

Chapter 3

Scale Dependence of the Thermodynamic Forcing of Tropical Monsoon Clouds: Results from TRMM Observations

Abstract

Clouds exert a thermodynamic forcing on the ocean-atmosphere column through latent heating, owing to the production of rain, and cloud radiative forcing, owing to the absorption of terrestrial infrared energy and the reflection of solar energy. The Tropical Rainfall Measuring Mission (TRMM) satellite provides, for the first time, simultaneous measurements of each of these processes on the spatial scales of individual clouds. Data from TRMM are used to examine the scale dependence of the cloud thermodynamic forcing and to understand the dominant spatial scales of forcing in monsoonal cloud systems. The tropical Indian Ocean is chosen, because the major monsoonal cloud systems are located over this region. Using threshold criteria, the satellite data are segmented into rain cells (consisting of only precipitating pixels) and clouds (consisting of precipitating as well as nonprecipitating pixels), ranging in scales from 10^3 km^2 to 10^6 km^2. For each rain cell and cloud, latent heating is estimated from the microwave imager and radiative forcing is estimated from the Clouds and the Earth's Radiant Energy System radiation budget instrument.

The sizes of clouds and rain cells over the tropical Indian Ocean are distributed lognormally. Thermodynamic forcing of clouds increases with rain cell and cloud area. For example, latent heating increases from about 100 W m^{-2} for a rain cell of 10^3 km^2 to as high as 1500 W m^{-2} for a rain cell of 10^6 km^2. Correspondingly, the liquid water path increases tenfold from 0.3 kg m^{-2} to nearly 3 kg m^{-2}, the longwave cloud forcing from 30 to 100 W

m^{-2}, and the diurnal mean shortwave cloud forcing from -50 to -150 W m^{-2}. Previous studies have shown that in regions of deep convection, large clouds and rain cells express greater organization into structures composed of convective core regions attached to stratiform anvil cloud and precipitation. Entrainment of moist, cloudy air from the stratiform anvil into the convective core helps to sustain convection against the entrainment of unsaturated air. Thus large clouds produce more rain, trap more terrestrial radiation and reflect more solar energy than do smaller clouds. The combined effect of increased forcing and increased spatial coverage means that larger clouds contribute most of the total forcing. Rain cells larger than 10^5 km^2 make up less than 2% of the rain cell population, yet contribute greater than 70% of the latent heating. Similarly, the clouds larger than 10^5 km^2, in which the largest rain cells are embedded, make up less than 3% of clouds, yet are the source of greater than 90% of the total thermodynamic forcing. Significant differences are apparent between the scales of latent heating and radiative forcing, as only about 25% of cloud area is observed to precipitate. The fraction of clouds that contain some rain increases dramatically from about 5% for the smaller scale (10^3 km^2) to as high as 90% for the largest scale considered here (10^6 km^2). The fractional area of the precipitating cloud ranges from 0.2 to 0.4 with a hybrid scale dependence. Greater than half of radiative forcing is provided by nonprecipitating anvil portions of deep convective cloud systems. The results presented here have significant implications for the parameterization of clouds and rain in GCMs and washout of solute trace gases and aerosols in chemistry and transport models.

3.1 Introduction

In the tropical regions of deep convection, latent heating and cloud-radiative interactions play an important role in the energy balance. Large and frequent cloud systems deposit the majority of the total latent heating of the atmosphere in the Tropics. This heating provides the energy to lift parcels to the tropopause and balance longwave cooling of the atmosphere. Excess latent heating in these regions establishes zonal and meridional heating gradients in the atmosphere that play a crucial role in large-scale dynamics. Model studies and measurements of the radiative effects of convective-cirrus cloud systems at the top of the atmosphere and surface have confirmed that, in addition to latent heating, clouds: (a) reduce the flux of longwave radiation to space (the cloud greenhouse effect), resulting in heating concentrated mostly in the atmosphere; and (b) enhance the reflection of solar energy back to space, resulting in a cooling concentrated mostly at the surface (Ramanathan 1987; Collins et al. 1996). These radiative processes are responsible for enhancing the atmospheric heating gradient while simultaneously reducing the surface heating gradient between deep convective regions and regions of large-scale subsidence. This effect operates on zonal circulations, for example over the tropical Pacific Ocean (Webster 1994), as well as meridional circulations such as the Indian monsoon (Ramanathan 1987).

Tropical convective clouds span a continuous spectrum of sizes, from a few tens of km^2 to millions of km^2. Thus we can expect that the thermodynamic forcing of the column by clouds exists on a corresponding spectrum of sizes. Clouds of different sizes, however, express significant structural differences. Studies of satellite images (Roca and Ramanathan 2000) and ground-based radar echoes (Houze and Betts 1981) suggest that small clouds are dominated by isolated convective elements while larger clouds express an organized structure of one or more deep convective cores attached to a broad stratiform anvil cloud. Boer and Ramanathan (1997) document a significant dependence of solar reflectivity and outgoing longwave radiation on cloud size in the tropical western Pacific. Houze (1989) presented

observations of the vertical latent heating profiles of organized convective cloud systems, and demonstrated that they peak higher in the troposphere than profiles of isolated convective cells. Hartmann et al. (1984) show that applying the vertical heating profile consistent with organized cloud structures in an atmospheric general circulation model (GCM) results in a more realistic simulation of the Walker circulation than the simulated circulation when the heating profile consistent with isolated convective cells is applied. In order to understand the link between cloud thermodynamic forcing and atmospheric dynamics, we have to determine the spatial scales of the forcing.

The Tropical Rainfall Measuring Mission (TRMM) satellite provides, for the first time, simultaneous measurements of the latent heating and radiative forcing of clouds from the same platform. In this study, these measurements are used to investigate the dependence of thermodynamic forcing on the horizontal scales of tropical convective clouds over the Indian Ocean during the winter monsoon. Cloud thermodynamic forcing averaged over individual clouds and rain cells is evaluated in order to reveal the horizontal scales at which these processes force the large-scale atmospheric circulation of the Indian Ocean monsoon region. Furthermore, the horizontal scale and magnitude of latent heating is compared to that of radiative forcing for typical clouds across the observed spectrum of sizes. Finally, the analysis provides a convenient means of evaluating the parameterization of clouds and convection in GCMs. The horizontal scales of clouds and rain cells will be compared to typical grid box sizes in GCMs of various resolutions as a simple means of comparing the naturally occurring scales of thermodynamic forcing features to the minimum scales represented explicitly in models. Properly accounting for the effects of clouds large enough to be resolved by the model, while also capturing the effects of the subgrid-scale clouds, and subgrid-scale variability within clouds, through a parameterization scheme is a particular challenge in light of the continuous spectrum of clouds sizes. Satellite studies such as this can help constrain the problem of distinguishing between resolved forcing and subgrid-scale

forcing. Note that in this paper, the term "resolved" will be used to refer to clouds and rain cells whose size exceeds the size of a single grid box. That a cloud or rain cell is resolved by this definition does not mean that smaller-scale processes imbedded within the cloud or rain cell, which may be responsible for the growth and maintenance of the feature, will be resolved.

Data are presented from January and February 1998, during the winter monsoon season. The tropical Indian Ocean consists of a large pool of warm water with surface temperatures typically greater than 300 K. During the winter monsoon, convergence of northeasterly surface winds off of the Asian continent with southeasterly winds from the southern Indian Ocean over these warm waters results in frequent convective activity (Krishnamurti et al. 1997). The result is a large sample of convective clouds that provide an ideal environment for studying the thermodynamic forcing of tropical clouds.

3.2 TRMM data

TRMM is the first satellite specifically designed for the measurement of rainfall. The satellite is a joint US-Japan project that has a passive microwave radiometer, a passive visible and infrared radiometer, and the first ever spaceborne rain radar (Kummerow et al. 1998). Rainfall is measured independently from each of the instruments and algorithms are being developed that combine measurements from each of the instruments. In addition to the rainfall measuring instruments, the satellite also measures top of the atmosphere radiative fluxes with the Cloud and the Earth's Radiant Energy System (CERES) instrument (Wielicki et al. 1996). The choice of orbit parameters for TRMM was made with the goal of measuring the variability of tropical rainfall on time-scales from diurnal to annual (Simpson et al. 1988). It flies at a low orbit (about 350 km), which allows sufficient resolution to capture features of individual clouds of scales larger than a few hundred km^2. The orbit is inclined at $35°$ and precesses such that all local hours are sampled approximately once per month.

3.2.1 Passive microwave rain measurements

Surface rain rate estimates for this study were made at 5 km $\times$ 7 km resolution using the TRMM Microwave Imager (TMI), a 9-channel passive microwave radiometer. The instrument is nearly identical to the Special Sensor Microwave Imager (SSM/I), currently operating on polar-orbiting satellites, with an additional, dual-polarized low-frequency channel at 10.7 GHz (2.8 cm wavelength). Passive microwave rain measurements rely on both the emission and scattering properties of rain and ice at microwave frequencies. Furthermore, because the response function for each channel peaks at a different altitude within the atmosphere, the instrument can retrieve information about the vertical profile of rain and ice. The rain rate retrieval algorithm used in this study is described by Kummerow et al. (1996). It makes use of these properties to couple the observed brightness temperatures with a mesoscale cloud model. The technique uses a large database of candidate vertical profiles of hydrometeors and corresponding surface rain rates generated by the model. A forward calculation of the brightness temperatures that would be measured by the instrument if the actual hydrometeor profile matched that of the model profile is performed for each profile in the database. Under the assumption that profiles in the database occur with the same relative frequency as those in nature, the retrieved profile and rain rate comprises a weighted average of the model profiles and rain rates. The weighting of each model profile is determined from the difference between the measured properties and the modeled properties such as microwave brightness temperatures and the ratio of convective rain to stratiform rain. Random errors in this technique are roughly 100% and are associated with the spread of rain rates that might result in a given set of measured brightness temperatures. The algorithm was applied to SSM/I data and compared with ground-based radar by Olson et al. (1999). A positive bias error of about 20% is found to be associated with overestimates at low rain rates. These errors were found to decrease with spatial averaging. Furthermore, this error may be reduced with the improved resolution and additional channels of the

TMI. Estimates of vertically integrated latent heating are made directly from the surface rain rate retrievals using

$$\int (LH)dz = \rho_w L_v R_s$$

which states that the latent heating (LH) integrated through the depth of the cloud is equal to the density of water (ρ_w) times the latent heat of vaporization (L_v) and the surface rain rate (R_s).

3.2.2 Top of the atmosphere radiative flux measurements

Radiative flux measurements at the top of the atmosphere were made using the CERES instrument. CERES is modeled after the Earth Radiation Budget Experiment (ERBE) instruments that flew on the *ERBS*, *NOAA-9*, and *NOAA-10* satellites. While new algorithms are being developed to retrieve top of the atmosphere fluxes, initial processing of CERES data has been performed using the same algorithms as were applied to the ERBE data. These ERBE-like products are used in this study. The resolution of the CERES instrument is 10 km × 10 km at nadir.

Cloud radiative forcing (CRF) is a simple and direct approach for estimating the effect of clouds on the radiative energy budget (Ramanathan 1987). CRF is the difference between the clear-sky radiative fluxes and the cloudy-sky fluxes, and thus reveals the radiative effects of clouds. Shortwave cloud forcing (C_s) is given by

$$C_s = S(\alpha_{clr} - \alpha),$$

where S is the incident solar flux, α_{clr} is the clear-sky albedo, and α is the cloudy albedo. Over oceans, the albedo of a cloud is almost always higher than the albedo of the surface. Therefore, C_s is usually negative and measures the cooling of the atmosphere-ocean column owing to the reduction in absorbed solar energy. Longwave cloud forcing (C_l) is given by

$$C_l = F_{clr} - F,$$

where F_{clr} is the clear-sky longwave flux to space and F is the cloudy longwave flux. Clouds are effective absorbers of longwave radiation and the upward flux of longwave energy above an overcast region is lower than if the region were clear. Thus C_l is positive and provides a measure of the increased longwave heating owing to the cloud. Typically, the cloudy-sky albedo and longwave flux values (α and F) are time- and space- averaged values. When CRF is calculated in this way, both the effects of the radiative properties of clouds as well as the effects of the frequency of cloud occurrence are accounted for. In this study, cloud forcing is averaged over regions that are entirely cloud covered. Thus α and F are the values for overcast skies. Cloud averaged CRF measurements used in this study represent the change in top of the atmosphere radiative flux at the location of the cloud from the clear-sky values owing to the presence of the cloud, and do not account for fractional cloud cover.

Clear-sky fluxes used in the cloud radiative forcing calculations are difficult to estimate on an instantaneous basis because of the high frequency of cloud cover. For this reason the monthly mean clear-sky longwave flux and albedo are used in place of the instantaneous clear-sky values. These are reported for 2.5° × 2.5° regions in the ERBE-like monthly mean product. To account for the variation of the clear-sky albedo with the solar zenith angle, only clear-sky albedo values measured at the same local hour as the pixel are used in calculating the monthly mean. To facilitate comparison of shortwave cloud forcing for clouds retrieved at different times of the day, and to account for presence of shortwave forcing only during daylight hours, all shortwave cloud forcing calculations are made using the diurnal mean solar insolation appropriate for the latitude of each cloud [calculated from Peixoto and Oort (1992), Eq. (6.18)].

The CERES radiometer measures radiances with an error of 1% or less. Additional uncertainty arises in converting the radiances measured from a single direction to top of the atmosphere fluxes resulting from radiation from all angles. For this conversion, an angular distribution model is used to estimate the anisotropy of the radiative flux. Reported errors

in instantaneous top of the atmosphere fluxes for the pixel-scale data are 12.1% in the shortwave and 5% in the longwave (Suttles et al. 1992; Wielicki et al. 1995). Monthly mean clear-sky fluxes have been used in place of instantaneous values. Natural variability in the tropical clear-sky albedo is 0.015, as reported by Conant et al. (1997). Variability in clear-sky longwave flux over the Indian Ocean for January, 1998 as measured by the CERES instrument is ± 5 W m^{-2}. For a typical clear-sky albedo of 0.08, these values correspond to an uncertainty of 7 W m^{-2} in C_s, hence -10 W m^{-2} is used as a threshold for detecting clouds. For typical cloudy conditions, uncertainties in CRF are ± 15 W m^{-2}.

3.2.3 Cloud and rain cell detection

Collocation of the rainfall and radiation datasets is achieved by binning each to the same 0.25° $\times$ 0.25° grid. The data are compiled into ensembles of rain cells (where precipitation reaches the ground) and clouds (which may or may not contain precipitation). Rain cells are identified using a simple clustering technique whereby adjacent pixels of nonzero rain rate are grouped into a single cell. Although a different algorithm is used here, the clustering scheme is identical to that described in Mapes and Houze (1993). Precipitating pixels must share a side to be included in the same cell. Cloudy regions that are not raining are excluded from the population of rain cells. The population of clouds is found by identifying contiguous regions that reflect greater than 10 W m^{-2} of diurnal mean solar energy over average clear-sky conditions. The same clustering technique as used to identify the rain cells is applied to the C_s data to identify the clouds. The terms "rain cell" and "cloud" are often used in the literature with various definitions. These terms will be used throughout this paper to refer specifically to the features identified using the thresholds and clustering technique described above.

The boundaries for this study are $\pm 20^{\circ}$ latitude and 40° -120° longitude. The swath width of the TMI is about 760 km. Although the CERES swath is wider, the CERES data are restricted to those data points that fall within the TMI swath in order match the data
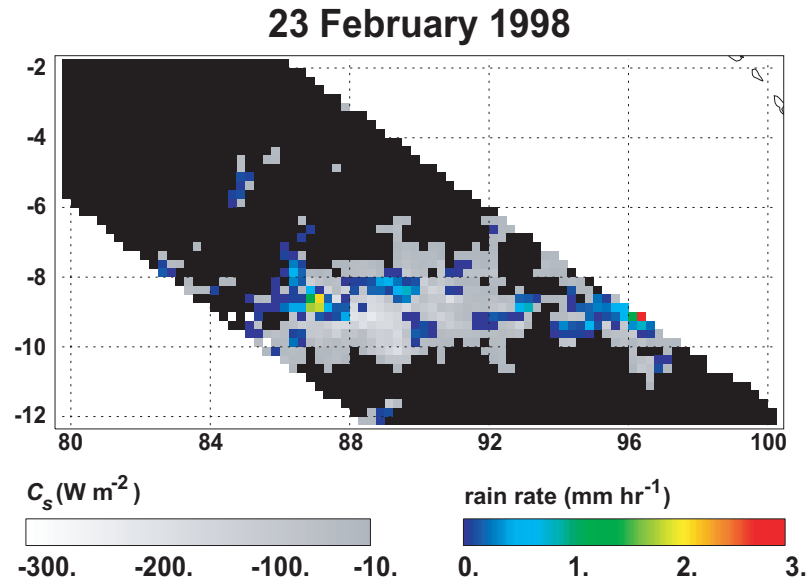
23 February 1998

Fig. 3.1. Clouds and rain cells detected by TRMM over the tropical Indian Ocean on 23 February 1998. Grid boxes where C_s is less than -10 W m^{-2} are shown in gray. Contiguous regions of such grid boxes are clustered into individual clouds. One large cloud is shown in the center of the swath with several smaller clouds surrounding it. Overlaid in color is surface rain rate. Contiguous regions of nonzero rain rate are clustered into rain cells. Rain cells always exist within a cloud. Several rain cells of varying size exist within the large cloud shown. Some of the surrounding clouds contain rain cells and others do not.

sets to the same grid. A land mask is applied and only 0.25° grid boxes lying entirely over ocean are included. Because shortwave reflectance properties are used to detect clouds, only satellite passes that occurred during daylight hours are used for the cloud statistics and the C_s statistics of rain cells. Furthermore, because at high solar zenith angles the incedent solar irradiance is low, which renders shortwave measurements highly uncertain at those times, only data acquired between 10 am and 3 p.m. (local time) are used for C_s measurements. Thus the full diurnal cycle of cloud amount is not accounted for in this study. All passes from all local hours are used for detecting rain cells. The CERES instrument is switched from a cross-track scanning pattern to a biaxial scanning pattern every third day. Data from the biaxial scan days is not dense enough to fill every 0.25° grid box at the edges of the swath. Thus no data was used from the biaxial scan days. Additionally, no CERES data was

available for Jan. 7 and 8. Thirty-eight days of data, for a total of 447 passes over the Indian Ocean region, are used in this study. Of these passes, 179 occurred in the middle of the day and were used for C_s measurements.

An example of the data for a pass over the Indian Ocean on 23 February 1998 is shown in Fig. 3.1. Here C_s is shown in gray-scale and surface rain rate is superimposed on color. A single large cloud appears in the center of the swath with several smaller clouds nearby. Within the large cloud are several rain cells of various sizes that are all attached to a large area of nonprecipitating anvil cloud. Some of the smaller clouds contain rain cells and others do not.

3.3 Spatial scales of clouds and precipitation

The horizontal scales of latent heating and CRF are revealed by the size distributions of rain cells and clouds. The numbers of rain cells and clouds detected in each size bin, from less than 10^3 km² to greater than 10^6 km², are shown in Fig. 3.2a (solid line and dotted line respectively). The lower and upper ranges of the scales are, respectively, limited by the resolution of the individual pixel and the swath width. The number of rain cells exceeds the number of clouds in most size bins because rain cells were detected using all passes of the satellite while clouds were detected using only midday passes. A total of 17,722 rain cells and 8707 clouds are included in the populations. Small cells and clouds dominate the populations with numbers decreasing steadily with size. The region greater than 5×10^5 km² is shaded in Fig. 3.2, and subsequent figures, to indicate that there is little confidence in the ability of the TRMM satellite to estimate rain cell and cloud size for those cells and clouds larger than 5×10^5 km². Because of the 760-km swath width, the sizes of clouds and cells in this region are likely to be underestimated. The placement of this gray region was tested against simulated clouds of a known size distribution by sampling the simulated clouds with the TRMM swath. The numbers of clouds were improperly sampled only within the gray region. The maximum sizes attainable for clouds and rain cells both fall within the gray region. Rain
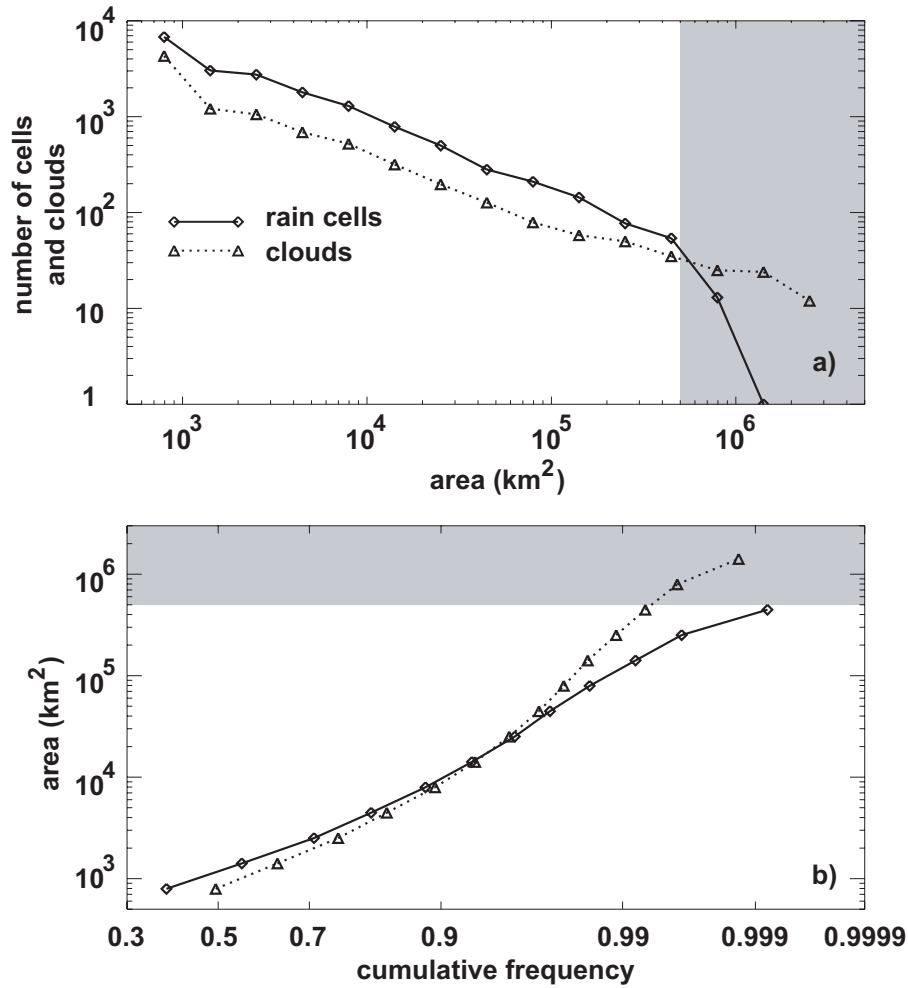
Fig. 3.2. (a) Number of rain cells (solid line) and clouds (dotted) as a function of area. (b) Cumulative frequency of occurrence of rain cells and clouds as a function of area. Cumulative frequency (abscissa) is shown on a normal probability scale.

cell number drops off rapidly at about 5×10^5 km². If rain cells in excess of 10^6 km² were to occur frequently, they would be truncated by the TRMM swath and would appear in the largest size bins in Fig. 3.2, as occurs in the distribution of clouds. However, only one rain cell larger than 10^6 km² is observed, indicating that the edge of the gray area in the figure corresponds roughly with the maximum rain cell size and confirms that the TRMM swath width is sufficient to capture most rain cells. On the other hand, geostationary satellite imagery confirms the presence of clouds in excess of 10^6 km² and even 10^7 km².

An alternative representation of the retrieved populations of rain cells and clouds for the 1998 winter monsoon are shown in Fig. 3.2b. The data are presented as the cumulative frequency of occurrence of rain cells and clouds on a log-probability plot. Plotted in this way, a straight line indicates that the data are lognormally distributed. The distribution of rain cells is approximately lognormal with deviations from lognormality at the small and large ends of the spectrum. The lognormal distribution of convective rain cells has been observed in radar echo studies conducted in tropical, midlatitude, oceanic, and continental convective regimes. Houze and Cheng (1977) and Lopez (1978), for example, demonstrate that in addition to radar echo size distributions, heights, and durations of radar echoes are also lognormally distributed. Deviations at the small and large extremes of the size range are likely due, in part, to limitation in the measurement resolution and observable swath width of the instrument, respectively. For rain cells, deviations at the large extreme may also be attributable to physical limitation of the rain cell growth process as mentioned above. Mapes and Houze (1993), for example, suggest 300 km as a limit for horizontal transport of precipitation-sized ice particles from the tops of convective cells before falling out, implying a low probability for rain cells exceeding 10^5 km^2.

Lognormal distributions are an outcome of processes exhibiting the law of proportionate effects (Aitchison and Brown 1957). This law states that as a variable progresses in steps, the amount the variable changes from its current value to the next value is a random proportion of its current value. That the law of proportionate effects may apply to the generation or growth processes of convective cells was discussed by Lopez (1977). In this paper it is proposed that either cell growth by merging of small convective elements or growth by scale-dependent entrainment may account for the lognormal distributions. An attempt to describe the behavior from first principles was provided by Raymond (1997), who suggests that mesoscale wind components as well as moisture flux components fit a lognormal distribution. Nevertheless, a complete explanation for the distributions remains

elusive.

The small clouds are distributed in a similar fashion as the rain cells. There is, however, a significant departure from the lognormal distribution appearing for clouds greater than 5×10^4 km^2, where large clouds appear more frequently than they would if the trend for the small clouds held for all clouds. Although we expect most of these clouds to be of convective origin, we would not necessarily expect that they adhere to the same distribution as the rain cells. Rain cells and small clouds are more directly related to convective-scale dynamics. The structure of the large cloud systems, however, can include a large anvil of cirrus cloud whose size may be more sensitive to larger-scale dynamics. Cirrus cloud may be advected by mean upper level winds or synoptic-scale divergence associated with large deep convective storms. A breaking scale is identified by Roca and Ramanathan (2000) in a satellite study of deep convective clouds over the Indian Ocean. For deep convective clouds greater than 10^4 km^2, greater organized structure is expressed in the form of deep convective core regions surrounded and connected by large stratiform anvil cloudiness. For clouds whose area exceeds the scale break, the fractional area of the cloud characterized by deep, undiluted convective activity increases with cloud size.

The likelihood that a cloud contains a precipitating region increases with size. The fraction of the number of clouds in each size bin that is observed to contain a rain cell is shown in Fig. 3.3 (solid line). Most observed clouds are not precipitating. Clouds smaller than 10^4 km^2 make up more than 85% of the cloud population, but only a small fraction of them contain any precipitation. For the subset of clouds that do contain some precipitation, the fraction of the cloud's area that is precipitating is shown in Fig. 3.3 (dashed line). Error bars in this and subsequent figures indicate one standard deviation of the mean in each size bin. Only 25-30% of the average cloud's area is raining. Clouds smaller than 2000 km^2 are too close to the resolution limit of the data to reliably estimate the raining fraction. For clouds from 2000 to 10^5 km^2 in size, the raining fraction of cloud decreases with
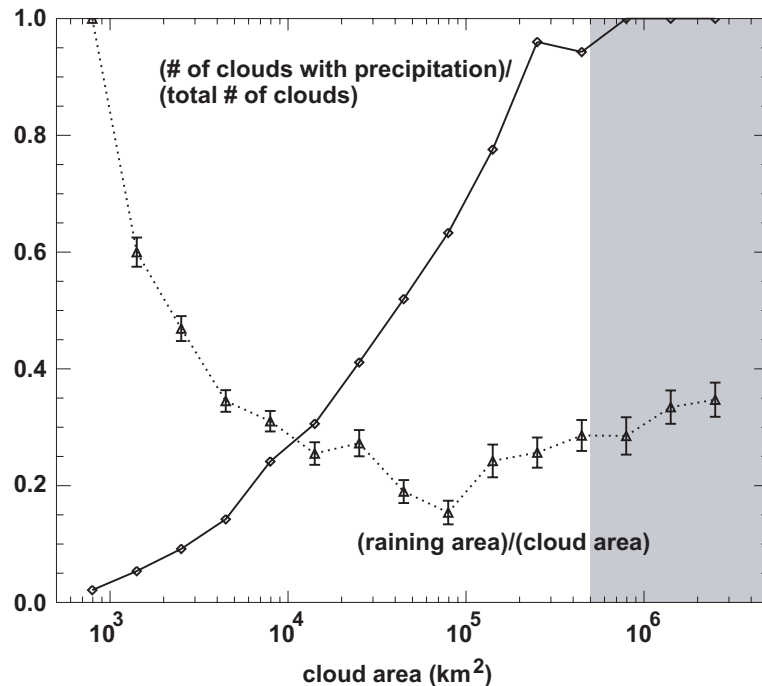
Fig. 3.3. Fraction of clouds that contain a rain cell (solid line). Also, the average fraction of cloud area taken up by rain cells (dotted), for clouds that contain at least one rain cell only. Both shown as a function of cloud area. Error bars indicate one standard deviation of the mean.

size, while for clouds larger than 10^5 km^2 raining fraction increases with size. The large clouds expressing an increasing scale dependence of raining fraction are the same clouds that deviate from the lognormal distribution as discussed above.

3.4 Thermodynamic forcing of rain cells

Embedded within some of the clouds lie the rain cells. Ground-based radar observations of rain cells made during the Global Atmospheric Research Program's Atlantic Tropical Experiment (GATE) confirmed that larger rain cells, termed mesoscale precipitating features (MPFs), express organized structure just as the large clouds do (Houze and Betts 1981). One or more deep convective core regions are connected to a broad region of stratiform precipitation in MPFs. The rain rate within the core is large and associated with vigorous updrafts. Precipitation within the stratiform region comprises ice detrained from the upper portion of the convective cell and is associated with much weaker, but more broadly
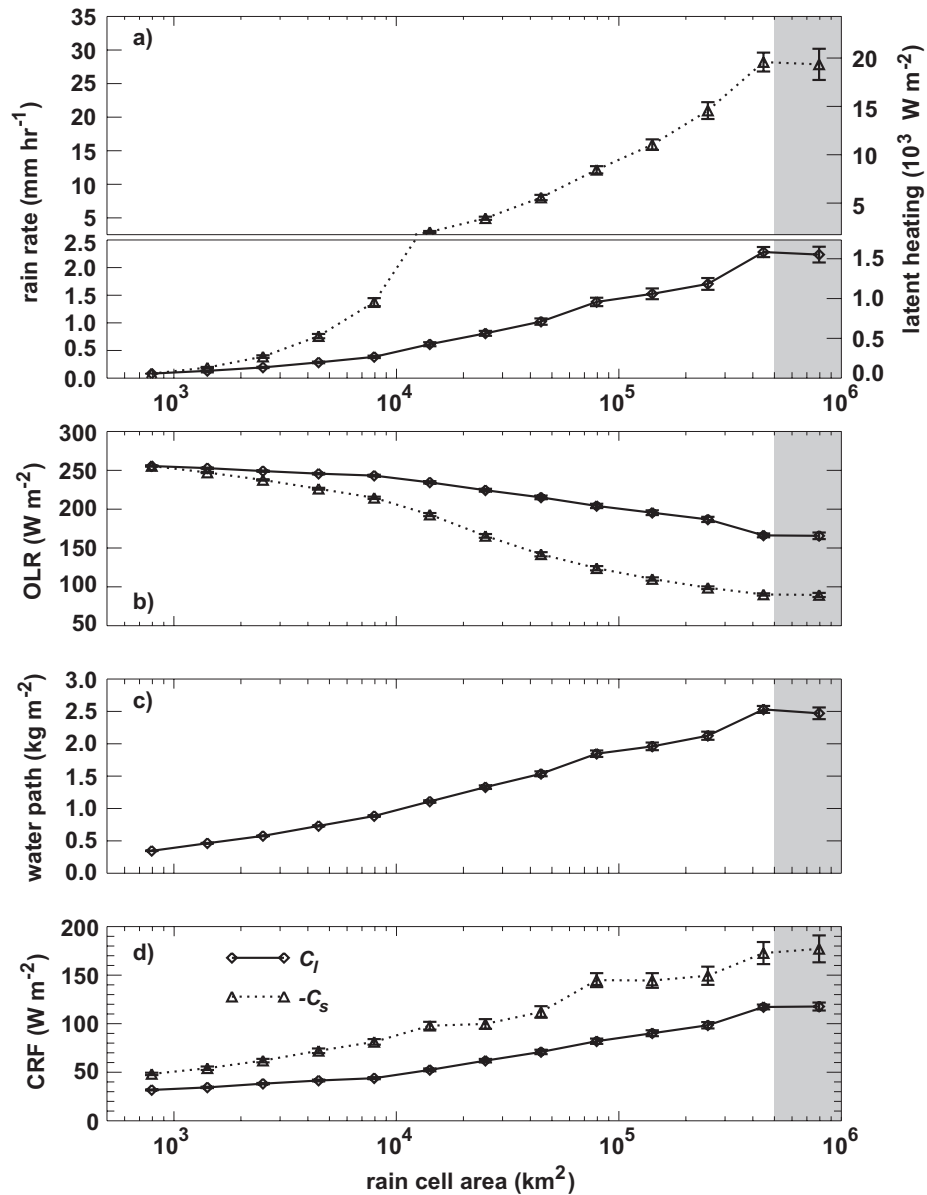
Fig. 3.4. Rain cell averaged properties as a function of rain cell area. (a) Rain rate (solid line) and $0.25^{\rm o}$ peak rain rate (dotted). Right side axis scaled to show vertically integrated latent heating. (b) OLR (solid) and $0.25^{\rm o}$ minimum OLR (dotted). (c) Ice+liquid water path. (d) C_l (solid) and $-C_s$ (dotted). Error bars indicate one standard deviation of the mean.

distributed, mesoscale motions. The organization of the larger precipitating clouds into

a mesoscale convective/stratiform structure appears to be associated with more intense

convective activity. The resolution of TRMM data is probably not sufficient to capture

individual convective showers, but the scales of the rain cells detected here provide an

indication of the scales at which the convective and stratiform showers organize themselves into the MPF structure. By using satellite measurements of rainfall, rain cells up to an order of magnitude larger than those measured during GATE are detected.

Rain cell properties as a function of rain cell size are shown in Fig. 3.4. Cell-averaged rain rate increases with rain cell size (Fig. 3.4a). Average latent heating of rain cells is proportional to the surface rain rate. The axis on the right side of Fig. 3.4a has been scaled to indicate the average vertically integrated latent heating from the retrieved rain rate. Latent heating increases with rain cell size, the largest cells releasing in excess of 1500 W m^{-2}. To indicate activity in the core of the MPFs, the size dependence of the rain rate in the 0.25° grid box where rain is heaviest is also shown in Fig. 3.4a (dashed line). Convective core rain rate increases rapidly with size, particularly for the larger rain cells. Lopez (1978) hypothesized rain cells exhibiting an organized MPF structure are protected from entrainment of dry environmental air by the surrounding moist environment of the stratiform anvil cloud, generating more rain and creating taller clouds (Houze and Cheng 1977).

Dense cumulonimbus clouds emit longwave radiation from just the top portion of the cloud, thus average outgoing longwave radiation (OLR, solid line in Fig. 3.4b) is an effective indicator of cloud-top height. OLR decreases with the size of the rain cells suggesting that, on average, larger rain cells penetrate to higher (colder) altitudes. The dotted curve in Fig. 3.4b is the scale dependence of OLR in the core area of the cell and indicates that the maximum height reached by a rain cell increases with size. The tops of the largest convective cores can penetrate to the tropopause.

Similarly, the vertically integrated liquid + ice water path increases with cell size (Fig. 3.4c). Apparently, larger convective cells are more effective at gathering moisture and distributing it vertically in the column. Were convective cells to grow primarily through the merger of small convective elements, there would be no appreciable source of additional moisture. Mesoscale motions within MPFs must directly enhance the convergence of

moisture below the cloud or act to concentrate the moisture captured from each element.

Longwave radiative forcing of a cloud measures the reduction in OLR attributable to the presence of the cloud. This effect increases with the horizontal scale of rain cells (Fig. 3.4d, solid line). Ramanathan (1977) demonstrated that the longwave forcing effect of a cloud is largely dependent on the difference between the surface temperature and the cloud-top temperature. The observed increase in cloud greenhouse effect with size is a result of the increase in cloud-top height with size discussed above.

Consistent with the deeper cloudiness indicated by the decreasing OLR and increasing water+ice path, the albedo, and thus shortwave cloud forcing, increases with rain cell size for nearly all size bins (Fig. 3.4d, dashed line). This indicates that the larger rain cells cool the column more effectively than the smaller rain cells.

3.5 Thermodynamic forcing of clouds

Figure 3.4 indicates that rain-cell-averaged latent heating exceeds rain-cell-averaged CRF by as much as one order of magnitude. Recall, however, that only 25% of cloud area is precipitating. The remaining three quarters of cloud area comprises nonprecipitating portions of extended anvil cloud associated with deep convective systems, dissipating deep convective clouds, and nonprecipitating shallow cumulous. Although this portion of the cloud area contributes no latent heating, it has significant shortwave and longwave radiative effects.

Deep convective clouds dominate the population of the larger winter monsoon clouds over the Indian Ocean (Roca and Ramanathan 2000) and give rise to extended decks of anvil cloud through detrainment of ice near the top of the cloud. Indeed, Webster and Stephens (1980) observed the ubiquitous presence of middle and high clouds, sometimes extending 750 km from the center of convection, over the South China Sea during the winter monsoon. Ramanathan and Collins (1991) suggested that the C_s of large decks
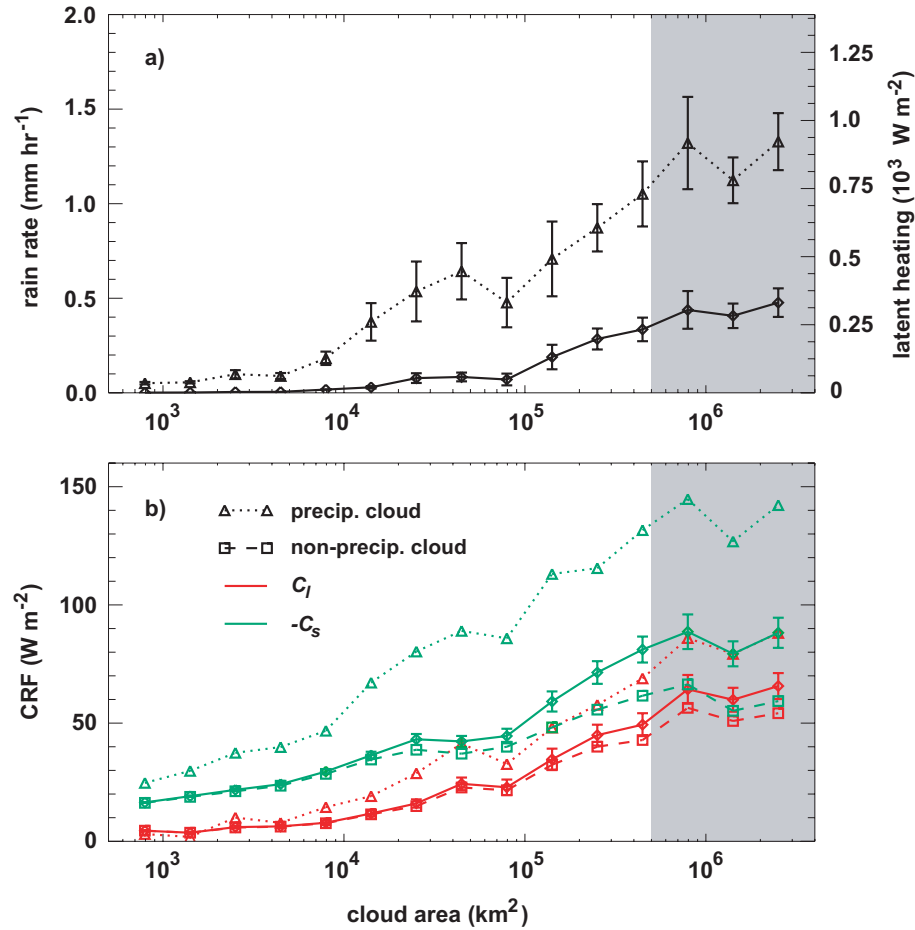
Fig. 3.5. Cloud averaged properties as a function of cloud area. (a) Rain rate; right side axis scaled to show vertically integrated latent heating. (b) C_l (red) and $-C_s$ (green). Solid lines are averages over entire cloud, dotted lines are averages over precipitating portions of cloud, and dashed lines are averages over non-precipitating portions of cloud. Error bars indicate one standard deviation of the mean.

of anvil cloud may strongly influence heating of the ocean surface in the western Pacific warm pool.

Latent heating as a function of cloud size is shown in Fig. 3.5a. The solid line denotes the latent heating averaged over the entire area of the cloud, and the dotted line is latent heating averaged over only the portion of cloud that contains rain. Latent heating increases with cloud size. For clouds larger than 10^5 km^2, the slope of the increase is more dramatic. Evidently, the larger, more organized clouds contain within them the larger rain

cells, which were found to be the dominant source of rainfall.

Similar to the results from the rain cells, cloud-averaged OLR decreases and albedo increases with cloud size (not shown). The corresponding dependence of CRF on cloud size is shown in Fig. 3.5b. Here C_l is shown in red and C_s in green. The dashed lines indicate averages over the nonprecipitating portions of cloud, the dotted lines are averages over the precipitating portions of cloud, and the solid lines are average over the entire cloud area. The distinction between precipitating cloud and nonprecipitating cloud is made based on the surface rain rate. Cloudiness that contains precipitation that reevaporates before striking the ground, which results in no net latent heating, is considered nonprecipitating. The goal here is to compare radiative forcing in cloudiness that contributes to net latent heating to cloudiness that does not. For small clouds, the average CRF for the nonprecipitating cloud is roughly equal to the total cloud-averaged CRF, since most of the small clouds do not contain any precipitation. For all cloud sizes, however, precipitating cloud averaged CRF exceeds nonprecipitating cloud CRF. This difference increases with cloud size. Also note that the C_s difference between precipitating cloud and nonprecipitating cloud is greater than that for C_l in the large clouds. Cells of active convection apparently generate thicker and more reflective clouds locally in the precipitating region. Although the extended anvil cloud is comprised of ice detrained at the top of the convective core, the material that remains aloft to produce the nonprecipitating cloud is less densely concentrated and distributed over a thinner vertical layer. Thus it is less effective at reflecting sunlight and trapping longwave energy. Note, however, that the magnitudes of CRF in the nonprecipitating regions are quite significant, exceeding 60 W m^{-2} in the largest clouds. The albedo of cirrus clouds is associated with its optical depth, which can depend on physical thickness of the cloud as well as the amount, size, and shape of ice crystals at the top of the cloud. Observations suggest, however, that albedo may be more sensitive to cloud thickness than microphysics (Heymsfield et al. 1998). Cloud-averaged latent heating exceeds cloud-averaged CRF by about a factor of 3 or 4 for

the large, deep convective clouds.

3.6 GCM parameterization of clouds and convection

Evaluating the properties of clouds as a function of their size provides a useful tool for evaluating the treatment of clouds in GCMs. The horizontal grid scales of many such models are within the horizontal scale of the larger clouds detected using the TRMM satellite. Using the definition stated in the introduction of the paper, these clouds are resolved by some models. While the aggregate effect of unresolved clouds and subgrid-scale processes within resolved clouds on the state of the surface-atmosphere column in each grid box must be determined using a parameterization scheme, some of the effects of resolved clouds may be determined explicitly and separate from the parameterization. Since clouds exist on all scales, from entirely subgrid-scale to fully resolved, separating the effects of clouds into resolved and unresolved forcing, while still capturing the proper scale dependence of forcing across the spectrum of cloud sizes, poses a particular challenge to modeling efforts.

The cumulative contribution of rain cells and clouds to the total thermodynamic forcing is shown in Fig. 3.6 as a function of the rain cell and the cloud size. The vertical dashed lines indicate typical values for the horizontal resolution of spectral GCMs at the equator. The enhanced forcing of larger rain cells, in conjunction with their larger spatial extent, mean that a relatively small number of large rain cells account for a large fraction of the total observed latent heating and CRF attributable to the rain cells (Fig. 3.6a). Rain cells greater than 10^5 km^2 make up less than 2% of all cells, yet contribute roughly 70% of latent heating.

Presented in this way, the data indicates the fraction of thermodynamic forcing contributed by rain cells that are resolved by the model and the fraction resulting from unresolved cells. Note however that, although the total dimension of a rain cell may be larger than the GCM resolution (*i.e.*, resolvable), there will be individual rain features that
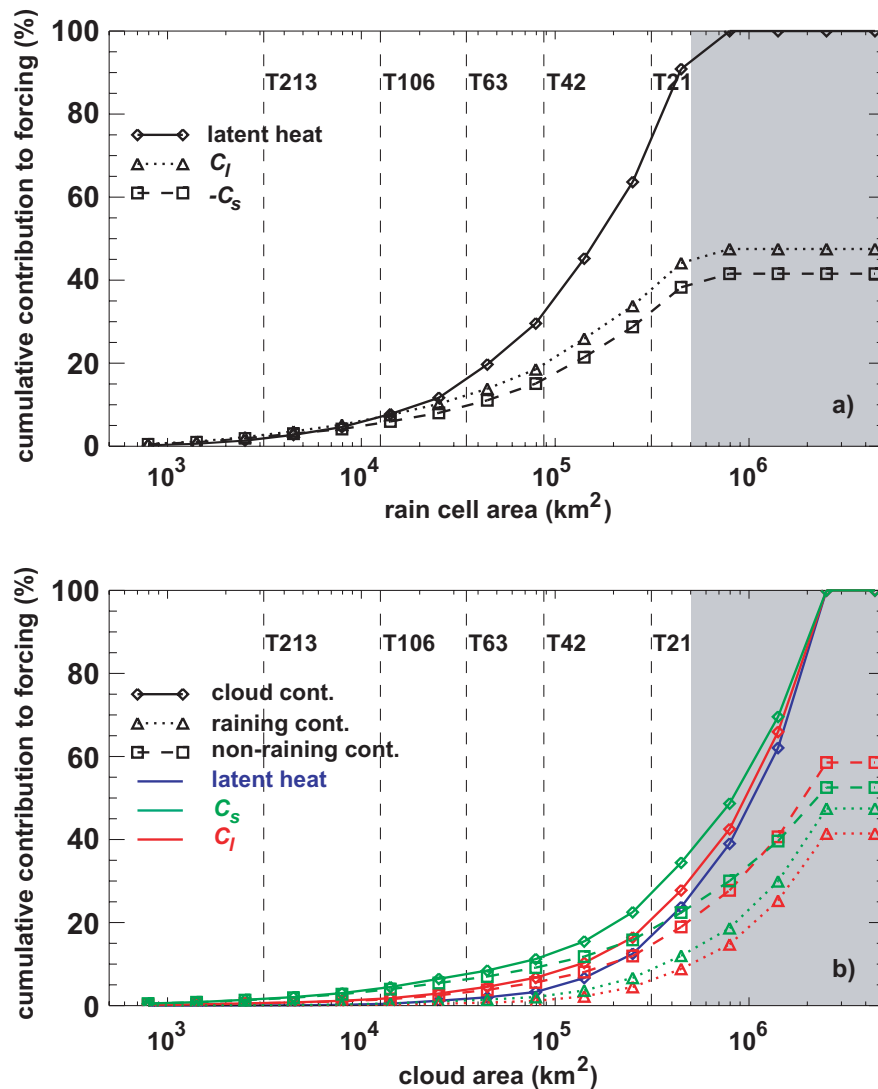
Fig. 3.6. (a) Cumulative contribution of rain cells to total latent heating (solid), C_l (dashed line) and C_s (dotted) as a function of rain cell area. (b) Same for clouds. Blue is latent heating, green is C_s and red is C_l. Solid lines are the contributions from the entire cloud, dotted lines are the contributions from the precipitating portions of cloud and dashed lines are the contributions from non-precipitating portions of cloud.

are subgrid-scale that need to be parameterized, even if the whole rain cell is resolvable.

The amount of latent heat and CRF attributable to resolved rain cells is a strong function

of model resolution. A GCM with the highest resolution, T213 (approx. 50 km × 50 km),

would resolve enough of the rain cells to account for virtually all of the rain cell forcing.

By resolving these rain cells, it is possible to identify such features in the model and test

the resolved physics, as well as the parameterizations of subgrid-scale processes, to see if they result in resolved rain cells that have scale dependent properties that are consistent with observed rain cells. Latent heating and CRF of monsoon rain cells in such a model should express a similar size dependence as shown in Fig. 3.4. A GCM at the lowest resolution (T21 = approx. 550 km × 550 km), however, would only resolve enough rain cells to account for about 30% of rain cell forcing.

As is the case with rain cells, the largest clouds contribute most of the thermodynamic forcing (Fig. 3.6b). Clouds larger than 10^5 km^2 contribute more than 80% of the latent heating (blue line), C_l (red lines), and C_s (green lines). The solid lines are the cumulative contribution of the entire area of the clouds in each size bin to the total cloud forcing. The dotted and dashed lines are the contributions of the precipitating area of cloud and the nonprecipitating area of cloud, respectively, to the total forcing. Note that the nonprecipitating cloud is a significant contributor to total CRF. While latent heating dominates CRF in rain cells, the nonprecipitating cloud, because of its spatial extent, contributes more than half of the total observed CRF.

That the largest clouds provide such a large contribution to total forcing is important, because even coarse-resolution GCMs should, in principle at least, resolve many of these large clouds. As with the resolved rain cells, care must be taken as GCMs will still need parameterizations for some subgrid-scale features to properly simulate these large clouds. Even at the coarsest model resolution, clouds contributing greater than 80% of the observed latent heating are resolved. The rain cells in these clouds may not be resolved, as discussed above, but this result indicates that the large clouds contain several rain cells and that these are the larger rain cells that are contributing most of the latent heat. CRF, however, is a process that scales with the size of the entire cloud. A GCM at T21 resolution will resolve clouds contributing greater than 75% of CRF. At a resolution of T63 (approx. 200 km × 200 km) enough clouds are resolved to account for greater than 90% of CRF.

Comparison of the scale dependence of cloud frequency and CRF in GCMs to the trends detected by TRMM provides a means of validating of the treatment of clouds in GCMs. The dependence of rainfall, cloud liquid water path, and other properties on cloud size for resolved tropical Pacific clouds in a GCM is demonstrated in Zhang et al. (1999). They also compare modeled cloud distributions to distributions observed by the GMS satellite to identify strengths and weaknesses in the model's cloud parameterization scheme.

The cumulative contributions to the thermodynamic forcing of clouds and rain cells (Fig. 3.6) indicate that larger clouds and rain cells, known to be associated with organized convection (Roca and Ramanathan 2000), are the dominant source of forcing. However, we still need to understand how individual convective elements, with scales of tens of kilometers, organize themselves to give rise to the large-scale forcing. GCMs have to deal with this subgrid-scale problem rigorously for simulating the observed importance of the "resolved"-scale clouds.

3.7 Discussion and conclusion

Thermodynamic forcing of the ocean-atmosphere column by clouds is provided by latent heating and cloud-radiative interactions. Measurements from the TRMM satellite of surface rain rate and top of the atmosphere radiative fluxes provide estimates of the total thermodynamic forcing of winter monsoon clouds over the Indian Ocean. The total latent heating averaged over all January and February 1998 passes over the Indian Ocean (including clear-sky regions) is 118 W m^{-2}. For C_l, the average is 22 W m^{-2} and average C_s is -32 W m^{-2}. Assembling the data into populations of rain cells and clouds highlights the horizontal scales at which the latent heating and CRF processes operate, and allow for the comparison of the magnitudes of latent heating and CRF on the scales of individual clouds.

Thermodynamic forcing increases with size for both the rain cells and the clouds. The combined effects of increased coverage and increased thermodynamic forcing exhibited by the larger clouds in the study, implies an important role for large clouds in the overall

heating and cooling of the column. Less than 2% of rain cells are found to contribute roughly 70% of the total latent heating. All of these cells are between 10^5 and 10^6 km^2. In 447 passes over the Indian Ocean during the two months of observations, this amounted to only 499 rain cells, or roughly one cell at the dominant scale for each pass. Riehl and Malkus (1958) concluded that a relatively few deep convective towers (1500-5000 throughout the equatorial region from 10°N to 10°S) carry enough heat to the upper troposphere to balance the radiative cooling and poleward transport in the upper branch of the Hadley circulation. Rain cells are not directly comparable to the deep convective towers addressed by Riehl and Malkus because several such towers may exist within a single rain cell. Riehl and Malkus proposed that the towers representing the core regions of undiluted, penetrative convection are 3 to 5 km on a side – numbers that were confirmed by observations during GATE (LeMone and Zipser 1980). While the deep, undiluted towers are critical for transporting heat from the boundary layer to the tropopause, the emphasis in the present study is on the scales forcing the large-scale features of the tropical monsoon circulation. Consideration of the towers alone ignores the important contribution to forcing from the stratiform anvil precipitation. Mapes and Houze (1995) demonstrate that the large-scale environment in which the deep convective clouds are embedded respond to heating from both stratiform precipitation and convective precipitation, and hence the entire rain cell. A complementary calculation to that of Riehl and Malkus can now be made to determine how many rain cells at the dominant scale are required at a given time to provide the 118 W m^{-2} latent heating of the winter monsoon. Taking 2×10^5 km^2 as a representative size for a deep convective rain cell, with an area averaged latent heating of 1000 W m^{-2}, and 4×10^7 km^2 as the area of the tropical Indian Ocean, it takes only about 20 rain cells at a time to provide the necessary latent heat.

Only 25-30% of a typical monsoon cloud is raining. In contrast to the latent heating, which is confined just to the rain cells within a cloud, CRF is distributed throughout the

entire area of the cloud system. The dominant scale of the clouds is at least one order of magnitude larger than that of the rain cells. Clouds greater than 10^5 km^2, comprising less than 3% of all observed clouds, are found to contribute 90% of the total CRF. Indeed, many of these clouds are beyond the size range that the TRMM swath can capture. Although operating at different scales, latent heating and CRF remain linked since the same clouds that provide most of the CRF also provide most of the latent heat. Evidently, the largest rain cells are embedded only within the largest clouds.

Increasing thermodynamic forcing with cloud size is likely a reflection of the dominance of organized deep convection at larger cloud sizes in the tropical Indian Ocean. One or more large precipitating regions in the core of the cloud system are associated with vigorous convective motions penetrating to the tropopause. Within these precipitating regions, latent heating exceeds CRF by one order of magnitude. Large amounts of ice are detrained from the tops of the convective cores and mesoscale circulations effectively disperse the anvil material. The number distribution of these giant organized cloud systems reveals a separate regime from the smaller scale, lognormally distributed rain cells, and shallow cumulus.

The nonprecipitating cloud contributes no latent heating, yet has significant radiative properties and, because of its spatial extent, contributes more than half of the total CRF. Within a rain cell, atmospheric latent heating can exceed top of the atmosphere CRF by up to a factor of 10. Averaged over the entire area of a deep convective cloud system, however, latent heating exceeds CRF by only a factor of 3 or 4. The magnitude of CRF increases with cloud size. Cooling owing to C_s exceeds the warming from C_l at all size bins such that the largest clouds detectable by TRMM provide a net cooling of the column of about 30 W m^{-2}. In addressing the response of the large-scale circulation to the thermodynamic forcing, it is important to consider the vertical distribution of the forcing. Table 3.1 shows the partitioning of each component of the thermodynamic forcing for the average overcast

Table 3.1. Vertical distribution of the thermodynamic forcing for an average cloud (W m^{-2}).

	Latent heat[*]	C_s	C_l
Top of atmosphere	0	-70	48
Atmosphere	216	18	41
Surface[**]	0	-88	7

[*] Latent heat contained within 25% of the average cloud's total area.
[**] Surface CRF estimated from ratios of surface forcing to TOA forcing observed over the Central Equatorial Pacific Ocean during CEPEX (Collins et al. 1996).

region between the top of the atmosphere, the atmosphere and the surface. These values differ from those discussed at the beginning of this section because the clear-sky regions are excluded here. Also recall that cloud-averaged forcing is only determined from midday passes of the satellite, so these values are subject to large uncertainties due to poor sampling of the diurnal cycle of clouds and rain cells. Latent heating occurs entirely within the atmospheric layer, providing additional buoyancy and allowing clouds to penetrate deeper. CRF is observed by satellite at the top of the atmosphere. This is a forcing of the entire ocean-atmosphere column and hence is the sum of CRF in the atmosphere and at the ocean surface. While net cooling due to CRF is smaller than the magnitudes of either C_l or C_s, partitioning of each between the surface and atmosphere is different, and care must be taken in interpreting the cancellation of C_l and C_s. Observations of CRF at the surface and top of the atmosphere were made for deep convective clouds during the Central Equatorial Pacific Experiment (CEPEX) by Collins et al. (1996). The ratio of C_s at the surface to C_s at the top of the atmosphere was estimated to be between 1 and 1.5 indicating that in the absence of solar absorption in clouds, all of the cooling is felt at the surface. If moderate solar absorption occurs, then surface cooling is even larger to balance the atmospheric heating. The net result in either case is to stabilize the entire column. Taking an intermediate value of 1.25 for this ratio leads to a cloud average cooling of the surface of -88 W m^{-2} and a moderate heating of the atmosphere of 18 W m^{-2} from absorbed sunlight. Here C_s in the atmosphere may have a limited impact on the direct response of the atmosphere to the

cloud in light of the large atmospheric latent heating. The strong surface cooling, however, has a significant effect on the tropical circulation on longer timescales (*e.g.*, Ramanathan and Collins 1991). In contrast, the ratio of surface C_l to top of the atmosphere C_l was estimated at between 0 and 0.3, meaning that surface heating due to longwave cloud radiation is small. Here C_l is expressed as a large convergence of upward longwave flux in the cloud that reinforces the latent heating by further destabilizing the cloud layer. Adopting an intermediate ratio of 0.15, cloud-averaged C_l in the atmosphere is 41 W m^{-2} leaving only 7 W m^{-2} to heat the surface. Values for surface and atmosphere radiative forcing are highly uncertain ($\pm 50\%$). In situ measurements of surface forcing are required to confirm these values for monsoon clouds.

Satellite measurements of the cumulative contributions of clouds to thermodynamic forcing provide a means of comparing the net effects of clouds resolvable by GCMs to subgrid-scale clouds. Clouds contributing the majority of thermodynamic forcing occur at scales larger than a grid cell in many models. Measurements of the scale dependence of cloud properties can be compared with those of modeled clouds to validate the treatment of resolved clouds in GCMs. The dominance of such large clouds in the thermodynamic forcing of the atmosphere in the tropical monsoon environment underscores the importance of the processes that organize convection in large-scale disturbances and their representation in models.

References

Aitchison, J. and J. A. C. Brown, 1957: *The Lognormal Distribution*. Cambridge University Press, 176 pp.

Boer, E. R. and V. Ramanathan, 1997: Lagrangian Approach for Deriving Cloud Characteristics from Satellite Observations and its Implications to Cloud Parameterization. *J. Geophys. Res.,* **102**, 21,383-21,399.

Collins, W. D., F. P. J. Valero, P. J. Flatau, D. Lubin, H. Grassl and P. Pilewskie, 1996: Radiative Effects of Convection in the Tropical Pacific. *J. Geophys. Res.,* **101**, 14,999-15,012.

Conant, W. C., V. Ramanathan, F. P. J. Valero, J. Meywerk, 1997: An Examination of the Clear-Sky Solar Absorption over the Central Equatorial Pacific: Observations versus Models. *J. Climate,* **10**, 1874-1884.

Hartmann, D. L., H. H. Hendon, and R. A. Houze, 1984: Some Implications of the Mesoscale Circulation in Tropical Cloud Clusters for Large-Scale Dynamics and Climate. *J. Atmos. Sci.,* **41**, 113-121.

Heymsfield, A. J., G. M. McFarquhar, W. D. Collins, J. A. Goldstein, F. P. J. Valero, J. Spinhirne, W. Hart and P. Pilewski, 1998: Cloud Properties Leading to Highly Reflective Tropical Cirrus: Interpretations from CEPEX, TOGA COARE, and Kwajalein, Marshall Islands. *J. Geophys. Res.,* **103**, 8805-8812.

Houze, R. A., 1989: Observed Structure of Mesoscale Convective Systems and Implications for Large-Scale Heating. *Q. J. R. Meteorol. Soc.*, **115**, 425-461.

Houze, R. A., and C.-P. Cheng, 1977: Radar Characteristics of Tropical Convection Observed During GATE: Mean Properties and Trends Over the Summer Season. *Mon. Wea. Rev,* **105**, 964-980.

Houze, R. A., and A. K. Betts, 1981: Convection in GATE. *Rev. Geophys. Space Phys.,* **19**, 541-576.

Krishnamurti, T. N., B. Jha, P. J. Rasch and V. Ramanathan, 1997: A High Resolution Global Reanalysis Highlighting the Winter Monsoon. Part 1, Reanalysis Fields. *Meteorol. Atmos. Phys.,* **64**, 123-150.

Kummerow, C., W. S. Olson and L. Giglio, 1996: A Simplified Scheme for Obtaining Precipitation and Vertical Hydrometeor Profiles from Passive Microwave Sensors. *IEEE Trans. Geosci. Remote Sensing,* **34**, 1213-1232.

Kummerow, C., W. Barnes, T. Kozu, J. Shiue and J. Simpson, 1998: The Tropical Rainfall Measuring Mission (TRMM) Sensor Package. *J. Atmos. Ocean Technol.,* **15**, 809-817.

LeMone, M. A. and E. J. Zipser, 1980: Cumulonimbus Vertical Velocity Events in GATE. Part I: Diameter, Intensity and Mass Flux. *J. Atmos. Sci.*, **37**, 2444-2457.

Lopez, R. E., 1977: The Lognormal Distribution and Cumulus Cloud Populations. *Mon. Wea. Rev.*, **105**, 865-872.

Lopez, R. E., 1978: Internal Structure and Development Processes of C-Scale Aggregates of Cumulous Clouds. *Mon. Wea. Rev.,* **106**, 1488-1494.

Mapes, B. E. and R. A. Houze, 1993: Cloud Clusters and Superclusters over the Oceanic Warm Pool. *Mon. Wea. Rev.,* **121**, 1398-1415.

Mapes, B. E. and R. A. Houze, 1995: Diabatic Divergence Profiles in Western Pacific Mesoscale Convective Systems. *J. Atmos. Sci.*, **52**, 1807-1828.

Olson, W. S., C. D. Kummerow, Y. Hong and W.-K. Tao, 1999: Atmospheric Latent Heating Distributions in the Tropics Derived from Satellite Passive Microwave Radiometer Measurements. *J. Appl. Met.,* **38**, 633-664.

Peixoto, J. P. and A. H. Oort, 1992: *Physics of Climate.* American Institute of Physics, 520 pp.

Ramanathan, V., 1977: Interactions between Ice-Albedo, Lapse-Rate and Cloud-Top Feedbacks: An Analysis of the Nonlinear Response of a GCM Climate Model. *J. Atmos. Sci.,* **34**, 1885-1897.

Ramanathan, V., 1987: The Role of Earth Radiation Budget Studies in Climate and General Circulation Research. *J. Geophys. Res.,* **92**, 4075-4095.

Ramanathan, V. and W. D. Collins, 1991: Thermodynamic Regulation of Ocean Warming by Cirrus Clouds Deduced from Observations of the 1987 El Niño. *Nature,* **351**, 27-32.

Raymond, W. H., 1997: A Theoretical Evaluation of the Relevance of Lognormal Distributions for the Moisture Flux and Wind Components. *Mon. Wea. Rev.*, **125**, 3018-3023.

Riehl, H. and J. S. Malkus, 1958: On the Heat Balance in the Equatorial Trough Zone. *Geophysica,* **6**, 503-538.

Roca, R. and V. Ramanathan, 2000: Scale Dependence of Monsoonal Convective Systems over the Indian Ocean. *J. Climate,* **13**, 1286-1289.

Simpson, J., R. F. Adler, and G. R. North, 1988: A proposed Tropical Rainfall Measuring Mission (TRMM) Satellite. *Bull. Amer. Meteor. Soc.,* **69**, 278-295.

Suttles, J. T., B. A. Wielicki, and S. Vemury, 1992: Top-of-Atmosphere Radiative Fluxes: Validation of ERBE Scanner Inversion Algorithm Using *Nimbus-7* ERB Data. *Bull. Amer. Meteor. Soc.,* **31**, 784-796.

Webster, P. J., 1994: The Role of Hydrological Processes in Ocean-Atmosphere Interactions. *Rev. Geophys.* **32**, 427-476.

Webster, P. J. and G. L. Stephens, 1980: Tropical Upper-Tropospheric Extended Clouds: Inferences from Winter MONEX. *J. Atmos. Sci.,* **37**, 1521-1541.

Wielicki, B. A., R. D. Cess, M. D. King, D. A. Randall and E. F. Harrison, 1995: Mission to Planet Earth: Role of Clouds and Radiation in Climate. *Bull. Amer. Meteor. Soc.,* **76**, 2125-2153.

Wielicki, B. A., B. R. Barkstrom, E. F. Harrison, R. B. Lee, G. L. Smith and J. E. Cooper, 1996: Clouds and the Earth's Radiant Energy System (CERES): An Earth Observing System Experiment. *Bull. Amer. Meteor. Soc.,* **77**, 853-868.

Zhang, G. J., D. Zurovac-Jevtic and E. R. Boer, 1999: Spatial Characteristics of the Tropical Cloud Systems: Comparison Between Model Simulation and Satellite Observations. *Tellus*, **51A**, 922-936.

Chapter 4

Spatial and Temporal Scales of Precipitating Tropical Cloud Systems in Satellite Imagery and the NCAR CCM3

Abstract

Testing general circulation model parameterizations against observations is traditionally done by comparing simulated and observed, time-averaged quantities, such as monthly mean cloud cover, evaluated on a stationary grid. This approach ignores the dynamical aspects of clouds, such as their lifecycle characteristics, spatial coverage, temporal duration, and internal variability. In this study, a complimentary Lagrangian approach to the validation of modeled tropical cloudiness is explored. An automated cloud detection and tracking algorithm is used to observe and track overcast decks of cloud in a consecutive set of hourly METEOSAT-5 images and the National Center for Atmospheric Research Community Climate Model version 3 (NCAR CCM3). The algorithm is applied to the deep convective cloud systems of the tropical Indian Ocean region during a 49 day period of the 1999 winter monsoon season. Observations of precipitation are taken from the Tropical Rainfall Measuring Mission (TRMM) satellite in addition to a METEOSAT-5 infrared rainfall technique that is calibrated using the TRMM data.

Clouds, defined as overcast decks, are observed spanning spatial scales from 25 km² to greater than 10^7 km², as well as temporal scales from 1 hour to greater than 100 hours. Semi-permanent decks of anvil and cirrus cloud, with numerous regions of deep convection embedded within, dominate total cloud cover. The peak in total spatial coverage of such cloud systems lags the peak in coverage by deep convective cloudiness by 12-15 hours because of the residence time of cirrus cloud material and the time it takes the material to

spread from the regions of convection. At scales greater than 10^6 km^2 the size distribution of simulated clouds is biased such that the dominant scale of clouds is several million square-km larger than the dominant scale of observed clouds. Virtually all of the simulated precipitation occurs at rain rates lower than 2 mm hr^{-1}, while as much as 25% of observed precipitation occurs at rain rates higher than 2 mm hr^{-1}. Precipitation associated with deep convection in observed semi-permanent cloud systems is organized into more localized mesoscale structures of adjacent convective cells attached to stratiform precipitation regions. A separate analysis of TRMM data (Wilcox and Ramanathan 2001) determined that such structures can exceed the size of grid cells in coarse-grid global models and have area-averaged rain rates up to and exceeding 2 mm hr^{-1}. These mesoscale convective systems are responsible for the extreme, episodic precipitation events that are not parameterized in the model. The simulated cloud systems gently precipitate throughout their duration and everywhere within their boundaries. The model lacks a process that acts to organize the convective cells within fewer grid cells, in addition to a representation of the observed stratiform precipitation structures. A modification to CCM3 is tested that is intended to account for the evaporation of upper-level precipitation in mid-level mesoscale downdrafts. The modification results in only a slight change in domain-averaged precipitation. However, it causes a significant shift in the distribution of precipitation toward higher rain rates that is more consistent with the distribution of TRMM observed rain rates. The modification demonstrates the sensitivity of the model to one important component of mesoscale organized convection.

4.1 Introduction

Condensed moisture, in the form of clouds and precipitation, is a key component of the climate system and continues to be a challenge for global models of the atmospheric general circulation. Latent heating from the condensation of precipitation is the largest source of heat driving atmospheric circulations. Variability of precipitation in time and space has important impacts on ecosystems and societies. Uncertainties in feedbacks associated with cloud cover and radiative forcing remain a leading source of uncertainty in greenhouse warming predictions (Houghton et al. 2001). Accurate, quantitative predictions of condensed moisture remain a challenge for global models because of their dependence upon processes, such as cumulus convection and thermodynamic phase changes, that often occur on time and space scales that are small relative to the time steps and grid cells of such models. Progress in this matter is further hindered by a lack of available observations across the necessary scales to constrain the problem.

Validation of the representation of moist processes in models is typically approached by means of Eulerian analysis schemes whereby time and space averages of simulated and observed quantities, such and surface rain rate or fractional cloud cover, are evaluated over stationary grids. Presented in this study is a Lagrangian analysis scheme, similar to the scheme developed by Boer and Ramanathan (1997), whereby the boundaries of clouds are identified and tracked in order to reveal the spatial and temporal scales of clouds and precipitation. This scheme was further refined to distinguish between precipitating and non-precipitating cloud systems by Wilcox and Ramanathan (2001). The analysis scheme is intended as a complement to the traditional Eulerian approach by identifying cases where the physical properties of cloud systems may be improperly simulated even when time- and space-averaged quantities agree with observations. Statistics are compiled and compared based on large ensembles of both observed clouds and modeled clouds whose properties, such as spatial coverage, temporal duration and cloud-averaged precipitation rate, have been

observed throughout the lifecycle of each cloud.

This study focuses specifically on deep convective clouds located over the tropical Indian Ocean during the winter monsoon season. Cloud observations are made using the METEOSAT-5 geosynchronous satellite. Rain rate estimates are also made using the infrared channel of METEOSAT-5 by means of a cloud-top temperature proxy that is tuned using simultaneous measurements from the TRMM satellite. Further comparisons of simulated and observed rain rate distributions are made using only TRMM data. The METEOSAT-5 imagery provide the ability to observe cloud systems spanning spatial scales from 25 km^2 to greater than 10^7 km^2, and temporal scales as small as 0.5 hours. The observed cloud systems will be compared with simulated cloud systems from the NCAR CCM3 global atmospheric model.

As climate models evolve toward parameterization schemes that are more physically based, it should be expected that elements, such as clouds, which result from a combination of several independently parameterized processes, should accurately represent the behavior of complex, natural cloud systems. In regions of tropical deep convection, clouds arise primarily through the process of moist convection. The organization of convection into adjacent convective cells and mesoscale circulations (Houze and Betts 1981) results in precipitation structures that can exceed 10^6 km^2 (Wilcox and Ramanathan 2001). Convective updrafts transport condensate to the middle and upper troposphere where detrained condensate either precipitates, or remains suspended as large and persistent decks of cirrus cloud. Precipitating drops result from diffusion and coalescence within convective cells and the settling and melting of hail and graupel in mesoscale anvil circulations. Each of these processes is parameterized separately in GCMs, and the links between them are often absent. In this study the boundaries of clouds are chosen such that entire overcast cloud systems, including deep convection imbedded within extended cirrus decks, are grouped together. Thus the analysis provides a test of how well simplified numerical representations replicate

complete natural cloud systems that result from the linked processes listed above.

Increasingly, global GCMs are being coupled to chemical and aerosol transport models for the study and prediction of aerosol/climate interactions. For soluble species, the residence time in the atmosphere can be as short as 5-15 days because of the efficient removal by precipitation (Balkanski et al. 1993; Rasch et al. 2001). In this case it is crucial to validate the spatial and temporal distribution of precipitation at the scales of individual cloud systems. The following analysis identifies biases in the distribution of precipitation that may have significant implications for the simulated transport of soluble constituents.

4.2 Data and methodology

Images from the METEOSAT-5 geosynchronous satellite are used to identify clouds, measure their sizes, estimate their area-averaged rain rates and track them in time. METEO-SAT-5 provides half-hourly images from two channels in the infrared region of the spectrum and one in the visible. For this study, only brightness temperatures from the infrared window (IR) channel (10.5 - 12.5 µm) and the infrared water vapor band (WV) channel (5.7 - 7.1 µm) are used. The visible channel data is not used because clouds are tracked through the nighttime hours. The satellite was moved by the European Organization for the Exploration of Meteorological Satellites (EUMETSAT) to its present location above the equator at 63 degrees east longitude in support of the Indian Ocean Experiment (INDOEX). The raw data were gridded by EUMETSAT to a 5 km. $\times$ 5 km. grid prior to being transferred to the INDOEX science team. The infrared window channel and water vapor channel images are distributed as digital counts which are converted to brightness temperatures (T_{IR} and T_{WV} respectively) using calibration coefficients provided by EUMETSAT. The coefficients are determined by comparing the counts to calculated radiances for a subset of clear sky oceanic pixels where colocated reanalysis and radiosonde profiles are used as input to a radiative transfer model.

The bounds for this study are 40 to 120 degrees east longitude and -20 to 20 degrees

Table 4.1. METEOSAT-5 pixel classification scheme.

classification	brightness temperature (K)
deep convection/anvil	$T_{IR} < 240$
shallow conv./thick cirrus	$240 <= T_{IR} < 280$
thin cirrus	$T_{IR} >= 280,\ T_{WV} < 245$
clear sky or broken cloud[*]	$T_{IR} >= 280,\ T_{WV} > 245$

[*]   not included in the cloud detection or tracking analysis.

latitude. METEOSAT-5 images from 1 Jan. through 18 Feb. 1999 are used. Calibration coefficients were not reported for six images during the period. For these cases, the coefficients from the previous image are used and visual inspection of the retrieved cloud maps indicated that the affected images fit smoothly into the context of the surrounding images. Following 18 Feb. 1999, contamination of the images by direct sunlight near local midnight resulted in gaps of several hours in the record, thus only the 49 day period between 1 Jan. and 18 Feb. is included in the study.

4.2.1 Pixel classification and cloud detection

For the purposes of this study, a cloud is defined as a set of contiguous overcast pixels. In order to identify such regions in the METEOSAT-5 images, each pixel is placed in one of four classifications. Pixels with T_{IR} less than 240 K are labeled "deep convection/anvil". Pixels with T_{IR} greater than 240 K and less than 280 K are labeled "shallow convection/thick cirrus". Pixels with T_{IR} greater than 280 K and T_{WV} less than 245 K are labeled "thin cirrus". All other pixels are assumed to be either clear sky or only partially covered by cloud and are disregarded in the following analysis. The classification scheme is summarized in Table 4.1. The brightness temperature thresholds have been validated against other multi-spectral cloud retrievals and found to be suitable for discriminating clear-sky pixels from cloudy pixels, as well as classifying mid-level and upper-level cloud types (Roca et al. 2002).

Once the overcast pixels in an image have been identified and classified, a cloud

clustering algorithm is applied whereby adjacent overcast pixels of are grouped into a single cloud. Although a different algorithm is used here, the clustering scheme is identical to that described in Mapes and Houze (1993). Overcast pixels must share a side to be included in the same cloud.

4.2.2 Automated cloud tracking

Once cloud maps have been constructed for a series of consecutive images, an automated cloud tracking algorithm is applied to them based upon overlapping pixels in consecutive images. If a cloud overlaps at least one pixel from a cloud in the subsequent image, the two clouds are assumed to be related. Often, because of splitting, a cloud will overlap several clouds in the subsequent image. Likewise, a cloud often overlaps several clouds from the previous image because of merging. To determine which two clouds are the same cloud from a group of clouds related by overlap in two consecutive images, an "overlap parameter" is calculated for each pair of related clouds which is the product of the fractional area of each cloud that is overlapped. The pair of overlapping clouds with the largest overlap parameter is assumed to be the same cloud. This approach is chosen because it has the effects of identifying the pair of clouds with the maximum area of overlap, as well as the pair with the minimum change in area from one image to the next. Previous studies have tested several different decision algorithms designed to solve this problem and the results were found to be robust regardless of which decision algorithm is applied (Machado et al. 1998; Gambheer 2001).

Fig. 4.1a shows an example of a METEOSAT-5 IR-channel brightness temperature image. The same image, following the pixel classification stage is shown in Fig. 4.1b. The classification scheme is intended to be descriptive only and indicates the rough location of deep convection, mid-level cloud and thin cirrus. Fig. 4.1c shows the same image following the cloud detection stage. The colors in Fig. 4.1c are chosen randomly and each color indicates a different cloud. The scene depicted in Fig. 4.1 is not uncommon during the

18 Jan 1999 1100 GMT
METEOSAT5 IR brightness temperature (K)
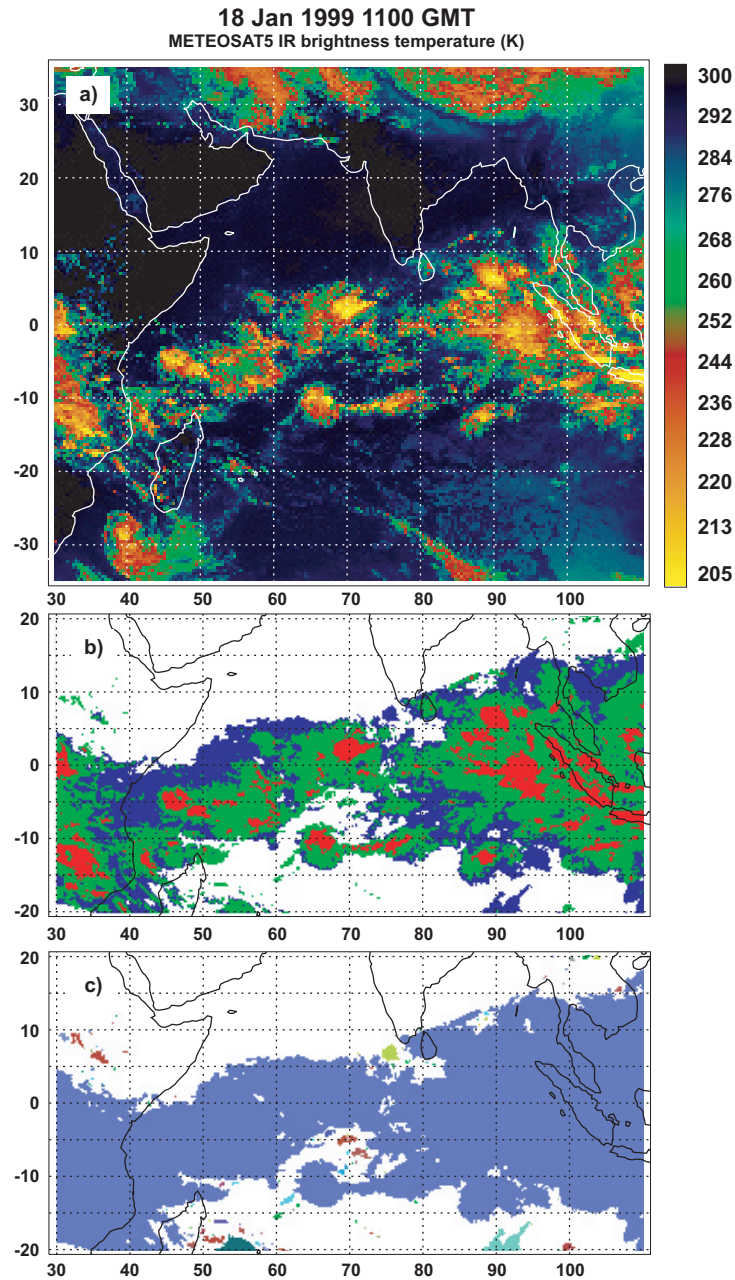
Fig. 4.1. (a) Sample METEOSAT-5 infrared channel brightness temperature image from 18 Jan 1999 1100 GMT. (b) The same image fallowing the pixel classification stage of the analysis. Red pixels are deep convection/anvil; green pixels are shallow convection/thick cirrus; blue pixels are thin cirrus. (c) The same image following the cloud clustering stage of the analysis.

winter monsoon season and shows a giant deck of overcast cloudiness oriented along the

inter-tropical convergence zone with a number of smaller clouds at the periphery of the

convergence zone. According to the analysis scheme employed in this study, the giant

overcast deck is a single cloud and imbedded within this cloud are numerous regions of deep

convection. Throughout this paper, the word "cloud" will be used to refer to the overcast

features illustrated by the different colored features in Fig. 4.1c. The definition of a cloud

illustrated here is not necessarily intended to identify individual dynamical elements. The

details of the cloud detection scheme were chosen to fulfill two goals: 1) to provide an

objective means of identifying cloud boundaries that encompasses deep convective elements

and their attached cirrus decks; and 2) to identify cloud elements in the satellite imagery that

are comparable to cloud elements that may be identified in output from a global GCM.

4.2.3 IR rain rate estimation

Surface rain rate estimates, averaged over the area of each cloud, are made using a

variation of the GOES precipitation index (GPI) technique of Arkin and Meisner (1987).

Rain rate (R_s, with units mm hr^{-1}) is related to f_{240}, the fraction of the area of each cloud with

T_{IR}<240K according to the following expression:

$$R_s = Gf_{240}$$

where the coefficient, G, is calibrated by passive microwave rain rate measurements from

colocated passes of the Tropical Rainfall Measuring Mission (TRMM) satellite (Kummerow

et al. 1998). TRMM Microwave Imager (TMI) brightness temperatures are inverted to

surface rain rates by means of the Goddard Profiling Algorithm (Kummerow et al. 2001).

METEOSAT-5 and TRMM images are colocated in time and space by matching the

METEOSAT-5 image nearest in time to the equator crossing time of each TRMM pass

within the region, and both images are averaged over the same 0.25° $\times$ 0.25° grid. Because

of the high temporal sampling of METEOSAT-5, the colocated images differ in time by no

more than about 15 minutes. The cloud classification and detection algorithm is applied to

the METEOSAT-5 image and the fraction of each clouds' area that lies within the 760 km

TRMM swath is noted. Only clouds with at least 20% of their area within the TRMM swath
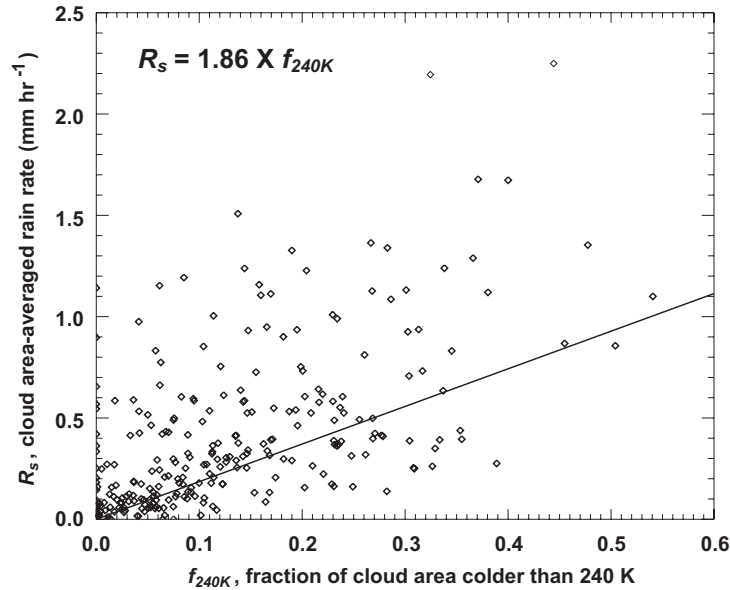
Fig. 4.2. Scatter plot of cloud area-averaged rain rate (R_s) from TRMM and cloud area fraction colder than 240 K (f_{240}) from METEOSAT-5 for a sample of nearly 350 clouds from January, 1999.

are used for calibrating the IR rain estimate. Furthermore, the area of the cloud captured by the TRMM swath must be at least 5×10^4 km². The fraction of each clouds' area that is colder than 240K (f_{240}) and the TRMM rain rate are averaged over the area of the cloud contained within the swath. Nearly 350 clouds fit the above criteria. The relationship between area averaged rain rate and f_{240} for these clouds is shown in Fig. 4.2. The correlation coefficient between R_s and f_{240} is 0.7. *G* is determined by a least squares regression where the contribution of each point in Fig. 4.2 to the regression is weighted by the size of the cloud. *G* has the value 1.86 mm hr^{-1} according to the regression. Weighting the data by cloud size ensures that the domain-averaged value of R_s estimated by METEOSAT-5 will agree reasonably well with that estimated by TRMM since the largest clouds contribute the most to the rainfall in the region. The domain-averaged rain rates (which are discussed in section 4.3) appear in Table 4.2. They are 3.31 mm day^{-1} for TRMM and 3.25 mm day^{-1} for METEOSAT-5. The METEOSAT-5 rain estimates are biased slightly low relative to TRMM because there is a small amount of precipitation observed from clouds that contain

no cloud area colder than 240K. However, only about 2% of total precipitation observed by TRMM occurs in METEOSAT-5 identified clouds with $f_{240} = 0$. Otherwise, the close agreement between the TRMM and METEOSAT-5 estimates reflects the tuning of G by the TRMM data.

Relationships between cold cloud fraction and precipitation, when averaged over sufficient temporal and/or spatial scales tend to be robust in spite of a poor correlation between rain rate and cloud-top temperature at the scale of satellite pixels. A discussion of techniques such as the one described above can be found in Atlas et al. (1990). In general, a greater amount of cold cloud-top coverage corresponds to a higher rain rate. However, a young growing convective cell can have a relatively warm cloud top, but a high rain rate. Alternatively, a decaying anvil cloud can have a cold cloud-top but a low rain rate. The IR rain estimate requires averaging over a sufficiently large area to capture an ensemble of cloud elements at various stages of the convective cloud lifecycle. Alternatively, small regions can be averaged over a sufficient period of time to capture the necessary variability. In this study, the emphasis will be on relatively large cloud systems; systems at least as large as a grid cell in a coarse global model. For these reasons, only clouds larger than 5×10^4 km^2 are used in the calibration of the IR rain rate estimate. Averaging over an area of at least 5×10^4 km^2 captures a sufficient ensemble of cloud elements to establish a reasonable correlation with independent rain rate measurements, and further averaging tends not to improve the correlation (Richards and Arkin 1981).

Note that satellite estimates of surface rain rate are uncertain, in part because of a lack of an unambiguous ground truth. A complete analysis of the TRMM rain estimates appears in Kummerow et al. (2001). They note that one comparison between instantaneous rain rates measured by TRMM and the radar located at the tropical station on Kwajalein suggests the TRMM measurements are biased low by 32%. An independent analysis, however, suggests a positive bias of 17%. Additional random error is introduced into the IR estimate

due to the scatter in the relationship between R_s and G apparent in Fig. 4.2.

In addition to calibrating the IR rain rate estimate, TRMM measurements will be compared with the frequency distribution and domain average of simulated rain rates.

4.2.4 NCAR CCM3 simulation

The analysis of satellite imagery described above results in an ensemble of more than one million clouds spanning several orders of magnitude in spatial coverage and temporal duration. A companion ensemble of simulated clouds is generated for comparison using the National Center for Atmospheric Research Community Climate Model (NCAR CCM version 3.6.6; Kiehl et al. 1996, 1998) run at T42 resolution (approx. 2.5° $\times$ 2.5°). The model is initialized with observations from 1 Sept. 1998 and run through 18 Feb. 1999. The period from 1 Sept. through 31 Dec. is included only to spin-up the model and is not used in the analysis. Observed monthly mean sea surface temperatures are applied. For comparison with the satellite imagery, only the Indian Ocean region (40-110 lon.; 20-20 lat.) is investigated. Overcast decks of cloud are identified in the model output by applying a threshold to the vertically integrated cloud fraction field (assuming random overlap) of 0.99. Clear-sky and partially filled grid cells are not used in the detection and tracking of simulated clouds. The temporal and spatial scales of simulated clouds are relatively insensitive to the choice of cloud fraction threshold. Values between 80% and 99% were tested with little difference in the resulting statistics. Simulated cloud cover associated with the inter-tropical convergence zone during the winter monsoon is characterized by a strong gradient between grid cells with very high cloud fraction and adjacent grid cells of low cloud fraction.

In CCM3, the processes leading to the formation of cloud and precipitation arise from separate parameterizations. Layer clouds are formed using relationships based on relative humidity that are similar to those developed by Slingo (1987). Convective cloud cover is computed using a relationship based primarily on convective mass flux. In the tropical Indian Ocean region, the layer cloud parameterization provides most of the cloud cover,

while the convective cloud amounts to a steady contribution of 10% low-level coverage in nearly all grid cells. The poor physical connection between convection, convective cloud cover, and anvil/cirrus layer cloud in the model is discussed by Rasch and Kristjánsson (1998). The spatial and temporal scales of CCM3 simulated tropical cloudiness are thus determined primarily by the resolved-scale distribution and transport of water vapor.

In contrast, simulated precipitation in the tropical Indian Ocean region depends entirely on physics assumed to be occurring at subgrid-scales. Virtually all of the precipitation produced by the model in this region is generated within the deep convection parameterization scheme. According to the scheme, mass fluxes of a subgrid-scale ensemble of convective updrafts and downdrafts is predicted based on the quantity of convective available potential energy determined from grid cell values of temperature and humidity. Precipitation is produced at a rate that is proportional to the mass flux of the updrafts and a fraction of that precipitation is evaporated in the downdrafts. Details of the scheme are described in Zhang and McFarlane (1995). In winter monsoon cloud systems, approximately 97% of total precipitation results from deep convection. Another 2% of total precipitation is generated by a separate parameterization of shallow convection (Hack 1994). The remainder is contributed through the process of stable condensation, whereby an entire grid cell reaches super-saturation and the excess moisture is removed as precipitation.

4.3 Domain-averaged precipitation and cloud cover

A comparison of the precipitation amount and cloud cover averaged over the entire observation region and time period is presented in Table 4.2. The domain averaged rain rate as observed by TRMM during the period is 3.31 mm day^{-1}. Using the infrared cloud-top temperature proxy for rain (calibrated by TRMM) the average rain rate is 3.25 mm day^{-1}. The model simulated rain rate during the same period is 5.31 mm day^{-1}; or about 60% greater than observed. The amount of precipitation that occurs in grid cells that are partially filled with cloud is about 19% of the total model simulated precipitation in the domain. By colocating

Table 4.2. Comparison of mean precipitation and cloud properties.

	TRMM observations	METEOSAT-5 observations	CCM3 simulation
rain rate (mm day^{-1})	3.31	3.25	5.31
fraction of precipitation from partly cloudy grid cells (%)		32[*]	19
cloud cover (%)		45	66
overcast grid cell cover (%)		27	52
partially filled grid cell cover (%)		18	14

[*] from colocated METEOSAT-5 cloud mask and TRMM TMI rain rates.

the METEOSAT-5 cloud mask and TRMM surface rain rate observations and averaging over

the CCM3 grid, it is determined that 32% of observed precipitation occurs in partially filled

grid cells. When observed rain rates are averaged over cloud area and arranged by cloud size,

however, it is revealed that only about 2% of total precipitation results from clouds that are

smaller than a single T42 model grid cell (not shown). This result suggests that it is common

for the boundaries of intermediate-scale clouds and giant semi-permanent clouds to fall in

the middle of a grid cell, and for that portion of the cloud to contain some precipitation.

This result implies there is a limitation in the application of the cloud detection scheme

to coarse-grid model output since all partially cloud covered grid cells are assumed to be

composed of isolated clouds that are smaller than a grid cell, when in fact they include cloud

cover that is attached to multi-grid cell overcast decks. Hence the spatial scales reported for

CCM3 clouds are probably somewhat underestimated.

Cloud cover is substantially larger in the model simulation than in the observations.

Model simulated cloud fraction is 66%. 52% is attributable to the overcast cloud decks

tracked in this study, while 14% is contributed from partially filled grid cells. Observed cloud

fraction is 45%, suggesting that model overestimates cloud cover by 20%. Resampling the

METEOSAT-5 images at the resolution of the model grid, indicates that the cloud cover

associated with partially filled grid cells is 18%, which is in relatively close agreement with the

model simulation. This suggests that the largest problems in simulating spatial coverage of cloud are associated with the overcast decks.

4.4 Spatial and temporal properties of cloud cover

The satellite image analysis indicates that a few, very large, semi-permanent overcast decks dominate winter monsoon cloud coverage over the Tropical Indian Ocean. Fig. 4.3a (solid line) shows the number distribution of observed clouds as a function of cloud lifetime. While over one million individual clouds were detected and tracked, only five clouds where found to last for greater than 100 hours. They are, however, the five largest clouds observed; each exceeding one million square-km in mean area, as illustrated in Fig. 4.3b (solid line). Mean area is defined as the area of the cloud averaged over each of the time steps through which the cloud was tracked. The cumulative contribution to the total observed cloud cover is presented in Fig. 4.3c and demonstrates that over 80% of the cloud coverage is attributable to just these five long lived clouds. Note that the lifetime of clouds is a somewhat arbitrary quantity because the birth and death of clouds, even at moderate scales, is predominantly determined by the merging and splitting of existing clouds rather than the spontaneous generation and dissipation of independent clouds. Nevertheless, the relationship between size and lifetime (Fig. 4.3b) indicates that, on average, the longevity and spatial coverage of clouds are positively correlated. A similar feature was observed for the convective clouds over the Pacific Ocean (Boer and Ramanathan 1997). Clouds reaching scales of tens of millions of square kilometers exist because the spreading of middle- and upper-level cloudiness from localized regions of intense deep convection is sufficient to bridge the gaps between them. Such decks of cloud are able to persist for periods of weeks because of the residence time of anvil and cirrus cloud material is long enough to maintain the bridges between convective centers over the faster time-scale variability of deep convection.

The time scales associated with the interactions between convection and extended decks of anvil and cirrus cloud are indicated in time series of cloud area for specific clouds.
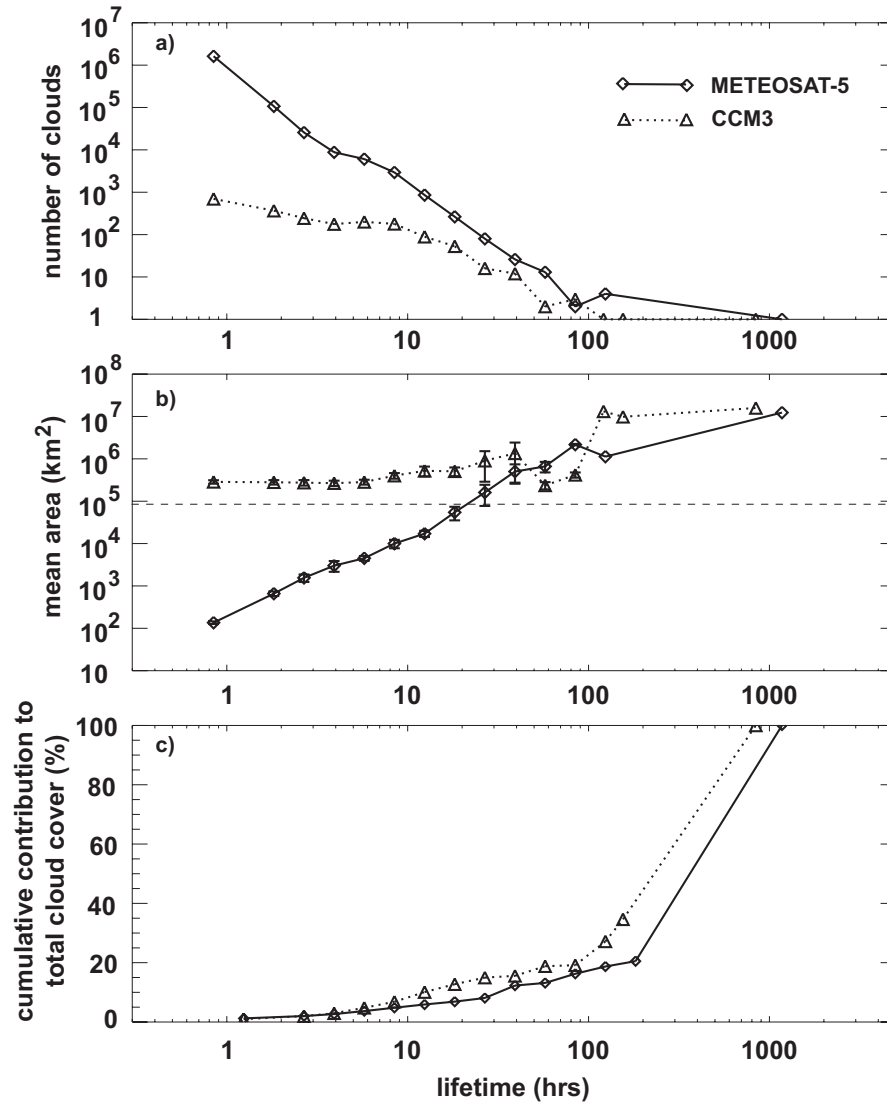
Fig. 4.3. (a) Number distribution of clouds. (b) Cloud area averaged over the lifetime of each cloud. (c) Cumulative contribution to total cloud area. All are shown as a function of cloud lifetime. Solid lines are observed clouds. Dotted lines are simulated clouds. Horizontal dashed line in (b) indicates approximate size of a single model grid cell. Error bars indicate one standard deviation of the mean cloud area in each size bin.

An example of the evolution of cloud area for a single tracked cloud appears in Fig. 4.4a.

Figure 4.4b shows the area of the cloud that is attributable to each classification (the sum

of each of the three lines in Fig. 4.4b is the curve shown in Fig. 4.4a). Deep convection

and anvil cloudiness within this cloud tend to peak in the afternoon as illustrated by the

area colder than 240K (solid line). The area covered by thin cirrus (dash-dot line) peaks
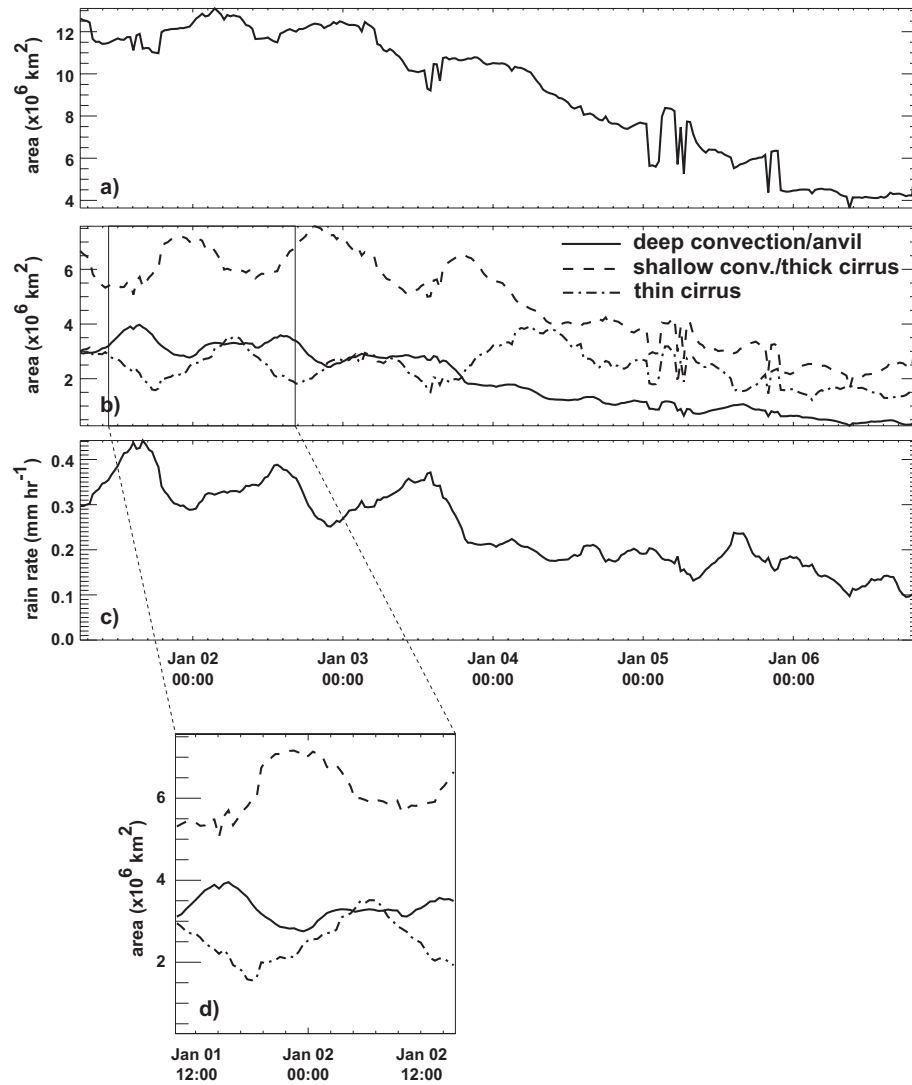
Fig. 4.4. (a) Evolution of cloud area for a single cloud observed over a 7 day period. (b) Evolution of spatial coverage of each cloud type within the cloud. Solid line is deep convection/anvil cloud; dashed line is shallow convective/thick cirrus cloud; dash-dot line is thin cirrus. (c) Evolution of rain rate averaged over the entire area of the cloud. (d) Same as (b) for 24 hour period. Time on axis indicates local time at the geographic center of the cloud.

12-15 hours later and the intermediate cloud class (dashed line) peaks in between. While convection varies strongly on a diurnal time scale, the lag between the peak in convection and the peak in cirrus cloud cover helps explain how giant overcast decks persist.

Although cloud cover associated with overcast decks is over-predicted, the comparison of modeled and observed temporal cloud statistics shown in Fig. 4.3 indicates good

agreement (all results for model simulated clouds are shown with dotted lines). Differences in the number distribution and mean area of clouds at time scales of 1 hour to 1 day result from the difference in resolution between the model grid and the satellite imagery. The horizontal dashed line in Fig. 4.3b indicates the approximate size of a single model grid cell. There cannot be any overcast decks in the model that are smaller than a grid cell. Because of the finer resolution of the satellite, there are overcast decks identified in the imagery that are smaller than the model grid cell. In fact, there are a large number of these observed subgrid-scale clouds, which tend to have lifetimes shorter than a day. These clouds, if present in the model, are excluded from the cloud detection and tracking analysis. Hence the appearance of a larger number of short-lived subgrid-scale clouds in the observations is an artifact of the analysis scheme. When the data are expressed as the cumulative contribution to total cloud cover (Fig. 4.3c), the dominance of the giant, semi-permanent overcast decks is apparent in both the satellite imagery and the model simulation.

That the model is capable of reproducing the presence of the semi-permanent decks is noteworthy because the model does not impose any time scales on the cloud cover. In the standard configuration, the model completely erases and recalculates the cloud field once each model hour. Since relative humidity is the sole predictor of the upper-level clouds that make up the semi-permanent cloud decks, this result implies that the time scales associated with the large-scale distribution of humidity and the moisture transport are appropriate for maintaining the cloud decks.

As mentioned above, however, cloud fraction associated with the semi-permanent decks is too large, which is attributable to an improper representation of the spatial scales of these cloud systems. Fig. 4.5a shows the number distribution of clouds as a function of cloud size for observed and simulated clouds. The observations indicate that there are many orders of magnitude more clouds at the scale of a satellite pixel than there are at the scales of 10^6 to 10^7 km^2. The distribution of model simulated clouds indicates that there are too
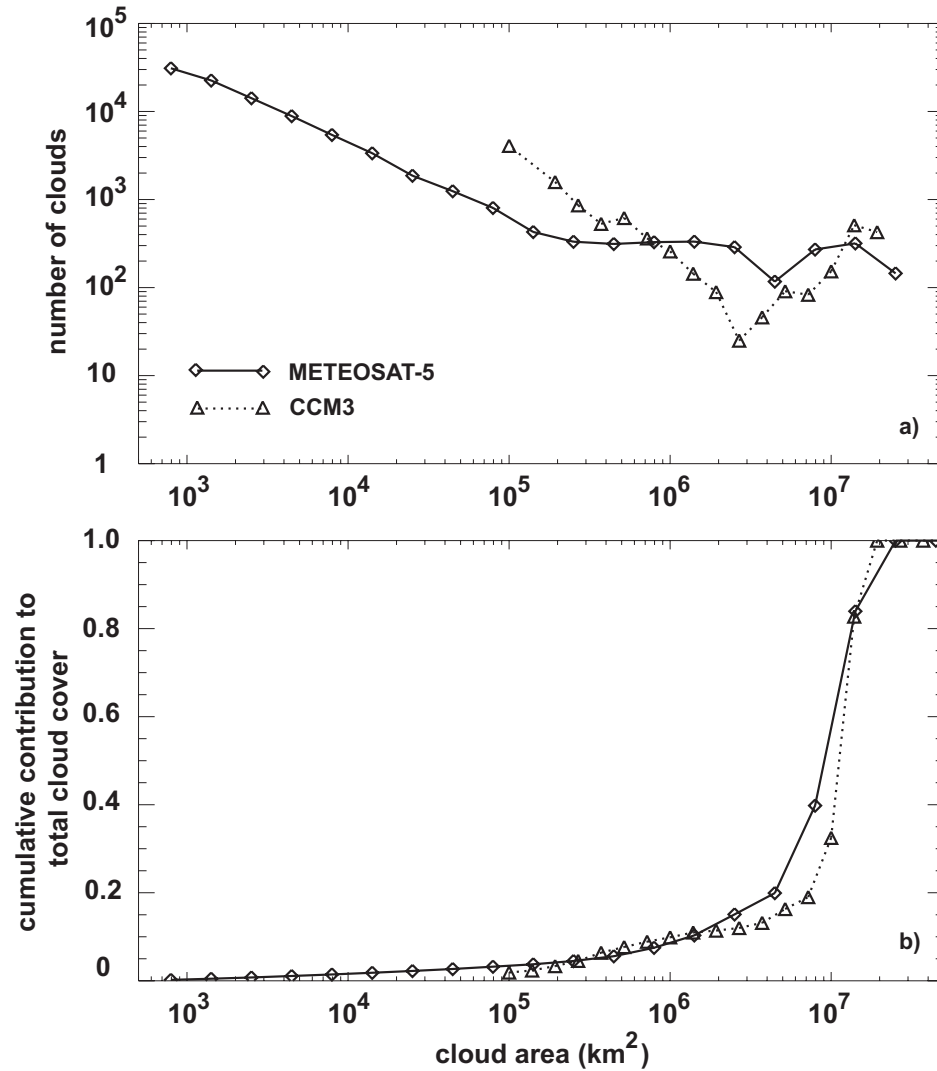
Fig. 4.5. (a) Number distribution of clouds. (b) Cumulative contribution to total cloud area. All are shown as a function of cloud area. Solid lines are observed clouds. Dotted lines are simulated clouds.

many clouds at the intermediate scales of one to a few grid cells, too few clouds between 10^6 and 10^7 km^2 and too many clouds at scales of the largest overcast decks. The consequence of this bias in the size distribution of clouds is evident in Fig. 4.5b, which shows the cumulative contribution to total cloud cover as a function of cloud size. The dominant scale of clouds, those that contribute to most of the total cloud cover, is several million square-km larger in the model. This result implies that either the upper-tropospheric humidity is distributed

too broadly over the region during too much of the period, or the diagnostic relationship between relative humidity and cloud fraction is biased toward too much cloud for winter monsoon anvil and cirrus cloud.

4.5 Observed and simulated precipitation properties

Across the observed scales of clouds, precipitation rate increases with cloud size. In contrast, simulated clouds exhibit a nearly binary behavior with respect to precipitation (Fig. 4.6a). Simulated clouds smaller than 2×10^6 km^2 have cloud area-averaged rain rates of about 0.15 mm hr^{-1}, while clouds larger than 2×10^6 km^2 have rain rates of about 0.35 mm hr^{-1}. Because of the large space and time scales of the largest clouds, they dominate the contribution to the domain-averaged precipitation. The over-prediction of rain rate within clouds at the largest scales, is responsible for the over-prediction of precipitation over the entire domain and time period. Note that the solid curve in Fig. 4.6a is based on the IR rain estimation approach discussed in section 4.2.3, and therefore includes the considerable scatter shown in Fig. 4.2. However Fig. 4.6a is the same statistic for 1999 METEOSAT-5 data as computed directly with TRMM rain rate measurements for 1998 data shown in Fig. 3.5a. The two curves indicate the same increasing trend in rain rate with increasing cloud area, although the 1999 METEOSAT-5 data (Fig. 4.6a, solid line) indicate a slightly lower rain rate than the 1998 TRMM data (Fig. 3.5a, solid line) at most cloud size bins.

Although the intermediate-scale clouds (5×10^4 km^2 to 5×10^5 km^2) have average rain rates in better agreement with observed rain rates, the fraction of clouds at this scale that are precipitating is slightly overestimated, as indicated by Fig. 4.6b. Here the probability that a cloud contains a region of precipitation within its boundaries is presented as a function of cloud size. The giant, semi-permanent cloud decks always contain active deep convection, and are therefore always precipitating. The smallest observed clouds (less than 1×10^5 km^2) almost never precipitate. A fraction ranging between 0.4 and 1 of the intermediate-scale clouds are precipitating clouds. This includes a fraction of clouds that never precipitate as
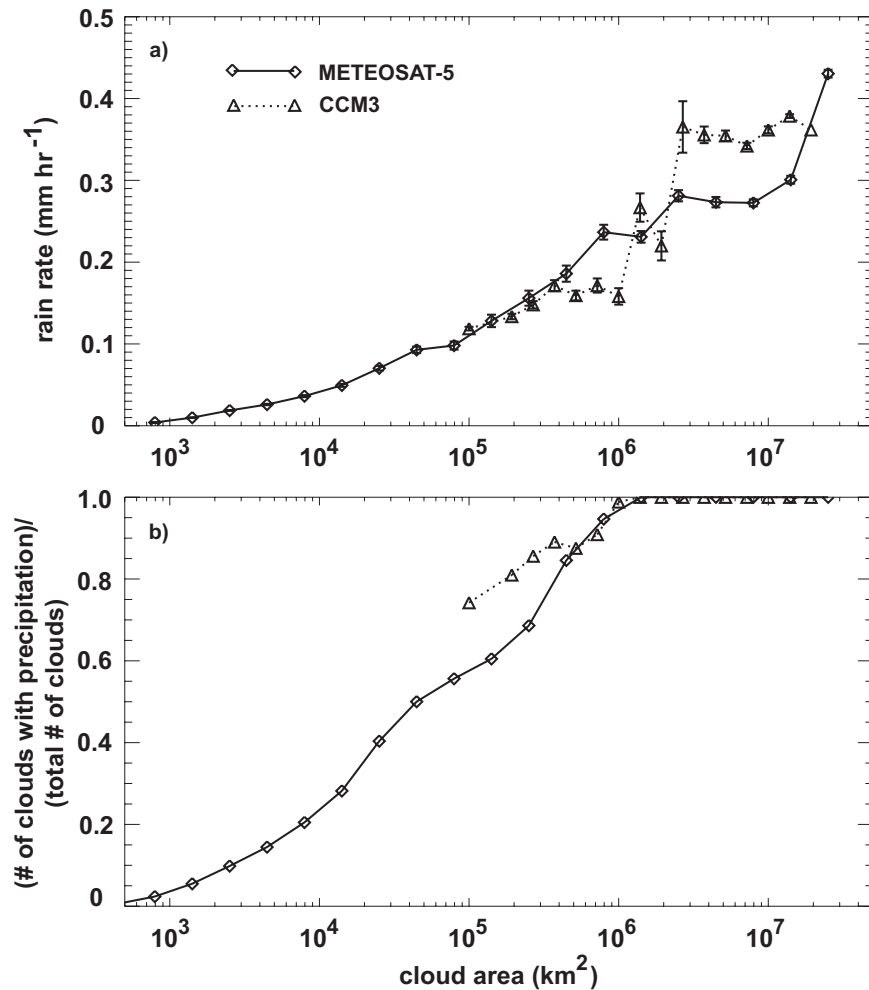
Fig. 4.6. (a) Rain rate averaged over the entire area of cloud. (b) Fraction of clouds in each size bin that contain some precipitation. All are shown as a function of cloud area. Solid lines are observed clouds. Dotted lines are simulated clouds. Error bars indicate one standard deviation of the mean rain rate in each size bin.

well as a fraction of clouds that precipitate for only a portion of their total lifetime.

While precipitation averaged over the horizontal scales of giant cloud decks is larger than observed, rain rates on the scale of individual grid cells is biased low relative to observations. This is confirmed by directly comparing the frequency distribution of simulated grid cell rain rates to measured rain rates averaged over the same CCM3 model grid. Because rain rates estimated by infrared brightness temperatures are less accurate than passive microwave measurements, only TRMM measurements are used here. All TRMM passes over the Indian

1 Jan - 18 Feb. 1999 (20S-20N; 40E-110E)
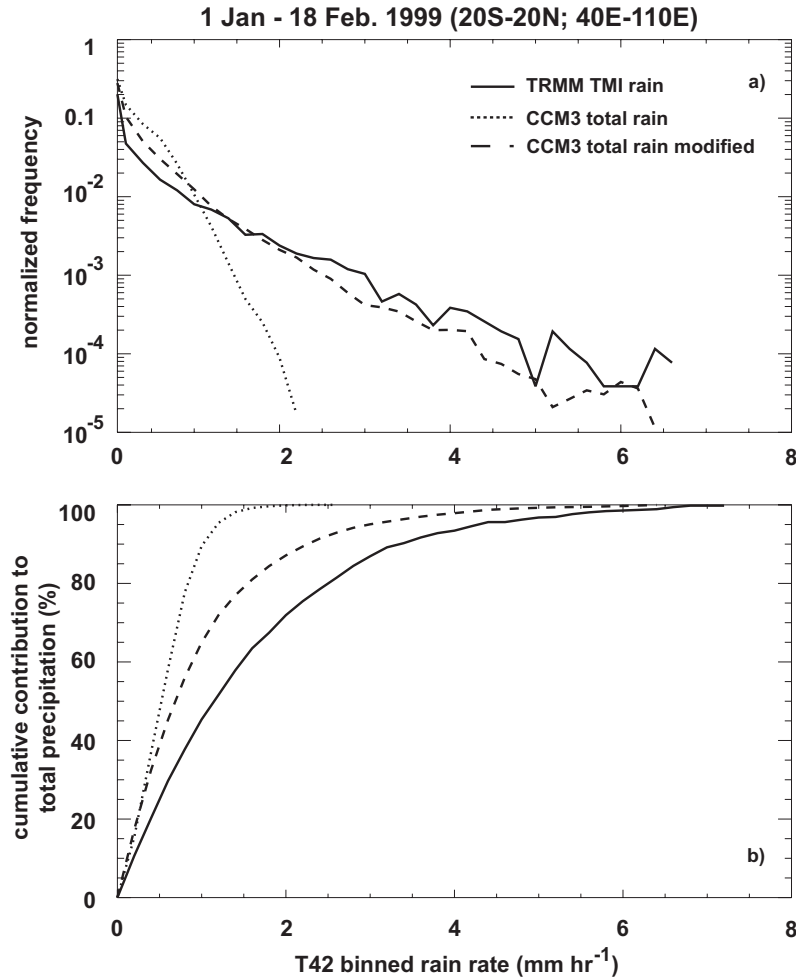
Fig. 4.7. (a) Frequency distribution of rain rate. (b) Cumulative contribution to total precipitation. Solid lines are observations from the TRMM Microwave Imager. Dotted lines are simulated rain rates from CCM3. Dashed lines are simulated rain rates from CCM3 with the mesoscale evaporation modification added to the model. All rain rates are averaged over CCM3 grid boxes at T42 resolution.

Ocean region during the 49 day period are used and the pixel data are averaged over the CCM3 grid cells at T42 resolution. The result is shown in Fig. 4.7 (solid and dotted lines). Virtually all of the simulated precipitation occurs at instantaneous rain rates lower than 2 mm hr^{-1}, while as much as 25% of the observed precipitation occurs at rain rates higher than 2 mm hr^{-1}. Furthermore, greater than 99% of the simulated precipitation is diagnosed by the convective parameterization scheme and hence is assumed to result entirely from convective updrafts at scales much smaller than a single grid cell. This means that less than 1% of the

precipitation occurs by the stable condensation process, whereby an entire grid cell reaches super-saturation and the excess moisture is removed as precipitation. However, application of the cloud clustering algorithm directly to the surface rain rate images from TRMM indicates that 60% of observed precipitation in the region occurs in contiguous regions of precipitation that are larger than a single T42 model grid cell (not shown). The horizontal scale of rain areas and the horizontal scale of a resolved dynamical feature necessary to produce a supersaturated grid cell are probably not comparable. Nevertheless, the observations reveal that a significant portion of precipitation in the winter monsoon environment results from mesoscale organized convective structures spanning areas larger than a model grid cell. Such structures are not parameterized in the model, yet the model resolution is not sufficient for motions at these scales to emerge. These mesoscale convective systems are responsible for the extreme, episodic precipitation events at the tail of the TRMM rain distribution in Fig. 4.7. Such systems are typically embedded within larger cloud decks with as much as 75% of the cloud deck consisting of non-precipitating cloud (Wilcox and Ramanathan 2001). In contrast, the simulated clouds gently precipitate everywhere and all of the time.

The smoothing of precipitation in time and space in the model has obvious implications for the prediction of extreme precipitation events. The effects on simulations of the atmospheric circulation and hydrological cycle in regions of deep convection require further study. The poor representation of the time and space scales of precipitation may also have important implications for the evolution of soluble trace gas and aerosol constituents. The transports of such constituents are now commonly added to global general circulation models in order to assess their climate impacts. The distribution of such constituents is often quite heterogeneous. Subjecting them to a scavenging loss mechanism that is improperly represented in time and space could potentially lead to large errors in predictions of their concentrations.

4.6 Sensitivity of simulated rain rate distribution to moisture recycling

The CCM3 convection parameterization responds to a build-up of convective available potential energy in a grid column by generating an ensemble of convective cells in the column to release the potential energy, and in many cases also generating some precipitation. The broad distribution of gentle precipitation in CCM3 is a consequence of a tendency within the convective parameterization scheme to release such potential energy too frequently. Similarly, the complete dominance of convective precipitation over stable condensation results from the too frequent invocation of the convection scheme. A reformulation of the convective parameterization is beyond the scope of this paper. However, a simple modification to the parameterization of convective precipitation in the model is tested here that simulates the effect of the evaporation of convectively generated precipitating condensate in mesoscale downdrafts. The modification has a significant impact on the frequency distribution of rain rate.

In the standard formulation of CCM3, convective precipitation is diagnosed from the magnitude of convective mass flux (Zhang and McFarlane 1995). Under the assumption that all of evaporation of precipitation occurs within narrow saturated downdrafts, a portion of the diagnosed precipitation is allowed to re-evaporate. In the case of tropical convection, however, as much as 16% of the total precipitation in a mesoscale cloud cluster may be evaporated in unsaturated mesoscale downdrafts (Gamache and Houze 1983). As mentioned previously, the physics of these mesoscale organized convective structures are absent from the present formulation of convection in CCM3. In this section, a simple modification is made to CCM3 that allows a fraction of the convective precipitation to re-evaporate within the environment surrounding the convective updrafts and downdrafts. This modification is not intended to be a complete parameterization of organized tropical convection, as it does not include many important features, such as the mass and momentum fluxes within mesoscale updrafts and downdrafts. The modification does, however, illustrate the potential

importance of environmental moistening by such structures in modulating the spatial and temporal scales of precipitation.

Parameterized mesoscale re-evaporation is limited only to precipitation generated through the parameterization of deep convection. Following the formulation of the re-evaporation of stable condensation, which is already present in the model, deep convective precipitation is made available for evaporation in each lower layer where relative humidity is less than 1. Unlike stable condensation, however, evaporation of deep convective precipitation is further constrained by the cloud field. In addition to being sub-saturated, grid cells must have a cloud fraction less than 0.5 for deep convective precipitation to evaporate. The cloud fraction constraint is chosen arbitrarily, however is designed to be consistent with the observation that mesoscale evaporation occurs in clear areas beneath precipitating anvils. Like the evaporation of stable condensation, the rate of evaporation of deep convective precipitation is calculated using the relation proposed by Sundqvist (1988):

$$E = k_E (1 - RH)\, R^{1/2}.$$

E is the rate of the evaporation, RH is relative humidity and R is the rate of production of precipitation. E has the units of kg kg^{-1} s^{-1} and R has units of kg m^{-2} s^{-1}. The constant, k_E, has the value 10^{-5}. For grid columns in the Indian Ocean region with rain rates greater than 1 mm hr^{-1} this formulation results in a vertically integrated evaporation rate that is on average about 10% of the surface rain rate, which is in reasonable agreement with the observational study of Gamache and Houze (1983).

Domain-averaged rain rate remains nearly constant (5.39 mm day^{-1} compared to 5.31 mm day^{-1}) in spite of the increased evaporation, indicating that the overall quantity of moisture precipitated in the Indian Ocean monsoon trough is somewhat insensitive to the details of precipitation microphysics. The distribution of precipitation, however, changes significantly. The addition of parameterized mesoscale evaporation shifts the distribution of

winter monsoon precipitation toward higher rain rates than in the standard CCM3 simulation (Fig. 4.7, dashed lines). While almost no simulated precipitation occurs at rates higher than 2 mm hr^{-1} in the standard model, nearly 20% of the total precipitation occurs in grid cells with rain rates greater than 2 mm hr^{-1} in the modified model. The addition of moisture recycling also results in a modest increase in the percentage of precipitation resulting from stable condensation; rising from 1% in the standard simulation to 3% in the modified simulation. As discussed previously, observations of the horizontal scales of surface rain rate features suggest that the stable condensation fraction should be higher than in the standard model, however the proper value of this partitioning is not well constrained by observations. Better observations of the vertical profile of precipitating condensate would help in this regard. Furthermore, the value of this partitioning should be closely tied to the convective parameterization, which in turn should be properly tuned to the resolution of the model, since the amount of stable condensation will reflect the amount of resolved-scale convection is assumed to be present.

The modification to the model tested here is intended to determine if a simple modification to the model could significantly change the distribution of precipitation. While successful in generating extreme precipitation rates more similar to the observations, the modification is not intended to account for the mass, momentum and energy fluxes associated with organized mesoscale convection. A discussion of the effects of a more complete parameterization of mesoscale dynamics on many aspects of a GCM integration can be found in Donner et al. (2001).

4.7 Summary

A Lagrangian analysis scheme is explored as a tool for testing the spatial, temporal and precipitation characteristics of winter monsoon clouds over the tropical Indian Ocean as simulated by the NCAR CCM3 global general circulation model. Overcast decks of cloud of the scale of a single model grid cell and larger are detected and tracked over a 49

day period during January and February, 1999 and compared with clouds observed by the METEOSAT-5 geosynchronous satellite. Statistics for simulated and observed clouds are arranged by size and lifetime in order to determine if the frequency distribution of clouds as a function of size and lifetime are properly simulated. Furthermore, the dependence of rain rate and rain frequency upon cloud size is compared, where infrared rainfall estimates are supplemented with colocated observations from the TRMM satellite. Such Lagrangian statistics supplement more traditional Eulerian techniques of comparing time- and space-averaged, gridded fields of cloud cover and precipitation in determining where model parameterizations fall short of simulating complex deep convective cloud systems.

Clouds, defined as overcast decks, are observed spanning spatial scales from 25 km^2 to greater than 10^7 km^2, as well as temporal scales from 1 hour to greater than 100 hours. Semi-permanent decks of anvil and cirrus cloud, with numerous regions of deep convection embedded within, dominate total cloud cover. The peak in total spatial coverage of such cloud systems lags the peak in coverage by deep convective cloudiness by 12-15 hours because of the residence time of cirrus cloud material and the time it takes the material to spread from the regions of convection. As a result, semi-permanent cloud decks can persist for time scales of days to weeks. It is potentially advantageous for global models with coarse grids that overcast decks as large or larger than several model grid cells dominate deep convective cloud cover. From a validation standpoint, this fact means there are identifiable cloud features (*i.e.*, resolved overcast decks) that can be directly compared to similar observable features. Semi-permanent decks are simulated in CCM3 in spite of the fact that the diagnostic scheme for predicting cloud cover makes no assumptions about the time scales of cloud material. Nevertheless, several significant differences are apparent between the observed and simulated cloud systems.

At scales greater than 10^6 km^2 the size distribution of simulated clouds is biased such that the dominant scale of clouds is several million km-square larger than the dominant

scale of observed clouds. Averaged over the entire domain, cloud cover attributable to the giant overcast decks is over-predicted by greater than 20%. In order to maintain cloud decks of this scale, precipitating deep convection is always occurring somewhere within the boundaries of the cloud. These cloud systems also contribute most of the precipitation in the region. Within the simulated semi-permanent decks, precipitation rates averaged over cloud area are substantially higher than observed. As a result, the domain-averaged precipitation rate is larger in the model simulation than is observed by the TRMM satellite. Although precipitation is over-predicted in the model, the frequency distribution of rain rates is biased low in the model relative to TRMM data averaged over the model grid. The semi-permanent cloud decks simulated in the model gently precipitate throughout their duration and everywhere within their boundaries. This contrasts with observed semi-permanent cloud systems, which precipitate throughout their duration, but do so in more localized regions of precipitation. Most of the observed precipitation occurs in mesoscale precipitation features with high precipitation rates that are absent from the model. All of the simulated precipitation occurs in convective updrafts assumed to be small relative to a model grid cell. What the model lacks is a process that acts to organize the convective cells within fewer grid cells, in addition to a representation of the observed stratiform precipitation structures. Furthermore, while most grid cells within the semi-permanent clouds are precipitating, very few reach grid cell supersaturation and precipitate by stable condensation. The scales of saturated regions cannot be observed, however the TRMM imagery indicates that as much as 60% of precipitation results from precipitation regions that are larger than a single grid cell. This implies that a greater fraction of simulated precipitation should arise from stable condensation, although more detailed observations are required to properly constrain this parameter.

On average, intermediate-scale clouds (clouds of the size of one to a few grid cells) have precipitation rates that are similar to observed clouds of comparable scale. However,

the probability that a cloud at this scale contains some precipitation is slightly overestimated in the model. Cloud cover associated with partially filled grid cells in the model agrees reasonably well with observed clouds averaged over the model grid. Evidence suggests that a significant portion of the partially filled grid cells are in fact attached to overcast decks that are larger than a grid cell. 19% of simulated precipitation and 32% of observed precipitation occurs in model grid cells that are only partially filled with cloud. Clouds that are physically smaller than a model grid cell are plentiful in the observations, however, they account for a small portion of the total cloud cover and only 2% of total observed precipitation.

As the application of general circulation models expands to the simulation and prediction of precipitation variability of societal importance, such as the frequency of extreme precipitation events, the biases in the distribution of rain rates documented here will become an increasingly serious issue. Even in cases where analyses of simulated monthly mean precipitation fields indicate quantitative and spatial agreement with observations, the intense precipitation events associated with organized mesoscale structures are missing. Likewise, the use of global GCMs to drive the advection and scavenging of aerosols will require that the spatial and temporal scales of precipitation be adequately represented. The application of the Lagrangian analysis scheme employed in this study to satellite imagery of clouds and precipitation can help constrain assumptions within aerosol scavenging parameterizations about the spatial scales of precipitation. Future development of convection parameterizations that include the organization of deep convection and associated mesoscale circulations should motivate the extreme precipitation events found to be absent in the present version of CCM3. Included in this study is the test of a modification to CCM3 intended to account for the evaporation of upper-level precipitation in mid-level mesoscale downdrafts. The modification results in only a slight change in domain-averaged precipitation, indicating that the regional-scale hydrological balance is not sensitive to this aspect of convection. However, the modification causes a significant shift in the distribution

of precipitation toward higher rain rates, as well as a modest increase in the fraction of precipitation resulting from stable condensation. The modification demonstrates the sensitivity of the model to one important component of mesoscale organized convection.

An advantage of the Lagrangian analysis scheme is that it evaluates clouds and precipitation in the context of integrated cloud systems. Convection, clouds and microphysics are parameterized separately in GCMs. In nature, however, close coupling between each of these processes gives rise to the cloud systems observed in satellite imagery. Not every applicable quantity is observable, however the Lagrangian scheme provides a means of evaluating how well the links between each of the parameterized processes results in cloud systems that mimic natural cloud systems. This study has explored some of the relationships between precipitation and cloud cover. The analysis demonstrates that there is a mismatch between the distribution of precipitation and the distribution of cloud cover: most seriously within the giant semi-permanent decks. In spite of the fact that convective-scale and mesoscale updrafts provide the condensate for both the precipitation and the extended decks of cloud, the relative humidity-based cloud cover parameterization is physically decoupled from convection in the model. The resulting cloud cover associated with the semi-permanent decks is higher than observed and precipitation is not properly distributed in time and space within the clouds.

References

Arkin, P. A. and B. N. Meisner, 1987: The relationship between large-scale convective rainfall and cold cloud over the western hemisphere during 1982-84. *Mon. Wea. Rev.*, **115**, 51-74.

Atlas, D., D. Rosenfeld, and D. A. Short, 1990: The estimation of convective rainfall by area integrals 1. The theoretical and empirical basis. *J. Geophys. Res.*, **95**, 2153-2160.

Balkanski, Y. J., D. J. Jacob, G. M. Gardner, W. C. Graustein, and K. K. Turekian, 1993: Transport and residence times of tropospheric aerosols inferred from global three-dimensional simulation of ^{210}Pb. *J. Geophys. Res.*, **98**, 20 573-20 586.

Boer, E. R. and V. Ramanathan, 1997: Lagrangian approach for deriving cloud characteristics from satellite observations and its implications to cloud parameterization. *J. Geophys. Res.,* **102**, 21 383-21 399.

Donner, L. J., C. J. Seman, R. S. Hemler, and S. Fan, 2001: A cumulus parameterization including mass fluxes, convective vertical velocities, and mesoscale effects: thermodynamic and hydrological aspects in a general circulation model. *J. Climate*, **14**, 3444-3463.

Gamache, J. F. and R. A. Houze Jr., 1983: Water budget of a mesoscale convective system in the tropics. *J. Atmos. Sci.*, **40**, 1835-1850.

Gambheer, A. V. and G. S. Bhat, 2000: Life cycle characteristics of deep cloud systems over the Indian region using *INSAT-1B* pixel data. *Mon. Wea. Rev.*, **128**, 4071-4083.

Hack, J. J., 1994: Parameterization of moist convection in the National Center for Atmospheric Research Community Climate Model (CCM2). *J. Geophys. Res.*, **99**, 5551-5568.

Houghton, J. T., Y. Ding, D. J. Griggs, M. Noguer, P. J. van der Linden, and D. Xiaosu, Eds., 2001: *Climate Change 2001: The Scientific Basis: Contribution of Working Group 1 to the Third Assessment Report of the Intergovernmental Panel on Climate Change.* Cambridge University Press, 944 pp.

Houze, R. A. and A. K. Betts, 1981: Convection in GATE. *Rev. Geophys. Space Phys.,* **19**, 541-576.

Kiehl, J. T., J. J. Hack, G. B. Bonan, B. A. Boville, D. L. Williamson, and P. J. Rasch, 1998: The National Center for Atmospheric Research Community Climate Model: CCM3. *J. Climate*, **11**, 1131-1149.

Kiehl, J. T., J. J. Hack, G. B. Bonan, B. A. Boville, B. P. Briegleb, D. L. Williamson, and P. J. Rasch, 1996: Description of the NCAR Community Climate Model (CCM3). NCAR Tech. Note, NCAR/TN-420+STR, 151 pp. [Available from National Center for Atmospheric Research, Boulder, CO 80307; http://www.cgd.ucar.edu/cms/ccm3/TN-420/].

Kummerow, C., W. Barnes, T. Kozu, J. Shiue and J. Simpson, 1998: The Tropical Rainfall Measuring Mission (TRMM) sensor package. *J. Atmos. Ocean Technol.,* **15**, 809-817.

Kummerow, C, Y. Hong, W. S. Olson, S. Yang, R. F. Adler, J. McCullum, R. Ferraro, G. Petty, D. -B. Shin and T. T. Wilheit, 2001: The evolution of the Goddard Profiling Algorithm (GPROF) for rainfall estimation from passive microwave sensors. *J. Appl. Meteor.*, **40**, 1801-1820.

Machado, L. A. T., W. B. Rossow, R. L. Guedes, and A. W. Walker, 1998: Life cycle variations

of mesoscale convective systems over the Americas. *Mon. Wea. Rev.*, **126**, 1630-1654.

Mapes, B. E. and R. A. Houze, 1993: Cloud clusters and superclusters over the oceanic warm pool. *Mon. Wea. Rev.,* **121**, 1398-1415.

Rasch, P. J. and J. E. Kristjánsson, 1998: A comparison of the CCM3 model climate using diagnosed and predicted condensate parameterizations. *J. Climate*, **11**, 1587-1614.

Rasch, P. J, W. D. Collins, and B. E. Eaton, 2001: Understanding the Indian Ocean Experiment (INDOEX) aerosol distributions with an aerosol assimilation. *J. Geophys. Res.*, **106**, 7337-7355.

Richards, F. and P. Arkin, 1981: On the relationship between satellite-observed cloud cover and precipitation. *Mon. Wea. Rev.*, **109**, 1081-1093.

Roca, R., M. Viollier, L. Picon, and M. Desbois, 2002: A multi satellite analysis of deep convection and its moist environment over the Indian Ocean during the winter monsoon. *J. Geophys. Res.* special INDOEX issue, part 2, in press.

Slingo, J. M. 1987: The development and verification of a cloud prediction scheme for the ECMWF model. *Quart. J. Roy. Meteor. Soc.,* **113**, 899-927.

Sundqvist, H. R., 1988: Parameterization of condensation and associated clouds in models for weather prediction and general circulation simulation, in *Physically-Based Modelling and Simulation of Climate and Climatic Change* (M. E. Schlesinger, Ed.), Kluwer Academic Press, 624 pp.

Wilcox, E. M. and V. Ramanathan, 2001: Scale dependence of the thermodynamic forcing of tropical monsoon clouds: Results from TRMM observations. *J. Climate,* **14**, 1511-1524.

Zhang, G. J. and N. A. McFarlane, 1995: Sensitivity of climate simulations to the parameterization of cumulus convection in the Canadian Climate Centre General Circulation Model. *Atmos.-Ocean*, **33**, 407-446.

Chapter 5

Sensitivity of Aerosol Concentrations to the Spatial Distribution of Precipitation

5.1 Introduction

Aerosol particles are relatively short lived in the atmosphere, with typical lifetimes of 1 to 8 days (Andreae 1995). Nevertheless, a growing number of studies are documenting the long-range transport of aerosols thousands of kilometers from their sources (*e.g.*, Clarke et al. 2001; Posfai et al. 1999). Aerosols are known to have several important impacts on the thermodynamic structure of the surface and atmospheric column and their concentrations are expected to grow as a result of industrialization, biomass burning and changes in land-use (Houghton 2001). It is the climate effects of aerosols together with their transport and accumulation in the atmosphere that are causing aerosols to be increasingly viewed as a global environmental concern in addition to a regional air quality problem. This chapter presents a study of aerosol precipitation scavenging, the primary process by which aerosols are removed from the atmosphere. The details of this process, which are poorly constrained by observations, may have important consequences for determining the lifetimes of aerosol particles and their ability to be transported far from their sources.

The direct radiative effect of aerosols is a cooling which results from the scattering of solar energy back to space. Globally, this effect is estimated for the entire column to be in the range of approximately -0.1 to -1.0 W m^{-2} for industrial aerosols and -0.1 to -0.5 W m^{-2} for particles resulting from biomass burning (Houghton 2001). The presence of dark carbonaceous aerosols, however, can lead to a warming of the atmosphere owing to the absorption of sunlight. This observation has led to the conclusion that the column radiative

forcing may, depending on the composition of the aerosol, be the difference between a much stronger surface cooling and atmospheric warming. The Indian Ocean Experiment (INDOEX) determined that the direct radiative influence of black carbon in the wintertime haze layer over the Northern Indian Ocean was an average atmospheric warming of 18 W m^{-2} and surface cooling of -20 W m^{-2} (Ramanathan et al. 2001a). Aerosols are also suspected of modifying the planetary energy budget by increasing the reflectivity of clouds, leading to surface cooling (Twomey 1977), evaporating low clouds, leading to surface heating (Ackerman et al. 2000), suppressing precipitation (Rosenfeld 2000), and perhaps an entire slowing of the hydrological cycle (Ramanathan et al. 2001b). Global values for these indirect aerosol forcing effects remain highly uncertain.

The primary removal process for many aerosol species is scavenging by precipitation. This process occurs both through the nucleation by aerosol particles of cloud droplets that eventually grow large enough to precipitate, as well as the sweep-out of particles below cloud that are impacted by falling droplets (Scott 1978). Quantitative estimates of the scavenging rate are difficult to obtain observationally. Most have been made either through numerical simulation of precipitation and aerosol/cloud microphysics in regional- or global-scale models (where both are highly parameterized), or determined as a residual in large-scale budget estimates. This quantity however is likely to be highly variable and depend strongly on the precipitation regime in the region (*i.e.*, broad stratiform precipitation versus cellular convective precipitation) as well as the proximity of the aerosol source to precipitating clouds.

In addition to aerosol lifetime studies, numerical models are also relied upon for global determinations of climate forcing by aerosols (*e.g.*, Kiehl and Briegleb 1993). Unfortunately, the simulation of precipitation may be biased in coarse models where convection must be parameterized. The frequency distribution of rain rate in satellite observations and a coincident atmospheric simulation using the Model for Atmospheric Transport and

1 Feb. - 21 Feb. 2002 (20S-20N; 40E-110E)
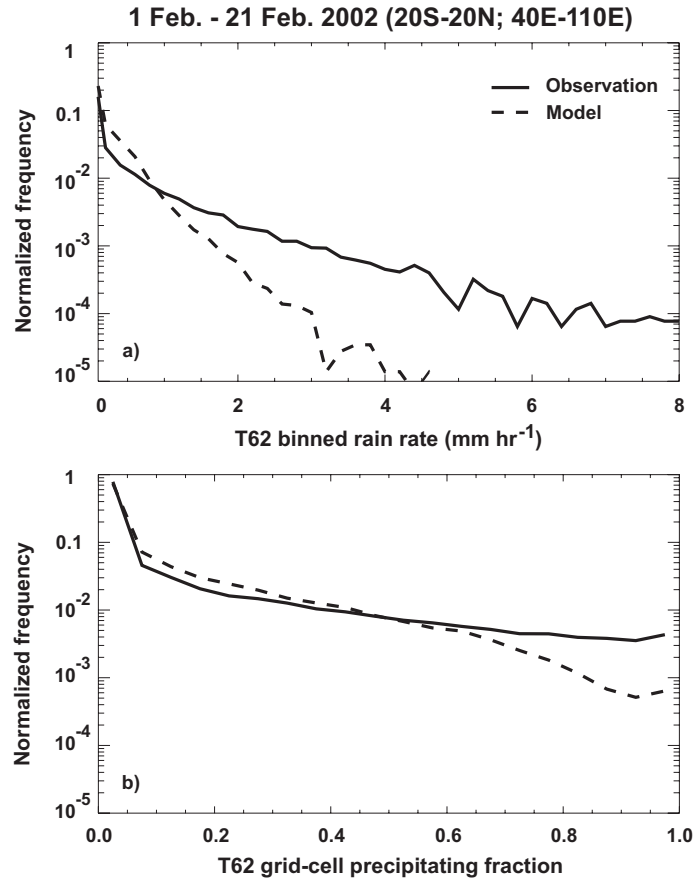
Fig. 5.1. Frequency distributions of (a) rain rate (in mm hr⁻¹), and (b) grid cell precipitating fraction. Solid lines are observations from a multi-platform satellite data set. Dashed lines are simulated rain rates from the MATCH global atmospheric model. All are averages over MATCH grid boxes at T62 resolution.

Chemistry (MATCH) are shown in Fig. 5.1 for precipitation over the Indian Ocean during the winter monsoon. The model is run at the standard T62 resolution (approximately 200 km × 200 km grid cells) and the satellite data have been averaged over the same grid. Extreme precipitation events, some with rain rates exceeding 8 mm hr⁻¹, are evident in satellite observations, while virtually no precipitation greater than 4 mm hr⁻¹ is present in the simulation. Furthermore, rain rates greater than 1 mm hr⁻¹ occur more frequently in the observations than in the model, while rain rates lower than 1 mm hr⁻¹ occur more frequently in the model. The bulk of precipitation in regions of tropical deep convection falls in a relatively few extreme precipitation events. In contrast, simulated precipitation

occurs as broadly distributed gentle precipitation. Wilcox (2002) has argued that this bias results from an absence of fundamental mesoscale convective processes in the convection parameterization of the model.

Because the dynamical structures that produce precipitation are often assumed to be smaller than a model grid cell, another parameter that often enters the numerical simulation of precipitation scavenging is the fraction of the grid cell experiencing rain. Again, the satellite data indicates that this quantity is biased in model simulations. Fig. 5.1b compares the frequency distribution of precipitating fraction in the bottom layer grid cells of the atmospheric model to satellite observations of surface precipitating fraction. The model makes an estimate of the precipitation fraction for each grid cell based on grid cell-averaged value of the production rate of precipitation, as well as the rate of precipitation from above the grid cell, using a parameterization described in section 5.2.2. For comparison, the model grid has been superimposed on the satellite observations and the fractional coverage by observed precipitation of each grid cell is determined. The relative frequency with which grid cells are filled to 60% or less with precipitation is similar in the model and observations. However, precipitating fractions greater than 60% are more frequent in the observations than in the model. While approximately one in every 500 grid cells will be completely filled with precipitation in the observations, only about one in every 5000 will in the model. Low precipitating fractions are consistent with the common assumption that the processes associated with atmospheric convection occur predominantly at scales that are smaller than a grid cell. The observations indicate that a substantial portion of monsoonal precipitation falls in mesoscale precipitation features that exceed the scale of a single model grid cell (Wilcox and Ramanathan 2001).

The purpose of this study is to test the sensitivity of simulated aerosol distributions to the model biases identified above by integrating high-resolution satellite precipitation observations into the MATCH chemical transport model. Separate simulations are per-

formed to test the effects of implementing observed rain rates and observed rain fractions in the scavenging scheme. The model configuration places a tracer source in the surface layer over India to simulate an idealized aerosol. This study compares the horizontal and vertical distributions of aerosol over the Indian Ocean basin using different scavenging criteria. In addition, the role of precipitation in limiting the long-range transport of aerosols beyond the Indian Ocean region is considered.

Aerosols transported off of South Asia during the winter monsoon travel south until they reach the Inter-tropical Convergence Zone (ITCZ). Here the aerosol-laden air masses encounter giant cloud systems containing intense precipitating structures, which provide a potent barrier between the northern and southern hemisphere flows. Despite uncertainties in the estimates of aerosol residence times, the efficiency of precipitation scavenging is evident in data from aircraft flights during INDOEX. A strong gradient was observed in aerosol particle concentrations, from about 1500 cm^{-3} in the Northern Indian Ocean to about 250 cm^{-3} in the Southern Indian Ocean (Ramanathan et al. 2001a).

5.2 Methodology

MATCH is a numerical simulation of the transport of atmospheric constituents based on observed meteorology. The model acquires observed pressure, wind and humidity fields from the NCEP meteorological reanalysis product in order to compute the transport. Precipitation, however, is not provided by the reanalysis data set, therefore MATCH computes precipitation by using standard parameterizations from the NCAR Community Climate Model version 3 (CCM3). Simulated precipitation results from two separately computed processes. Deep convection, which is fully parameterized in the model, is the dominant source of tropical precipitation. Additionally, a small amount of precipitation is produced by stable condensation, which occurs when a grid cell becomes super-saturated. The excess moisture, above saturation, is removed from the grid cell and falls as precipitation. Once the precipitation rate is diagnosed, MATCH computes the scavenging rate by determining the

Table 5.1. Simulation configurations.

name	precipitation source	scavenging parameterization	scavenging computation [*]
STD	MATCH	MATCH parameterization	Eqns 5.1-5.3
NOSCAV	not applicable	none	
SAT1	satellite	MATCH parameterization	Eqns. 5.1-5.3 $\langle \dot{Q} \rangle$ from satellite
SAT2	satellite	proportional to observed precipitating fraction (no ice phase scavenging)	Eqn. 5.1 F_p from satellite
SAT3	satellite	proportional to observed precipitating fraction (with ice phase scavenging)	Eqn. 5.1 F_p from satellite

[*]   see sections 5.2.2 and 5.2.4.

fraction of aerosol in each grid box to be removed. This depends in large part upon the grid cell precipitation fraction (Balkanski et al. 1993), which is parameterized as a function of the rate of production of precipitating water (see section 5.2.2). To assess the vulnerability of simulated aerosol transport to the representation of precipitation processes in these parameterizations, this study modifies MATCH to receive satellite observations of precipitation at 3 hour intervals.

Comparisons are made of aerosol distributions resulting from five MATCH simulations. The first run (STD) uses the standard configuration of the MATCH model. Precipitation is computed using the parameterizations of convection and stable condensation, and the scavenging rate is computed using the standard parameterization (see section 5.2.2). The second run (NOSCAV) is performed with no precipitation scavenging and establishes an upper bound on the distribution of aerosol. Three separate simulations are performed using satellite observed precipitation. The first (SAT1) tests the sensitivity to the bias in rain rate shown in Fig. 5.1a by replacing model derived rain rates with observed rain rates in the scavenging parameterization. The last two simulations (SAT2 and SAT3) test the precipitating fraction bias apparent in Fig. 5.1b by using the observed precipitating fraction (instead of rain rate) in a new parameterization of scavenging. The satellite-based scavenging
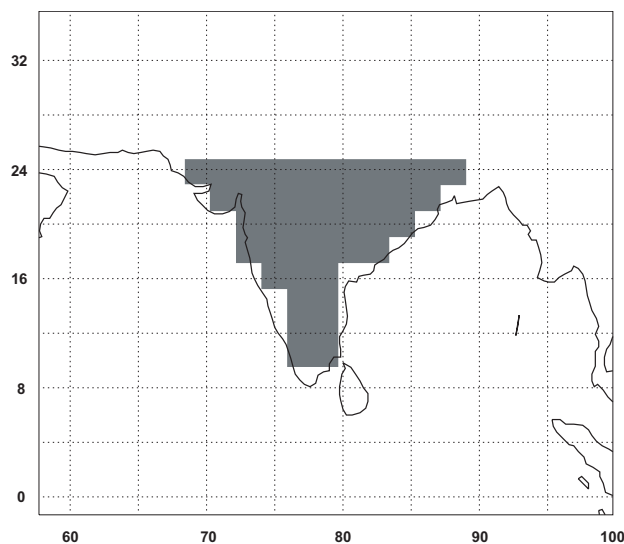
Fig. 5.2. Shaded MATCH grid cells indicate the location of the steady, uniform aerosol source in the bottom layer of the model. Source rate is 2.25 μg m^{-2} s^{-1}.

computation is described in section 5.2.4. The separate model runs are summarized in Table 5.1.

This study focuses on the transport of aerosol from the Indian subcontinent during the winter monsoon. A uniform and steady source of 2.25 μg m^{-2} s^{-1} is applied in the bottom layer of the model over India (see Fig. 5.2 for location of source area). The emissions rate is based on the time- and space-averaged emissions of Rasch et al. (2001) for sulfate, dust and carbonaceous aerosols in South Asia during the INDOEX period. The model is run for 21 days beginning 1 Feb. 2002.

5.2.1 MATCH chemical transport model

MATCH is designed to simulate the sources, sinks and advection of aerosol and trace gas species within the atmosphere. MATCH is an "off-line" transport model, meaning that it is configured to take archived meteorological analysis data sets as input. A description of the data assimilation process, as well as many of the parameterizations used in MATCH can be found in Rasch et al. (1997). The model is run at T62 horizontal resolution (approximately
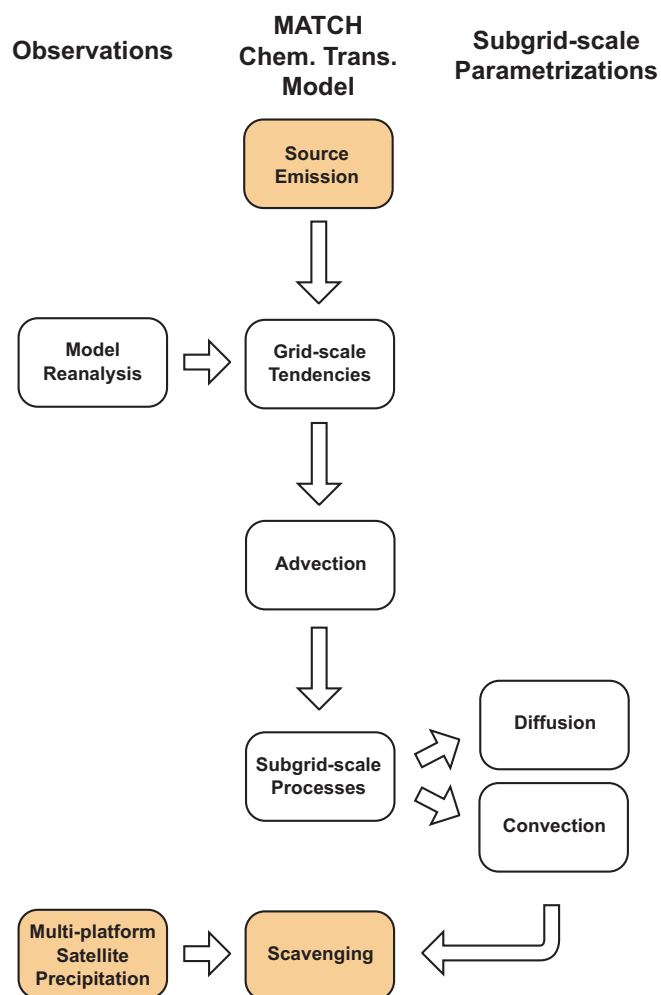
Fig. 5.3. Flow chart for MATCH indicating, in the center column, the key processes acting on simulated aerosol species. Aerosol sources are specified and then advected by grid-scale tendencies determined by the NCEP meteorological reanalysis data set. Advection due to subgrid-scale processes of diffusion and convection are determined by model parameterizations. Experiments are performed here where aerosol removal by precipitation scavenging is determined either by precipitation diagnosed by subgrid-scale parameterizations or observed by satellites. Colored boxes indicate model components that are added or modified in this study. All other components are in the standard MATCH configuration.

200 km ✕ 200 km at the equator) and 28 vertical levels. Some details regarding the convection and scavenging parameterizations are presented below. MATCH has been used for emissions studies (Mahowald et al. 1997a), transport and scavenging of trace gases (Mahowald et al. 1997b; Crutzen and Lawrence 2000), transport of photochemically active species (Lawrence et al. 1999), and transport of tropospheric aerosols (Collins et al. 2001).

A flow chart for MATCH appears in Fig. 5.3. Sources of aerosol are specified and advected by grid-scale tendencies determined by meteorological variables provided by the 3-hourly NCEP/NCAR reanalysis data set (Kalnay et al. 1996). Because significant fluxes of aerosol can result from subgrid-scale contributions to convection and diffusion, additional parameterizations are included in MATCH to compute these tendencies based on the meteorology from the reanalysis product. The deep convection parameterization (Zhang and McFarlane 1995) produces a large portion of the simulated precipitation, particularly in the Tropics. According to the scheme, mass fluxes of a subgrid-scale ensemble of convective updrafts and downdrafts is predicted based on the quantity of convective available potential energy determined from grid cell values of temperature and humidity. Precipitation is produced at a rate that is proportional to the mass flux of the updrafts and a fraction of that precipitation is evaporated in the downdrafts.

Meteorological quantities from the reanalysis data set are provided every 3 hours; however, because of the model resolution and the time scales of subgrid-scale processes, MATCH is operated with a 30-minute time step. Therefore the 3-hourly reanalysis quantities are linearly interpolated to the 30-minute temporal resolution.

5.2.2 Precipitation scavenging parameterization

This section describes the standard MATCH parameterization for precipitation scavenging which is used in the STD and SAT1 simulations. Precipitation scavenging in MATCH is calculated separately for the removal due to the conversion of cloud droplets to precipitating drops within the cloud (in-cloud scavenging), as well as the sweep-out of aerosol by precipitation from above (below-cloud scavenging). In the standard configuration of the model, separate values of precipitation are diagnosed for convection and stable condensation, where stable condensation results from the super-saturation of an entire grid cell. Therefore, for each grid cell there are up to 4 separate scavenging rates, in-cloud and below-cloud scavenging for both convective precipitation and stable condensation. Each of

the four types of scavenging is assumed to be occupying a separate portion of the grid cell, so all four are added together to determine the total aerosol amount scavenged.

The scavenging parameterization is based on the original formulation of Giorgi and Chameides (1986), a simple first-order scheme where the removal rate is proportional to a parameter F_p:

$$\frac{\Delta n}{\Delta t} = \frac{nF_p}{\Delta t} \quad .$$ (5.1)

n is the aerosol mass mixing ratio in kg kg^{-1} and Δt is the model time step (30 minutes). Strictly speaking, F_p is the fraction of aerosol in the grid cell that is removed. In the following computation, it is assumed that the aerosol is highly soluble. Under this assumption, all of the aerosol within the cloudy portion of the grid cell is assumed to reside within cloud droplets or precipitating drops. Because highly soluble aerosols are efficiently scavenged by precipitation, F_p is approximately equivalent to the fraction of the grid cell that is precipitating.

Computing F_p begins with determining the fraction of the grid cell occupied by cloud or precipitation, F_{cp}, which is determined in the NCAR CCM3 cloud parameterization scheme (Rasch and Kristjánsson 1998) as the greater of:

$$F_{cp} = \frac{\left\langle F_c \dot{P} \right\rangle_{above}}{\left\langle \dot{P} \right\rangle_{above}} \times \frac{\left\langle \dot{P} - \dot{E} \right\rangle_{above}}{\left\langle \dot{P} \right\rangle_{above}} \qquad \text{or} \qquad F_c .$$ (5.2)

F_c is the standard cloud fraction from the NCAR CCM3. It is largely based on the relative humidity as in Slingo (1987) and modified as described in Rasch and Kristjánsson (1998). $\dot{P}$ is the production rate of rain water and $\dot{E}$ is the evaporation rate of rain (both in kg m^{-2} s^{-1}). Both are computed with the cloud and convection parameterizations of the model. The $\left\langle \ \right\rangle_{above}$ operator denotes the sum over the grid cells above the grid cell at which F_{cp} is being computed.

The precipitating fraction of the grid cell is then estimated as

$$F_{\dot{p}} = F_{cp}\frac{\dot{Q}}{L} \qquad\qquad (5.3)$$

where $\dot{Q}$ is the net production rate of precipitating water and equal to $\dot{P} - \dot{E}$. Also note that the vertically integrated value through the column, $\langle\dot{Q}\rangle$, is equal to the surface rain rate. L is the total condensed water amount in kg m^{-2}.

In the case of precipitation by stable condensation (denoted by subscript sc), $\dot{Q}_{sc}$ and L_{sc} are computed by the as part of the Rasch and Kristjánsson (1998) cloud scheme. Therefore they are inserted in to Eqn. 5.3 to compute the precipitating fraction for in-cloud scavenging by stable condensation.

For convective precipitation (denoted by subscript c), $\dot{Q}_c$ is computed by the convection parameterization (Zhang and McFarlane 1995), however L_c is not. L_c is therefore assigned the approximate value of 10 kg m^{-2} as in Balkanski et al. (1993). This may be an overestimate and generally ensures that the grid cell precipitating fraction for in-cloud scavenging by convective precipitation is less than 0.1, which is consistent with the assumption that convective precipitation occurs at scales significantly smaller than the model grid cell.

Below-cloud scavenging in nature is determined by the volume swept out by each precipitating drop as it falls from the cloud to the ground (Scott 1978). Lacking a reliable estimate of the number and size of the precipitating drops for either the stable condensation or the convective precipitation, Eqn 5.3 is used for below-cloud scavenging. L is again assigned the value of 10 kg m^{-2} and $\dot{Q}$ is replaced with $\langle\dot{Q}_{sc}\rangle_{above}$ for stable condensation falling from above and $\langle\dot{Q}_c\rangle_{above}$ for convective precipitation from above.

In cloud scavenging is assumed to occur primarily in the liquid phase. At levels between 0°C and -20°C (where liquid and ice are assumed to be mixed) scavenging is reduced by a factor that decreases linearly with temperature from 1 at 0°C to 0 at -20°C. Thus no in-cloud scavenging occurs above the -20°C level. Below cloud scavenging is allowed in the

liquid, ice or mixed phases.

The scavenging scheme described above has been used in a number of models, beginning with that of Giorgi and Chameides (1986), to account for scavenging when details such as the subgrid distribution of precipitation and drop size and number distributions cannot be reliably predicted. It is used here because the goal of the SAT1 experiment is to test a common scavenging scheme where precipitation rate has been replaced with observations, and because it makes an estimate of the grid cell precipitating fraction which can be directly replaced with satellite observations (SAT2 and SAT3 simulations). It is not the purpose of this study to develop a new scavenging scheme for global scale models. According to the scheme, total scavenging is dominated by in-cloud scavenging by stable condensation (Eqn. 5.1). This largely reflects a common assumption that convective precipitation occupies only a small portion of the grid cell it occupies. However, given that most tropical precipitation is produced by the convection parameterization in the model, while known observationally to occur in mesoscale convective structures that can be large enough to fill a single grid cell, the scavenging parameterization likely underestimates scavenging by convective precipitation and overestimates scavenging by stable condensation.

5.2.3 Three-hourly multi-platform satellite precipitation measurements

Precipitation measurements are provided by a blending of measurements from several satellite platforms (Huffman et al. 2001). Complete documentation for the data set is provided by and Huffman and Bolvin (2002), however a few details are described here. Surface rain rate is measured, where available, from each of four passive microwave sensors. Three are Special Sensor Microwave Imagers (SSM/I) mounted on separate Defense Meteorological Satellite Program (DMSP) spacecraft (F13, F14 and F15). DMSP satellites are sun-synchronous polar orbiters with equator crossing times of 5:45, 8:30 and 9:20 respectively. The fourth microwave instrument is the Tropical Rainfall Measuring Mission (TRMM) Microwave Imager (TMI), which has a 46 day precessing orbit with an

equator crossing time that passes through all local hours during the 46 day period. Each microwave instrument is a multi-spectral microwave instrument sensitive to the emission and scattering characteristics of precipitating hydrometeors at wavelengths between 3.5 mm and 2.8 cm. Inversion from microwave brightness temperatures to hydrometeor profiles and surface rain rates is performed using the Goddard Profiling Algorithm (GPROF; Kumerrow et al. 2001). Intercalibration between the microwave instruments is performed whereby all SSM/I retrievals are adjusted by a factor determined by matching the SSM/I retrievals to TMI retrievals where they overlap.

The combined passes of the microwave instruments capture about 40% of the area of the Indian Ocean region during the 21 days of this study. Infrared (IR) estimates of rain rate from geosynchronous satellites are used to fill in the gaps between the microwave measurements. Over the Indian Ocean region, those measurements are provided by the METEOSAT-5 satellite. Precipitation is assigned to all IR pixels with brightness temperature colder than a variable threshold value, which is determined by colocated TMI measurements. The threshold is assigned such that the frequency distribution of 0.25° averaged rain rate in the IR retrieval agrees with the corresponding frequency in the TMI retrievals. The threshold is updated each time step of the precipitation data set using all colocated IR/TMI observations in the region during a 30 day period centered on the time step. The resulting merged microwave/IR data set is provided globally, every three hours beginning 29 Jan. 2002, at 0.25° resolution.

5.2.4 Satellite-based scavenging computation

In the formulation of the scavenging parameterization described in section 5.2.2, the amount of aerosol removed is determined by the grid cell precipitating fraction, F_p, which in turn is determined by the production rate of rain water, $\dot{Q}$. In the SAT1 simulation, the goal is to constrain the computation of F_p in Eqn 5.3 with observed rain rates rather than simulated rain rates. Unfortunately, the precipitation observations only provide a

reliable estimate of the surface rain rate, which is an integral of the production rate of rain water throughout the column above (*i.e.*, $\langle \dot{Q} \rangle$ rather than $\dot{Q}$). This profile of rain production is required by the scavenging parameterization to determine the vertical extent of the scavenging event and the amount removed from each level. Thus a database of MATCH profiles of rain production are taken from the entire 21-day STD simulation and grouped according to surface rain rate. Then a set of 7 average profiles are constructed where all profiles corresponding to rain rates within a factor of 10 in mm hr^{-1} are averaged together. For example, all profiles with MATCH surface rain rates between 10^{-6} and 10^{-5} mm hr^{-1} are averaged together. Likewise, all profiles with rain rates between 10^{-5} and 10^{-4} mm hr^{-1} are averaged together, and so on up to 10 mm hr^{-1}. Scavenging in the SAT1 simulation is performed by applying the profile corresponding to the bin in which the satellite observed surface rain rate falls. Although the sizes of the rain rate bins are broad, the standard deviation of rain production at most levels and most rain rate bins is less than 10%. Therefore, in the SAT1 simulation, scavenging is constrained by observed $\langle \dot{Q} \rangle$.

Scavenging in the SAT2 and SAT3 simulations is computed using Eqn. 5.1, where F_p is the fraction of the surface area at the bottom of the model grid column with non-zero surface rain rate in the satellite data. All aerosol residing within the fraction of the column, F_p, is removed with the constraint that the vertical extent of the scavenging is limited by the vertical extent of rain production in the average profiles described above. In the SAT2 simulation, scavenging is reduced at levels between 0°C and -20°C and does not occur at levels colder than -20°C. In the SAT3 simulation, ice phase scavenging above the freezing level is not restricted. Because all aerosol in the precipitating fraction of the grid cell is scavenged in the SAT3 simulation, it serves as an upper bound on aerosol scavenging. However, by being consistent with Eqn. 5.1, it provides a direct validation of the standard scavenging parameterization by replacing diagnosed values of F with observed values.

Although MATCH has a time step of 30 minutes, the satellite data are only provided

Table 5.2. 21-day averages over Indian Ocean region (30S-30N,40-110E).

	Satellite observations	MATCH (standard model)
precip. (mm day^{-1}), $\left\langle \overline{\dot{Q}} \right\rangle$	2.7	4.2
% grid cells containing rain	29	80
% coverage of surface precip., $\overline{F_p}$	7.7	6.8

*   overbar denotes time and space averaging.

every three hours. Therefore, the same rain rate values are applied for each 30-minute time step within the 3-hour period. The aerosol is assumed to mix entirely within the grid cell during each 30-minute time step. Thus if a portion of a grid cell is swept clean by precipitation in one time step, aerosol from the remaining portion of the grid cell is made available in the next time step to be swept by the same precipitation feature. This likely results in an overestimation of scavenging, however this assumption is made within all of the simulations compared here, including the STD simulation.

5.3 Simulated and observed precipitation distributions

Fig. 5.1 illustrates an important bias in the model representation of precipitation, specifically that the bulk of simulated precipitation falls as drizzle at the expense of more intense precipitation events. Conversely, as indicated in Table 5.2, the model produces significantly more precipitation than is observed when simulated and observed rain rates are averaged over the entire Indian Ocean basin and 21 day period. The model produces 4.2 mm day^{-1}, while only 2.7 mm day^{-1} is observed. This occurs in spite of the fact that the convection parameterization in the model is constrained by the 3-hourly grid cell-scale reanalysis of meteorological observations. Fig. 5.4 is a comparison of the 21-day mean rain rate over the Indian Ocean basin in MATCH and observed by satellite. The maps clearly indicate that precipitation occurs as more broadly distributed, gentle precipitation in MATCH, with the entire ITCZ region precipitating at an average rate of at least 5 mm day^{-1}. Furthermore, the percentage of grid cells containing precipitation is much higher, by about

21-day mean rain rate (mm day^{-1})

MATCH
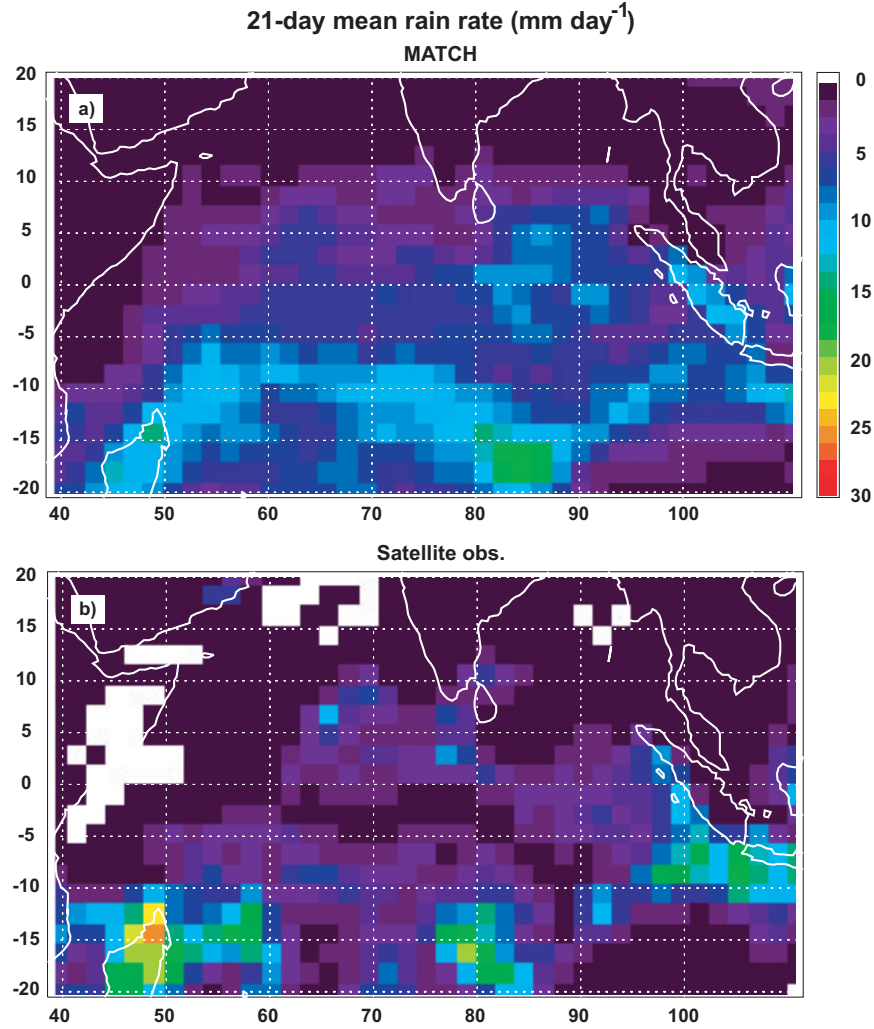
Satellite obs.

Fig. 5.4. Feb. 1-21, 2002 mean rain rate over the Indian Ocean basin in (a) the MATCH simulation and (b) the satellite observations. Rain rates are in mm day^{-1} and averaged over MATCH grid boxes at T62 resolution.

60%, in MATCH compared to the T62 gridded satellite data, as a result of the broad and steady simulated precipitation. Note that although may more grid cells are precipitating in the model, the scavenging parameterization generally predicts smaller grid cell precipitating fractions (F_p), and the mean precipitating fraction differs from the observed value by only about 1%.

In both the satellite data and the MATCH simulation, precipitation occurs primarily

within a band between 10º S and 20º S latitude, corresponding to the ITCZ typical of the winter monsoon. Three regions of peak precipitation are located over the north coast of Madagascar (50º E), directly south of the tip of India (80º E) and near Indonesia (100º E). Precipitation is stronger at each of these peak regions in the satellite observations by nearly 5 mm day^{-1}. Most other areas have lower mean rain rates in the satellite observations than the MATCH simulation.

5.4 Simulated aerosol distributions

The vertically integrated aerosol distributions after 21 days over the Indian Ocean basin for each of the 5 simulations is shown in Fig. 5.5. Also shown are the values for average aerosol burden over the entire region. The NOSCAV simulation (Fig. 5.5b) puts an upper bound on the aerosol amounts. In the absence of precipitation scavenging, aerosol spreads well south of the equator within 21 days. The average aerosol burden over the region is 31 mg m^{-2}. About 45% of the total aerosol is removed when the standard MATCH scavenging is applied (STD, Fig. 5.5a) and about 40% is removed using the standard MATCH parameterization with observed rain rates (SAT1, Fig. 5.5c). The aerosol burden is reduced by nearly 60%, however, when the fraction of aerosol removed is directly proportional to the observed grid cell fraction of precipitation (SAT2 and SAT3). The slightly higher aerosol amount in the SAT1 simulation relative to the STD simulation indicates there is only a weak dependence of aerosol scavenging on the distribution of rain rates, and may be due to the lower overall amount of precipitation in the satellite measurements. The higher removal rate in the SAT2 and SAT3 simulations indicates a stronger effect for biases in the grid cell fraction of precipitation.

In all simulations with precipitation scavenging, significant aerosol removal occurs within the ITCZ, corresponding with the region of maximum precipitation. ITCZ aerosol removal is most effective in the SAT2 and SAT3 simulations, particularly in the eastern portion of the ITCZ and the region over Indonesia. This may reflect the fact that grid cell

Aerosol burden after 21 days (g m^{-2})

Fig. 5.5. Vertically integrated aerosol burden over the Indian Ocean basin after 21 days in (a) the STD simulation, (b) the NOSCAV simulation, (c) the SAT1 simulations, (d) the SAT2 simulation, and (e) the SAT3 simulation. Units are g m^{-2}.

precipitating fractions greater than 0.8 occur much more frequently in the observations than the model. Such high raining fractions correspond to the more extreme rain rate events that occur along the ITCZ and near Indonesia. Note, however, that even in the STD

Aerosol burden after 21 days (g m^{-2})

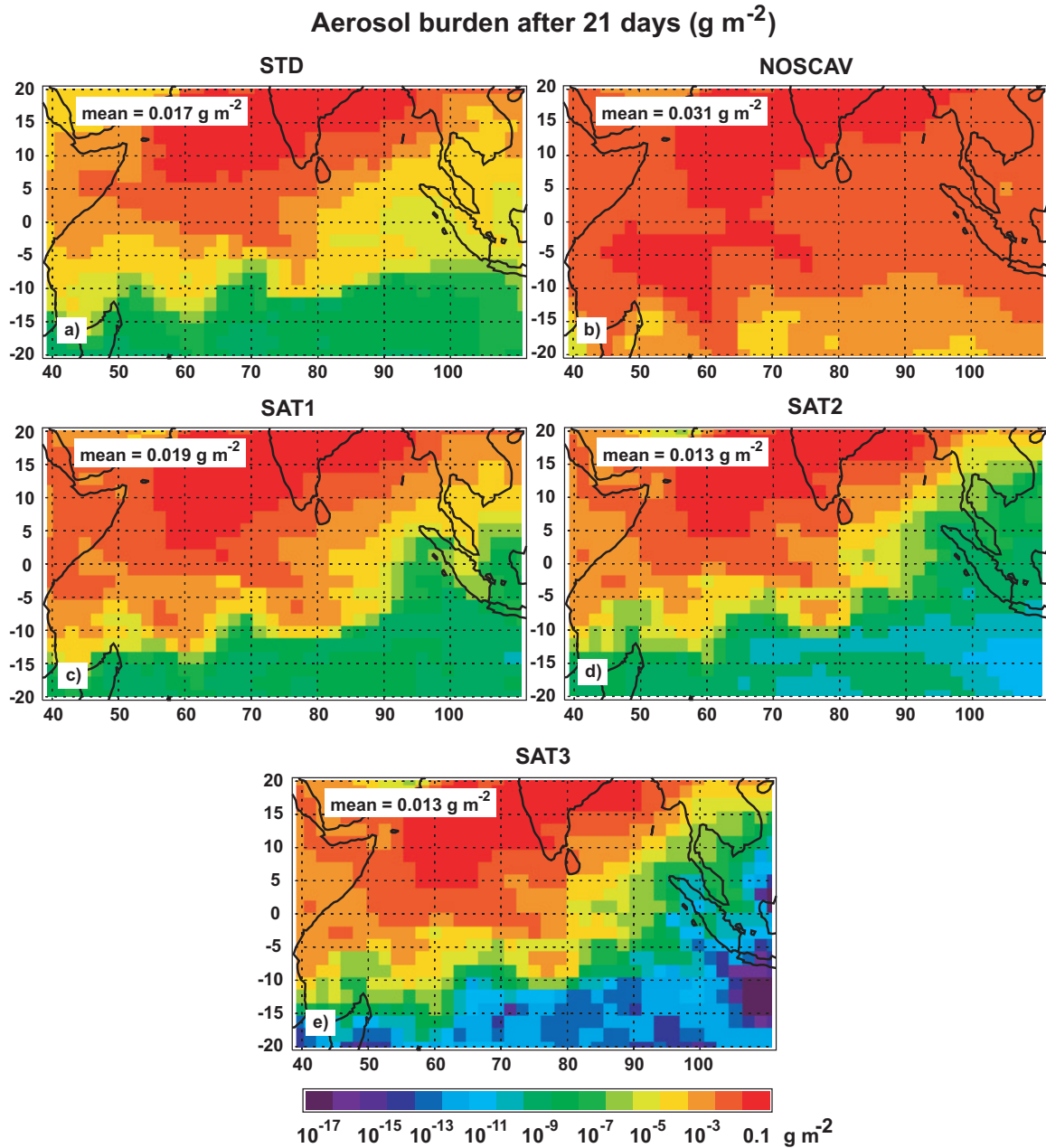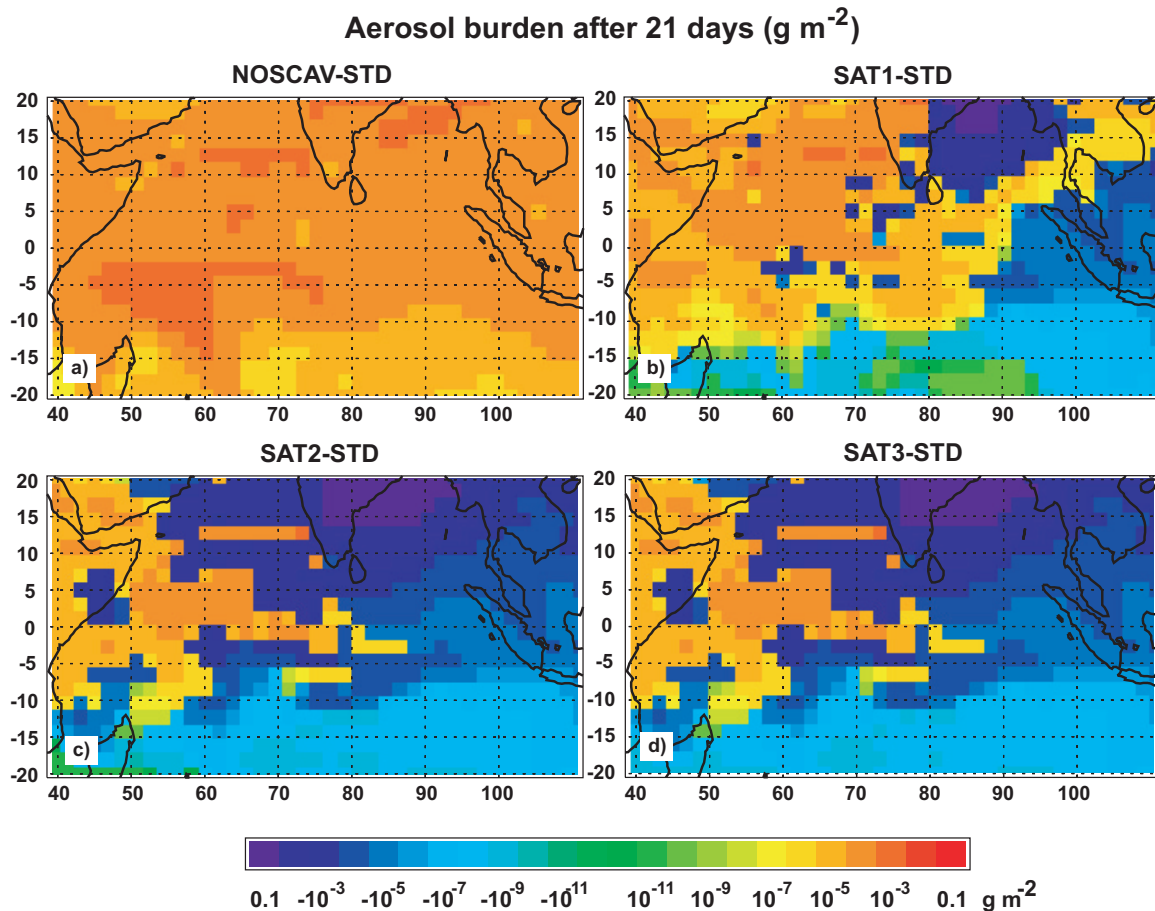**Fig. 5.6.** Difference of the vertically integrated aerosol burden over the Indian Ocean basin after 21 days in the STD simulation and (a) the NOSCAV simulation, (b) the SAT1 simulations, (c) the SAT2 simulation, and (d) the SAT3 simulation. Units are g m^{-2}.

and SAT1 simulations, the ITCZ values are several orders of magnitude smaller than in the NOSCAV simulation. Other important differences between the SAT simulations and the STD simulation occur in regions where modest amounts of precipitation occur in the MATCH simulation but none or only trace amounts are observed. These regions have a greater amount of aerosol in the SAT simulations than the STD simulation. This occurs in the western portion of the latitude band between 0° and 10°S as well as the east coast of Africa north of Madagascar. They appear as orange regions in the difference plots shown in Fig. 5.6. An exception to this is the region north of Indonesia, which received less

1 Feb. - 21 Feb. 2002 (20S-20N; 40E-110E)
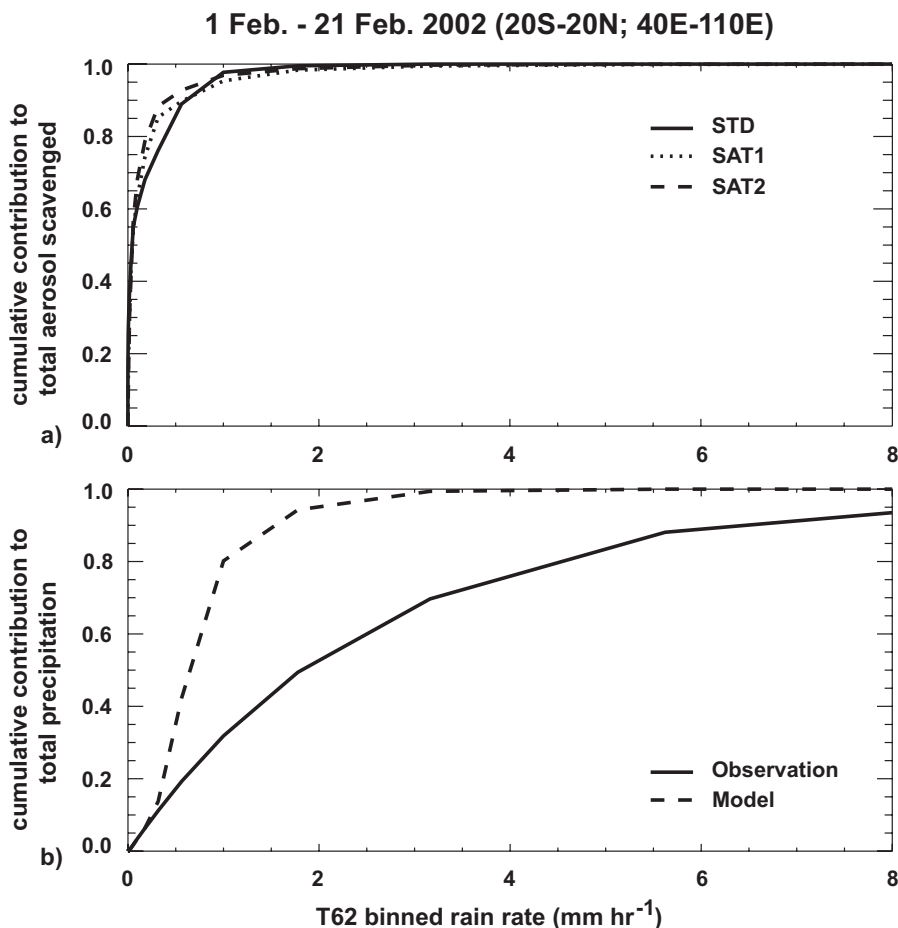
Fig. 5.7. (a) Cumulative contribution to the total aerosol scavenged over the Indian Ocean basin as a function of rain rate. Solid line is STD simulation, dotted line is SAT1 simulation, and dashed line is SAT2 simulation. (b) Cumulative contribution to the total amount of precipitation over the Indian Ocean basin as a function of rain rate. Solid line is satellite observations and dashed line is MATCH model.

precipitation than is simulated by MATCH but has a higher column amount of aerosol in the STD simulation than the SAT2 and SAT3 simulations.

In spite of the differences described above, the aerosol distributions in all of the simulations except for the NOSCAV simulation are similar. In general, the ITCZ represents a significant barrier to the transport of aerosol regardless of how the scavenging is calculated. The cumulative contribution to the total amount of aerosol scavenged is shown in Fig. 5.7a as a function of rain rate for all 5 simulations. For reference, the

Aerosol profiles after 21 days (g kg⁻¹)
40 - 110E longitude
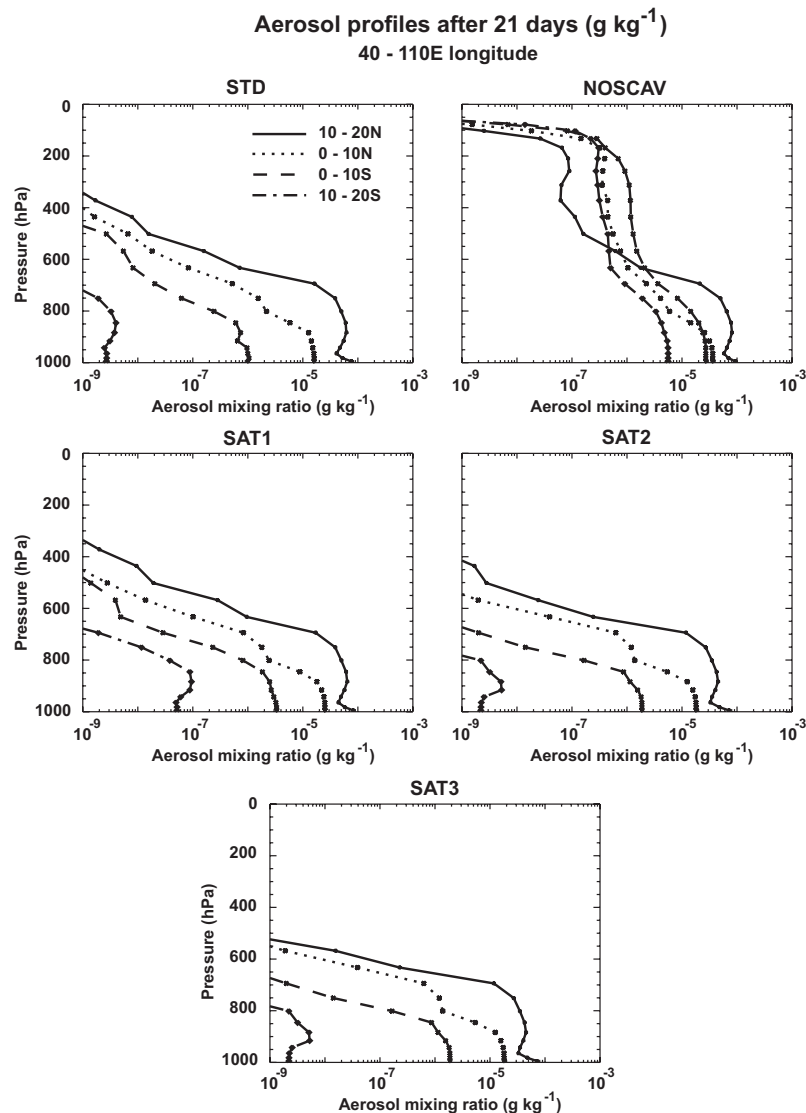
Fig. 5.8. Vertical profiles of aerosol mixing ratio over the Indian Ocean basin in 10° latitude bands for the (a) STD simulation, (b) NOSCAV simulation, (c) SAT1 simulation, (d) SAT2 simulation, and (e) SAT3 simulation. Units are g kg⁻¹.

cumulative contribution to total precipitation as a function of rain rate is shown in Fig. 5.7b.

Virtually all scavenging occurs at rain rates less than 1 mm hr⁻¹ even while such light rain

events account for a relatively small portion of the total amount of precipitation. This may

explain why scavenging is not particularly sensitive to the distribution of rain rates. The

most important issue is properly determining whether or not precipitation has occurred in

the grid cell.

The vertical distributions of aerosol show a greater sensitivity to biases in the grid cell fraction of precipitation (SAT2 and SAT3) than to biases in rain rate (SAT1). Fig. 5.8 shows vertical profiles of aerosol mixing ratio averaged over 10° latitude bands in the Indian Ocean basin. Without precipitation scavenging, aerosol is allowed to accumulate in the upper troposphere because of vertical transport by convection (Fig. 5.8b). Mixing ratios of 10^{-7} g kg^{-1} or greater are found in every latitude band within a broad layer between 600 hPa and 200 hPa. However, when precipitation scavenging is applied, aerosol transport above 600 hPa is significantly reduced. Differences in the low-level north-south gradient in aerosol amount are also apparent. North of the equator, aerosol amounts below 800 hPa are similar. Between 0° and 10°S, the low-level amount in SAT1 is a factor of 3 larger than the STD simulation and the SAT2 and SAT3 simulations are a factor of 2 larger. Between 10°S and 20°S, the low level amount in SAT1 is more than one order of magnitude larger than the STD simulation. SAT2 and SAT3 boundary layer amounts in this latitude band are only slightly smaller than STD. In the SAT2 and SAT3 simulations, aerosol concentrations above 800 hPa are lower in all latitude bands than in the STD or SAT1 simulations, suggesting that scavenging based on observed precipitating fraction is more effective at scavenging in the middle and upper troposphere. Differences between the SAT2 and SAT3 simulations reflect the effects of ice phase scavenging, and are only apparent above 500 hPa in the 20° - 10°N latitude band. Near the source region, upper-tropospheric aerosol amounts are lower in the SAT3 simulation because of removal by ice. Further north, in the center of the source region, the difference in upper-tropospheric aerosol between SAT2 and SAT3 is more pronounced (not shown).

5.5 Long-range transport of aerosols

There are two primary pathways for aerosol transported beyond the region of the Indian subcontinent and Indian Ocean. The most significant is to the northeast of India

Aerosol burden after 21 days (g m^{-2})
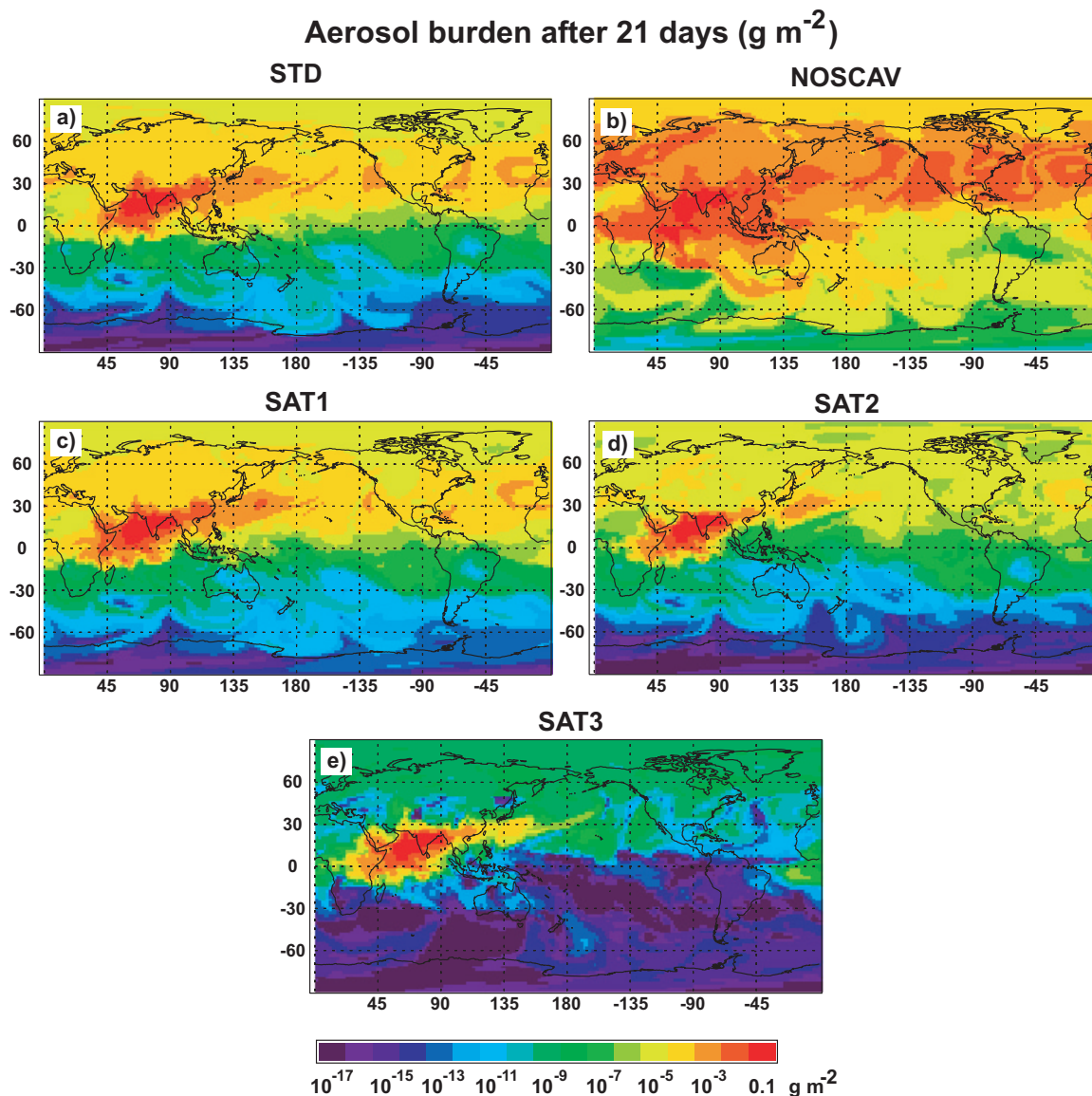
Fig. 5.9. Vertically integrated aerosol burden over the globe after 21 days in (a) the STD simulation, (b) the NOSCAV simulation, (c) the SAT1 simulations, (d) the SAT2 simulation, and (e) the SAT3 simulation. Units are g m^{-2}.

where some of the aerosol gets entrained into the extra-tropical storm track and is efficiently spread throughout the Northern Hemisphere within 21 days. The second is to the Southern Indian Ocean across the ITCZ. Fig. 5.9 shows the global aerosol burden after 21 days for all 5 simulations. In the NOSCAV simulation a broad band of aerosol spreads across the entire Northern Hemisphere extra-tropics. Also a tongue of aerosol laden air crosses the

Table 5.3. Hemispheric-mean aerosol burden after 21-days (mg m^{-2}) excluding Indian Ocean region (20S-20N; 30E-120E).

	Northern Hemisphere	Southern Hemisphere
STD	2.0	0.002
NOSCAV	9.6	1.0
SAT1	1.8	0.004
SAT2	0.8	4.7×10^{-4}
SAT3	0.7	4.5×10^{-4}

ITCZ in the Indian Ocean and eventually enters the Southern Hemisphere storm track to the south of Australia. In the STD simulation, the pathway to the Northern Hemisphere extra-tropics remains important in spite of precipitation scavenging. The pathway across the ITCZ, however is significantly reduced, with the amount of aerosol reaching the Southern Hemisphere reduced by several orders of magnitude compared to the NOSCAV simulation. Table 5.3 shows hemispheric mean aerosol amounts for all simulations, where the Indian Ocean region has been excluded to emphasize the amount transported beyond the region. Southern Hemisphere values are small in all but the NOSCAV simulation. The SAT simulations at least a factor of 2 smaller than the STD simulation in the Southern Hemisphere. Most aerosol that is exported out the region remains in the Northern Hemisphere. Total aerosol in the Northern Hemisphere is 10% smaller in the SAT1 simulation than the STD simulation. Again, with the present scavenging parameterization, there is only weak sensitivity to the distribution of rain rates. The SAT2 and SAT3 simulations have a much more significant effect on total Northern Hemisphere aerosol. Application of satellite observed precipitating fraction reduces Northern Hemisphere aerosol amounts by more than a factor of 2 compared with the STD simulation.

Perhaps the greatest impact on remote aerosol amounts results from the addition of ice phase scavenging. Though the Northern Hemisphere mean values in the Table 5.3 are similar for the SAT2 and SAT3 simulations, these are likely dominated by the values in the

high aerosol tongue extending over China. The stark contrast in Fig. 5.9 between the amount of aerosol in many parts of the Northern Hemisphere in the SAT2 and SAT3 simulations implies that the ability for ice phase precipitation to scavenge aerosol exerts a strong control on the availability of aerosol for transport between continents. In the SAT3 simulation a single tongue of aerosol extends from northern India to the central Pacific Ocean. However, the small amount of aerosol throughout the rest of the Northern Hemisphere suggests that most is removed near the source region prior to reaching the central Pacific Ocean. It should be noted that the significance of low aerosol values, particularly those in the Southern Hemisphere in all of the simulations and the Northern Hemisphere in the SAT3 simulation, cannot be known without additional analysis. For example, in order to assess whether the differences in Southern Hemisphere aerosol amount are significant for radiative forcing, it is necessary to assign radiative properties to the aerosol species, such as scattering and absorption coefficients, which is beyond the scope of this study.

5.6 Summary and conclusion

High resolution, 3-hourly rainfall estimates from multiple satellite platforms has been integrated into the MATCH off-line chemical transport model in order to test the effects of several apparent biases in model simulated precipitation on the concentrations of aerosols in the atmosphere. Errors in the parameterization of tropical deep convection results in a simultaneous over-prediction of total precipitation over the Indian Ocean and a bias toward gently drizzling grid cells at the expense of extreme precipitation events. The effects on aerosol scavenging of biases in simulated rain rates is tested by driving the standard MATCH parameterization of scavenging with grid cell-averaged rain rates from the satellite observations. Simulated scavenging appears to be only weakly effected by changes in the distribution of rain rates. The amount of aerosol scavenged over the Indian Ocean basin is reduced by about 12% when observed rain rates are applied, leading to a slightly higher aerosol burden in the region following a 21 day simulation. This results from a combination

of a 33% lower observed value of 21-day mean rain compared to the MATCH simulation and a substantially fewer number of lightly raining grid cells in the observations. Scavenging at low rain rates dominates the total scavenging and the absence of grid cells with high rain rates in the model does not appear to result in a serious error. When using the MATCH scavenging parameterization, the amount of aerosol removed is much more sensitive to whether or not the model accurately predicts the presence of rain in a grid cell rather than whether the specific rain rate is accurately predicted.

The scavenging parameterization operates by making an estimate of the grid cell fractions containing precipitation. The scavenging rate is directly proportional to the precipitating fraction in the parameterization. Given that there is a rough correlation between surface rain rate and precipitating fraction in the satellite data, the lack of sensitivity to biases in simulated rain rate discussed above suggests that the computation of precipitating fraction is likely flawed. Indeed the parameterized precipitating fraction in the bottom layer of the model is biased toward small precipitating fractions compared to the satellite observations of surface precipitating fraction. The sensitivity of aerosol concentrations to biases in precipitating fraction is tested by replacing the parameterized precipitating fraction with the observed value. Observed precipitation fractions reduce the aerosol amount over the Indian Ocean region by about 24% compared to the STD simulation. Aerosol amounts are less that in the standard model over the entire western portion of the region. The amounts are particularly low in the ITCZ region and south of Indonesia where there is a peak in 21-day mean precipitation and the extreme rain events with high grid cell precipitating fractions occur. Observed precipitation fractions also reduce the vertical extent of the aerosol layer.

Regardless of how aerosol is scavenged, the ITCZ acts as a strong barrier to the transport of aerosol to the Southern Hemisphere. Scavenging based on observed precipitating fraction reduces the total amount of Southern Hemisphere aerosol from 0.002 to 4.7×10^{-4} mg m^{-2} compared to the standard model. Northern Hemisphere aerosol amounts

are reduced by more than a factor to 2 compared to the standard parameterization when observed grid cell precipitating fraction is used in the scavenging. For the remote Northern Hemisphere, aerosol is further reduced with the addition of ice phase scavenging. The aerosol negotiating the pathway to the northeast of the source region toward the Northern Pacific Ocean must reach the upper troposphere in order to accumulate in large amounts over most of the Northern Hemisphere.

References

Ackerman, A. S., O. B. Toon, D. E. Stevens, A. J. Heymsfield, V. Ramanathan, and E. J. Welton, 2000: Reduction of tropical cloudiness by soot. *Science*, **288**, 1042-1047

Andreae, M. O., 1995: Climatic effects of changing atmospheric aerosol levels, in *Future climates of the world: a modeling perspective* (A. Henderson-Sellers, ed.). *World survey of climatology*, **16**, 347-398.

Balkanski, Y. J., D. J. Jacob, G. M. Gardner, W. C. Graustein, and K. K. Turekian, 1993: Transport and residence times of tropospheric aerosols inferred from a global three-dimensional simulation of ^{210}Pb. *J. Geophys. Res.*, **98**, 20,573-20,586.

Clarke, A. D., W. D. Collins, P. J. Rasch, V. N. Kapustin, K. Moore, S. Howell, and H. E. Fuelberg, 2001: Dust and pollution transport on global scales: Aerosol measurements and model predictions. *J. Geophys. Res.*, **106**, 32,555-32,569.

Collins, W. D., P. J. Rasch, B. E. Eaton, B. V. Khattatov, J.-F. Lamarque, and C. S. Zender, 2001: Simulating aerosols using a chemical transport model with assimilation of satellite aerosol retrievals: Methodology for INDOEX. *J. Geophys. Res.*, **106**, 7313-7336.

Crutzen, P. J. and M. G. Lawrence, 2000: The impact of precipitation scavenging on the transport of trace gases: A 3-dimensional model sensitivity study. *J. Atmos. Chem.*, **37**, 81-112.

Giorgi, F. and W. L. Chameides, 1986: Rainout lifetimes of highly soluble aerosols and gases as inferred from simulations with a general circulation model. *J. Geophys. Res.*, **91**, 14 367-14 376.

Houghton, J. T., Y. Ding, D. J. Griggs, M. Noguer, P. J. van der Linden, and D. Xiaosu, Eds., 2001: *Climate Change 2001: The Scientific Basis: Contribution of Working Group 1 to the Third Assessment Report of the Intergovernmental Panel on Climate Change.* Cambridge University Press, 944 pp.

Huffman, G. J., R. F. Adler, D. T. Bolvin, E. J. Nelkin, and E. F. Stocker, 2001: A New Fine-Scale, Quasi-Global Combined Precipitation Estimate Based on TRMM, *Proc. of the 11th Am. Meteoro. Soc. Conf. On Satellite Meteorology and Oceanography,* Madison, Wisconsin.

Huffman, G. J. and D. T. Bolvin, 2002: TRMM real-time multi-satellite data set documentation. Unpublished manuscript avail. from ftp://agnes.gsfc.nasa.gov/pub/huffman/ rt_examples/docs/3B4XRT_doc.

Kalnay, E. and co-authors, 1996: The NCEP/NCAR 40-year reanalysis project. *Bull. Am. Meteorol. Soc.*, **77**, 437-471.

Kiehl, J. T. and B. P. Briegleb, 1993: The relative roles of sulfate aerosols and greenhouse gases in climate forcing. *Science*, **260**, 311-314.

Kummerow, C., Y. Hong, W. S. Olson, S. Yang, R. F. Adler, J. McCullum, R. Ferraro, G. Petty, D. -B. Shin and T. T. Wilheit, 2001: The evolution of the Goddard Profiling Algorithm (GPROF) for rainfall estimation from passive microwave sensors. *J. Appl. Meteor.*, **40**, 1801-1820.

Lawrence, M. G., P. J. Crutzen, P. J. Rasch, B. E. Eaton and N. M. Mahowald: A model for studies of tropospheric photochemistry: Description, global distributions, and evaluation. *J. Geophys. Res.*, **104**, 26 245-26 277.

Mahowald, N. M., R. G. Prinn and P. J. Rasch, 1997a: Deducing CCl_3F emissions using an inverse method and chemical transport models with assimilated winds. *J. Geophys. Res.*, **102**, 28 153-28 168.

Mahowald, N. M., P. J. Rasch, B. E. Eaton, S. Whittlestone and R. G. Prinn, 1997b: Transport of [222]Radon to the remote troposphere using MATCH and assimilated winds from ECMWF and NCEP/NCAR. *J. Geophys. Res.*, **102**, 28 139-28 151.

Posfai, M., J. R. Anderson, P. R. Buseck, and H. Sievering, 1999: Soot and sulfate aerosol particles in the remote marine troposphere. *J. Geophys. Res.*, **104**, 21,685-21,693.

Ramanathan, V. and co-authors, 2001a: Indian Ocean Experiment: An integrated analysis of the climate forcing and effects of the great Indo-Asian haze. *J. Geophys. Res.*, **106**, 28,371-28-398.

Ramanthan, V., P. J. Crutzen, J. T. Kiehl, and D. Rosenfeld, 2001b: Aerosols, Climate and the Hydrological Cycle. *Science*, **294**, 2119-2124.

Rasch, P. J., N. M. Mahowald, and B. E. Eaton, 1997: Representations of transport, convection, and the hydrological cycle in chemical transport models: Implications for the modeling of short-lived and soluble species. *J. Geophys. Res.*, **102**, 28 127-28 138.

Rasch, P. J., and J. E. Kristjánsson, 1998: A comparison of the CCM3 model climate using diagnosed and predicted condensate parameterizations. *J. Climate*, **11**, 1587-1614.

Rasch, P. J., W. D. Collins, and B. E. Eaton, 2001: Understanding the Indian Ocean Experiment (INDOEX) aerosol distributions with an aerosol assimilation. *J. Geophys. Res.*, **106**, 7337-7355.

Rosenfeld, D., 2000: Suppression of rain and snow by urban and industrial air pollution. *Science*, **287**, 1793-1796.

Scott, B. C., 1978: Parameterization of sulfate removal by precipitation. *J. Appl. Meteor.*, **17**, 1375-1389.

Slingo, J. M. 1987: The development and verification of a cloud prediction scheme for the ECMWF model. *Quart. J. Roy. Meteor. Soc.,* **113**, 899-927.

Twomey, S., 1977: The influence of pollution on the shortwave albedo of clouds. *J. Atmos. Sci.*, **34**, 1149-1152.

Wilcox, E. M. and V. Ramanathan, 2001: Scale dependence of the thermodynamic forcing of tropical monsoon clouds: Results from TRMM observations. *J. Climate*, **14**, 1511-1524..

Wilcox, E. M., 2002: Spatial and temporal scales of precipitating tropical cloud systems in satellite imagery and the NCAR CCM3. *J. Climate*, accepted pending revision.

Zhang, G. J. and N. A. McFarlane, 1995: Sensitivity of climate simulations to the parameterization of cumulus convection in the Canadian Climate Centre General Circulation Model. *Atmos.-Ocean*, **33**, 407-446.

Chapter 6

Conclusion

6.1 Summary

This dissertation has presented a quantitative analysis of the impact of tropical cloud systems on latent heating of the atmosphere, radiative forcing of the surface and atmosphere, and the removal of aerosol particles from the atmosphere. These three processes each impact the thermodynamic structure of the atmosphere and the fundamental energy balance of Earth. Because of the important role of clouds and aerosols in the climate system, their successful simulation in climate models is necessary for accurate predictions of climate changes resulting from increasing greenhouse gas and aerosol loading. The dissertation has relied upon observations of cloud cover, precipitation and cloud radiative forcing (CRF) from the Tropical Rainfall Measuring Mission (TRMM) satellite and the METEOSAT-5 geosynchronous satellite. Chapters 3 and 4 have pursued a Lagrangian approach to satellite-based cloud analysis that identifies the boundaries of clouds, tracks them through time, and measures their precipitation and radiative forcing as a function of size and lifetime. The results have revealed the spatial scales at which latent heating and cloud radiative interactions force the climate system. Furthermore, the analysis has demonstrated a strong increase in thermodynamic forcing as the spatial scales of cloud systems increase, illustrated the persistence of giant cloud decks, and quantified systematic biases in the distributions of monsoonal cloud and precipitation in the NCAR CCM3 global model. Chapter 5 uses the knowledge gained about the large mesoscale precipitating structures, and their related biases in model simulations, to refine the role of precipitation in

the removal and long-range transport of aerosols.

This chapter provides a brief summary of the results of this dissertation research. The summary is followed by a discussion of potential responses of Earth's hydrological cycle to increases in greenhouse gas and aerosol loading of the atmosphere and the role of model representations of cloud, precipitation and aerosol processes in climate predictions.

Chapter 3 demonstrates that the impact of Indian Ocean monsoonal cloud systems upon the thermodynamic structure of the ocean-atmosphere column increases with the horizontal scale of the system. This occurs, in part, because a larger system impacts a larger volume of air. But more importantly, because the structural properties of larger cloud systems (*e.g.*, cloud liquid water content, cloud thickness and mesoscale precipitation features) are more effective at reflecting solar energy, reducing longwave emission to space and producing precipitation. As a result, it only takes about 20 mesoscale precipitating features (at about 2×10^5 km^2) at a time over the tropical Indian Ocean to provide the observed latent heating driving the winter monsoon circulation. Within the precipitating portions of cloud systems, the magnitude of latent heating exceeds that of shortwave and longwave cloud radiative forcing (CRF) by one order of magnitude. The spatial scales of CRF, however, are much larger, because 75% of the area covered by cloud is not precipitating. Virtually all cloud thermodynamic forcing occurs in overcast decks of cloud spanning more than one model grid cell, even in coarse resolution models, indicating that such structures should be detected in model output. The situation for precipitation, however, is more complicated as the range of typical model grid cells spans the spectrum of rain cell scales. A few grid cells should be completely filled with precipitation; most should not.

Chapter 4 exploits the large spatial scales of monsoonal cloud systems to perform a direct comparison between satellite observed cloud systems and those simulated by a climate model. Large cloud decks spanning numerous model grid cells do occur in the NCAR CCM3 atmospheric model. In fact, the distribution of cloud scales is biased too

heavily toward the largest scales, resulting in an overall over-prediction of monsoonal cloud cover. The temporal scales of cloud system processes are revealed in the high-frequency METEOSAT-5 imagery. The area covered by cloud associated with active deep convection within a system peaks up to 15 hours before the total area covered by the cloud system peaks. As cloud material spreads from the convective region, it remains suspended long enough for the overcast cloud deck to maintain its integrity through to the following day, when the diurnal cycling of convection builds back up to supply additional moisture to the middle and upper-level portions of the cloud.

Both chapters 4 and 5 perform comparisons of monsoonal precipitation in satellite observations and atmospheric simulations. Because all but the very largest rain cells are too small to fill a model grid cell it is not possible to directly compare the scales of simulated and observed rain cells. However, there is sufficient information to deduce systematic biases in the simulated precipitation that are related to the scales of precipitating structures. Though the models evaluated in chapters 4 and 5 have different names, the deep convection that produces most of the tropical rain is computed using the same parameterization. The model produces about 60% more monsoonal precipitation than is observed by satellite. However, this rain falls predominantly as light rain. Grid cell averaged rates in the simulations are almost always less than 1 mm hr^{-1}, while as much as 60% of observed rain occurs at higher rain rates. In order to produce more overall rain at lower rain rates, precipitation must occur over a larger area and more frequently in the simulation. The simulated Inter-tropical Convergence Zone (ITCZ) south of the equator in the Indian Ocean consists of a much broader region of moderate precipitation than is observed. As many as 50% more grid cells contain precipitation in the simulations. Meanwhile the regions of greatest rainfall accumulate substantially more rain in the observations than in the model. From chapter 3, it is apparent that the most extreme precipitation occurs in the largest rain cells, which develop substantial mesoscale anvil structures in order to cover areas as large as 10^6 km^2. The

organization of precipitation into such structures is largely absent in the model. A modifica-
tion to the model is tested in chapter 4 that accounts for the evaporation of precipitation
below the anvil cloud base as has been observed in mesoscale convective systems (Gamache
and Houze 1983). The modification results in a shift in the distribution of precipitation
toward the observed distribution, with more extreme rain rates. While the modification is
not a complete parameterization of mesoscale convective structures, the result is consistent
with the notion that missing mesoscale processes may be a cause of the model bias toward
light rain.

Chapter 5 tests a hypothesis that a bias in rain rates, such as that found for
monsoonal rain rates in the NCAR CCM3 model, may impact simulated distributions of
aerosols. This is tested by combining the MATCH chemical transport model with high-
resolution satellite precipitation measurements in simulations of winter monsoon transport
of aerosols emitted from the Indian subcontinent. When simulated rain rates are replaced
with observed rain rates in the standard model parameterization of precipitation scavenging,
only moderate differences are found for aerosol concentrations over the Indian Ocean. A
more substantial impact on the aerosol amount is found when the aerosol scavenging is made
proportional to the observed grid cell fraction containing precipitation. Under the standard
model parameterization, the inclusion of extreme precipitation events does not increase
scavenging because of the standard precipitation underestimates the grid cell precipitating
fraction for these events. Scavenging according to observed grid cell precipitating fraction
substantially reduces aerosol amounts in the Indian Ocean ITCZ region. It also substantially
reduces the transport of aerosol beyond the Indian Ocean region. Transport of aerosol
to the Southern Hemisphere is substantially impeded by precipitation along the ITCZ in all
simulations. In the Northern Hemisphere, away from the source region, aerosol amounts
are more than a factor of 2 smaller, compared to the standard model, when the grid cell
precipitating fraction observed by satellite is used in the scavenging computation. This

effect is most dramatic when scavenging by ice phase precipitation is included, suggesting that long range transport of aerosols is linked to the ability of aerosols to reach the upper-troposphere.

The results of this dissertation have emphasized the importance of large cloud systems embedded with highly energetic precipitation structures. While such systems clearly dominate small and moderate sized systems in contributing to winter monsoon cloud cover, latent heating, radiative forcing, and aerosol removal, note that moderate and small convective clouds are present in much greater numbers. They play a role in important cloud processes such as vertical transport of mass and momentum. During the Indian Ocean Experiment, an elevated aerosol layer was periodically observed at 3 km, and sometimes above the tops of the smaller clouds (Ramanathan et al 2001a). A substantial amount of mass, including haze, is transported vertically in small and moderate clouds over the Indian Ocean.

6.2 Implications for climate and climate change

The emphasis in much of the dissertation work has been on processes occurring within precipitating cloud systems. Such systems, however, do not behave entirely independently. The global surface and atmospheric energy budgets ultimately control the total amount of precipitation, the availability of moisture to condense as cloud, and the frequency and spatial distribution of cloud systems. As the activities of humans have an increasing impact on these budgets through greenhouse gas and aerosol loading of the atmosphere, there is the potential for significant change to the hydrological cycling of the climate system which must be reflected in the structure and thermodynamic forcing of the precipitating cloud systems.

Climate change resulting from the increase in greenhouse gas loading is generally expected to be accompanied by an increase in evaporation and precipitation, a so-called spin-up of the hydrological cycle. Related to the hydrological spin-up is an expected

increase in extreme precipitation events, particularly an increase in precipitation associated with individual storms. As surface temperature increases, the saturation vapor pressure in the surface boundary layer of the atmosphere increases and surface evaporation is enhanced (Manabe and Wetherald 1975). This must be balanced by an increase in precipitation if moisture is not to build up rapidly in the atmosphere. This enhanced hydrological cycle is a common response among GCMs in increased greenhouse gas simulations (Houghton et al. 2001). Enhanced precipitation could result from increases in the frequency of rain events, or a shift in the intensity of rain events, or both (Karl and Knight 1998). An analysis of daily accumulations of rain at meteorological stations in the U.S. has documented an increase in both temperature and precipitation, with a large increase in the portion of the precipitation resulting from extreme precipitation events (defined as >50.8 mm hr^{-1}; Karl et al. 1995). As discussed above, TRMM data from the winter monsoon indicate that biases in the CCM3 model are present in both the mean rain rate and the distribution of rain rates. The simulated hydrological cycle is faster (at least in the Indian Ocean region) than observed, resulting in a higher amount of total precipitation. Conversely, extreme precipitation events are less frequent. In order for the model to provide quantitative predictions of changes in hydrological cycling and high-frequency precipitation variability, the sources of such biases must be determined. Enhancing local evaporation of falling precipitation within simulated clouds was shown in chapter 4 to improve the representation of the rain rate distribution, though it had little impact on the total amount of precipitation in the region. The distribution and rate of convergence of low-level water vapor is perhaps a bigger influence than local cloud physics on the overall rate of hydrological cycling in the region. Inter-comparisons, such as presented here of instantaneous or hourly rain rates between models and observations must be extended to more regions and time periods. Though this study has focused on a region of predominantly ocean, it is land areas and the societies and ecosystems they support that are of principal interest in studies of precipitation variability.

Aerosols introduce additional perturbations to the hydrological cycle. The dominant interaction between rainfall and aerosols is that of precipitation scavenging. Indeed, precipitation scavenging is the principle mechanism for removing aerosols from the atmosphere. Evidence of the efficient removal of aerosols in tropical precipitating cloud systems is offered in chapter 5. Though the presence of extreme precipitation events in the observed rain rate distribution has little effect on the aerosol removal rate under the standard scavenging parameterization, aerosol removal is substantial increased along the Indian Ocean ITCZ when the removal rate is tied directly to the observed spatial coverage of precipitation. This results from the large spatial coverage of the most intense precipitating structures. This scavenging study, however, is just a first step in understanding and simulating the interactions between aerosol and precipitation, as the scavenging parameterizations explored here do not account for many potential microphysical interactions. For example, urban and industrial pollution has been demonstrated to suppress precipitation (Rosenfeld, 2000). Plumes containing small aerosol particles can nucleate droplets that are smaller than $14\mu m$, which do not commonly coalesce into precipitation sized drops. This effect, however, may depend on the details of the aerosol size distribution, as a relatively few large particles, such as sea salt spray, may override precipitation suppression (Rosenfeld et al. 2002). Such microphysical impacts on precipitation have only been verified in case studies.

Finally, aerosols may impact the hydrological cycle through their radiative forcing. The direct effect of bright aerosols, such as sulfates, is a surface cooling of 0.1 - 1 W m^{-2} globally (Houghton 2001), as a portion of the sunlight that would have been absorbed at the surface is reflected back to space. The addition of black carbon in aerosol, however, can lead to significant solar absorption in the aerosol layer, leading to a radiative heating of the atmosphere. Such heating enhances the surface cooling by further reducing the amount of solar radiation available for surface absorption. These radiative forcing effects can be quite significant regionally. The haze layer over the Indian Ocean during winter 1999 was

estimated to cause an average atmospheric warming of $+18$ W m^{-2} and surface cooling of -20 W m^{-2} (Ramanathan et al. 2001a). Such a surface cooling can impact the hydrological cycle by impacting the surface energy budget. The surface is principally cooled by evaporation (Kiehl and Trenberth 1997; see also discussion in chapter 1, section 1.1). A substantial reduction in solar energy at the surface reduces the amount of required evaporation, and leads to a spin down of the hydrological cycle (Ramanathan et al., 2001b). While aerosol radiative cooling has been determined to compensate for a portion of greenhouse gas warming (Kiehl and Briegleb 1993), it remains to be determined if aerosols may compensate globally for changes in the hydrological cycle. Nevertheless, a test of the global response to the wintertime Indian Ocean aerosol forcing in a GCM found a tropics-wide reduction in evaporation, although locally precipitation increased owing to the low-level aerosol heating (Chung et al. 2002).

Placing aerosols on par with greenhouse gases as an agent for global change puts a premium on unraveling the complex interactions between aerosols, cloud droplets and global hydrology. Quantitative global assessments and future predictions of aerosol forcing of climate will require a reasonable representation of precipitation scavenging, which clearly requires a proper simulation of the spatial distribution of precipitation. Potential feedbacks, however, between aerosols and precipitation substantially complicate the problem.

References

Chung, C. E., V. Ramanathan, and J. T. Kiehl, 2002: Effects of the south asian absorbing haze on the northeast monsoon and surface-air heat exchange. *J. Climate*, **15**, 2462-2476.

Gamache, J. F. and R. A. Houze Jr., 1983: Water budget of a mesoscale convective system in the tropics. *J. Atmos. Sci.*, **40**, 1835-1850.

Houghton, J. T., Y. Ding, D. J. Griggs, M. Noguer, P. J. van der Linden, and D. Xiaosu, Eds., 2001: *Climate Change 2001: The Scientific Basis: Contribution of Working Group 1 to the Third Assessment Report of the Intergovernmental Panel on Climate Change.* Cambridge

University Press, 944 pp.

Karl, T. R., R. W. Knight, and N. Plummer, 1995: Trends in high-frequency climate variability in the twentieth century. *Nature*, **377**, 217-220.

Karl, T. R. and R. W. Knight, 1998: Secular trends of precipitation amount, frequency, and intensity in the United States, *Bull. Amer. Meteor. Soc.*, **79**, 231-241.

Kiehl, J. T. and B. P. Briegleb, 1993: The relative roles of sulfate aerosols and greenhouse gases in climate forcing. *Science*, **260**, 311-314.

Kiehl, J. T. and K. E. Trenberth, 1997: Earth's annual global mean energy budget. *Bull. Am. Meteorol. Soc.*, **78**, 197-208.

Manabe, S. and R. T. Wetherald, 1975: The effects of doubling the CO2 concentration on the climate of a general circulation model, *J. Atmos. Sci.*, **32**, 3-15.

Ramanathan, V. and co-authors, 2001a: Indian Ocean Experiment: An integrated analysis of the climate forcing and effects of the great Indo-Asian haze. *J. Geophys. Res.*, **106**, 28,371-28-398.

Ramanthan, V., P. J. Crutzen, J. T. Kiehl, and D. Rosenfeld, 2001b: Aerosols, Climate and the Hydrological Cycle. *Science*, **294**, 2119-2124.

Rosenfeld, D., 2000: Suppression of rain and snow by urban and industrial air pollution. *Science*, **287**, 1793-1796.

Rosenfeld, D., R. Lahav, A. Khain, and M. Pinsky, 2002: The role of sea spray in cleansing air pollution over ocean via cloud processes., *Science*, **297**, 1667-1670.